RCS MEASUREMENT OF POLARIMETRIC ACTIVE RADAR CALIBRATORS

Kamal Sarabandi
Yisok Oh
Radiation Laboratory
Department of Electrical Engineering
and Computer Science
The University of Michigan
Ann Arbor, MI 48109

June 1990

JPL Contract 958744

RCS MEASUREMENT OF POLARIMETRIC ACTIVE RADAR CALIBRATORS

by

Kamal Sarabandi

Yisok Oh

Radiation Laboratory

Department of Electrical Engineering and Computer Science

The University of Michigan

PI: Fawwaz T. Ulaby

JPL Contract 958744

June 19, 1990

Absract

Practical aspects of polarimetric measurement of active radar calibrators (PARC) are discussed in this report. A new polarimetric calibration technique (STCT) is employed for polarimetric radar cross section measurement of L- and C-band PARCs. The amplitude and phase of the scattering matrix elements are given over a wide range of incidence angle for azimuth, elevation, 45°, and 135° planes. Tables for scattering matrix elements and the polarization signatures at boresight are also provided.

Contents

List of Figures

List of Tables

1 Introduction

Airborne and space-borne polarimetric imaging SAR has been shown to be an important remote sensing tool for the acquisition of quantitative information about the earth's environment on a global scale. In order to utilize the quantitative data scientifically, external calibration of the radar system is necessary. The external calibration of radar systems is performed by using a target with a specified radar cross section (RCS) known as a calibration target.

Calibration targets, in general, can be categorized into two major groups: 1) passive calibrators and 2) active calibrators [1]. Although passive calibrators are more stable and reliable than the active ones, they are less desirable because of their large physical dimensions. In recent years, polarimetric active radar calibrators (PARC) have been used extensively and are planned to be employed for external calibration of SAR systems [2] in support of future spaceborne missions.

The success of external calibration relies on the knowledge of the scattering matrix of the calibration target(s). Although it may be possible to estimate the elements of the scattering matrix for a calibration target to a reasonable extent, the manufacturing tolerances always leave a great deal of uncertainty in the estimation. Therefore it is imperative to measure the calibrators against a precise calibration target (such as a metallic sphere) under laboratory condition. This also reveals another drawback for passive calibrators with large physical dimensions, namely that the far-field condition and uniform illumination criteria cannot be met in the laboratory.

Until recently, it has been very difficult to measure the scattering matrices of targets over a wide range of incidence angle and frequency with the desired accuracy. Advances in technology and calibration methods have made it possible to measure the elements of the scattering matrix with an accuracy of 0.5 dB in magnitude and 5° in phase [3].

The purpose of this report is to document measurements of JPL's L- and C-band PARCs using the new calibration technique (STCT) given in Appendix A. The measurements were performed in the UM anechoic chamber using a fully automated polarimetric scatterometer[4].

2 System Configuration and Measurement Setup

The polarimetric measurements of the PARCs were performed by L- and C-band scatterometers. A simplified block diagram of the scatterometer system is shown in Fig. (1). The scatterometer is an HP 8753A-based system with both phase and amplitude measurement capability and 100 dB dynamic range. The ability of the network analyzer to generate the time domain response of the frequency measurement allows us to separate the unwanted short-range signals from the desired target response (known as software gating). The sequence of polarization selection, data collection, and target orientation is performed via an HP 9000 series computer. The relay actuator energizes the frequency and polarization switches. The amplifier and pulsing network eliminates the short-range returns from the antenna and circulators to increase the dynamic range for RCS measurements [5].

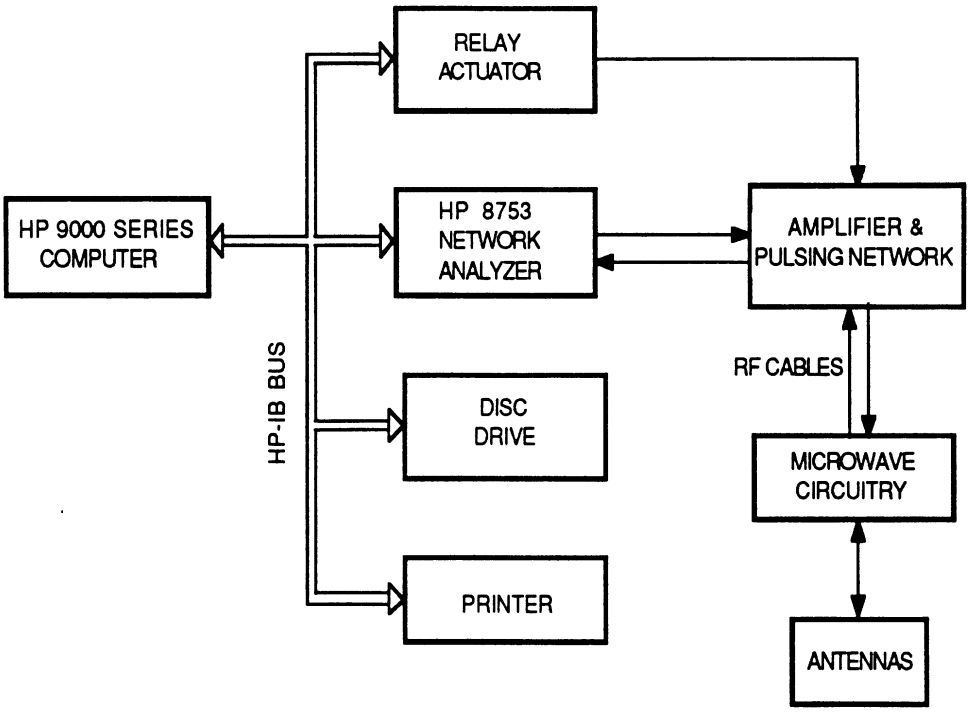

Figure 1: Block diagram of the scatterometer system.

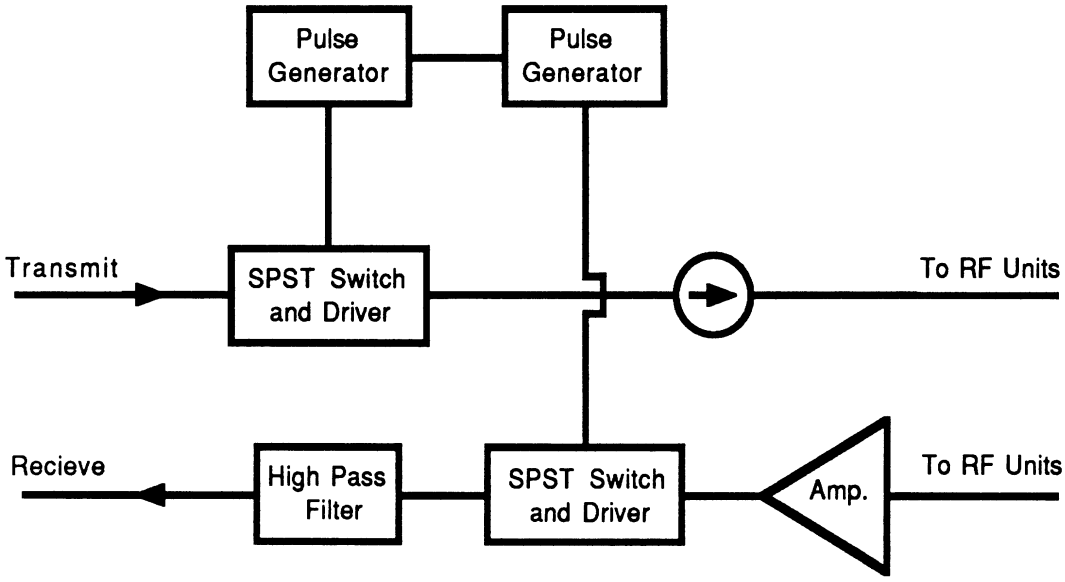

Figure 2: Block diagram of the pulsing network.

In this scheme, the receiver is switched off during transmission and then reconnected when the target return is expected to arrive at the receiver. Since the switching is done at a much higher rate than the receiver's bandwidth the network analyzer does not sense that the incoming signal is pulsed and it is measured as if it were a CW signal. The block diagram of the amplifier and pulsing network is shown in Fig. (2).

The synthesized source of the network analyzer spans the frequency range 300 KHz to 3 GHz and therefore for C-band up- and down-convertors are used. The block diagrams of the L- and C-band microwave circuitry are given in Figs. (3) and (4), respectively. The up-convertor of the C-band unit is a very stable microwave source operating at 6.5 GHz. The frequency range of the network analyzer for C-band measurement must be set to 1-1.5 GHz in order to operate the C-band scatterometer at 5-5.5 GHz. The operating frequency of the L-band system is 1.1-1.4 GHz. A new orthomode transducer (OMT) and dual-polarized antenna were designed for this project at L-band. The overall cross-polarization isolation of the new OMT and antenna is better than 35 dB.

Because PARC has a high gain amplifier, reflection from nearby objects might increase the feedback which would cause oscillation. To avoid this problem and also to have a very good signal to background ratio, the PARCs were mounted on a styrofoam pedestal in an anechoic chamber. The correct position of the PARCs with respect to the antenna coordinate system was accomplished by an azimuth-over-elevation positioner as depicted in Fig. (5). The azimuth turntable

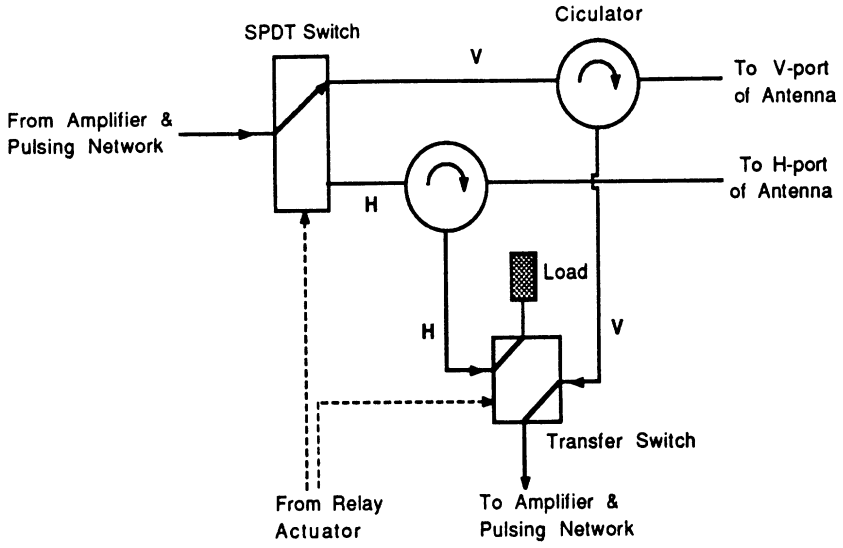

Figure 3: Block diagram of the L-band microwave circuitry.

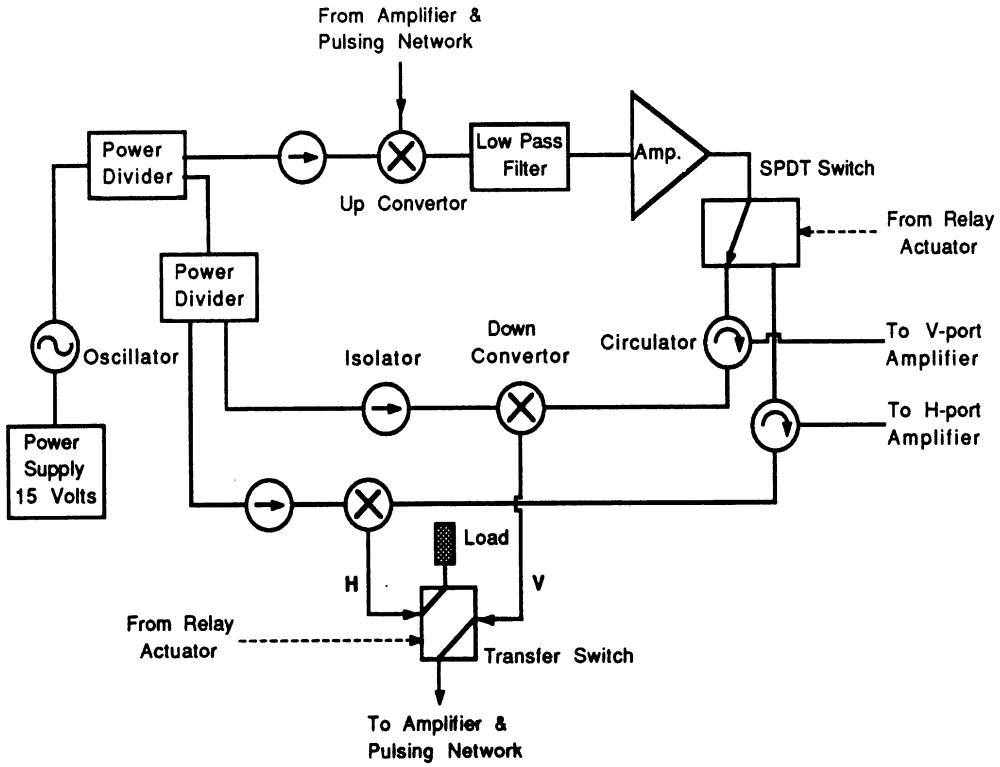

Figure 4: Block diagram of the C-band microwave circuitry.

is a computer controlled stepper motor with an accuracy of a fraction of a tenth of a degree and the elevation controller is a precise analog positioner.

3 Calibration Procedure

To calibrate the PARCs, we used the single-target calibration technique (STCT) described in Appendix A. The error in measurement of scattering matrix using this technique is less than 0.5 dB in amplitude and 5° in phase. With the STCT the antenna cross-talk contamination and channel imbalances are obtained by measuring only a single calibration target, namely a metallic sphere. This technique is immune to errors caused by target alignment with respect to the antenna coordinate system.

Using a four-port network approach it is shown that the measured scattering matrix of a target with scattering matrix **s** is given by

$$\mathbf{M} = \begin{bmatrix} R_1 & 0 \\ 0 & R_2 \end{bmatrix} \begin{bmatrix} 1 & C \\ C & 1 \end{bmatrix} \mathbf{s} \begin{bmatrix} 1 & C \\ C & 1 \end{bmatrix} \begin{bmatrix} T_1 & 0 \\ 0 & T_2 \end{bmatrix} + \mathbf{N}$$

where the **R** and **T** matrices are the receive and transmit channel imbalances, C is the antenna cross-talk contamination factor, and **N** is a matrix representing thermal noise and background reflections. The background contribution can be obtained by measuring the empty chamber and the effect of the thermal noise can be minimized by an integration process.

By denoting the measured scattering matrix elements of the sphere and the PARC, respectively, by m_{ij}^{o} and m_{ij}^{u}, the unknown scattering matrix elements of

the PARC can be obtained from

$$
\begin{aligned}
s_{vv} &= \frac{1}{(1-C^2)^2}\left[-2C^2\left(\frac{m_{12}^u}{m_{12}^o}+\frac{m_{21}^u}{m_{21}^o}\right)+(1+C^2)\left(\frac{m_{11}^u}{m_{11}^o}+C^2\frac{m_{22}^u}{m_{22}^o}\right)\right]s^o \\
s_{hh} &= \frac{1}{(1-C^2)^2}\left[-2C^2\left(\frac{m_{12}^u}{m_{12}^o}+\frac{m_{21}^u}{m_{21}^o}\right)+(1+C^2)\left(\frac{m_{22}^u}{m_{22}^o}+C^2\frac{m_{11}^u}{m_{11}^o}\right)\right]s^o \\
s_{vh} &= \frac{C}{(1-C^2)^2}\left[2\frac{m_{12}^u}{m_{12}^o}+2C^2\frac{m_{21}^u}{m_{21}^o}-(1+C^2)\left(\frac{m_{11}^u}{m_{11}^o}+\frac{m_{22}^u}{m_{22}^o}\right)\right]s^o \\
s_{hv} &= \frac{C}{(1-C^2)^2}\left[2\frac{m_{21}^u}{m_{21}^o}+2C^2\frac{m_{12}^u}{m_{12}^o}-(1+C^2)\left(\frac{m_{11}^u}{m_{11}^o}+\frac{m_{22}^u}{m_{22}^o}\right)\right]s^o
\end{aligned}
$$

where s^o is the theoretical value for the diagonal elements of the sphere's scattering matrix. The cross-talk contamination factor is given by

$$C = \pm\frac{1}{\sqrt{a}}\left(1-\sqrt{1-a}\right)$$

where $a \triangleq \frac{m_{12}^o m_{21}^o}{m_{11}^o m_{22}^o}$ and the branch of the square root is chosen such that $\mathrm{Re}\left[\sqrt{1-a}\right] > 0$. The uncertainty on the sign of C can be removed when measuring PARCs because the general trend of phase behavior is known.

4 Experimental Results

The measurements were performed in a 14-meter long anechoic chamber. The PARC under test was mounted on a styrofoam pedestal on an azimuth-over-elevation positioner. To assure that the PARC is not oscillating in the chamber, the energy flow between the receive and transmit antenna was monitored by inserting a 20 dB directional coupler between the amplifier and the transmit antenna. Also to avoid saturating the PARC's amplifier and scatterometer's receiver, the scatterometer transmit power was adjusted such that the PARC output power was around 5 dBm. For the actual RCS measurements the directional coupler was removed.

A 12-inch metallic sphere was used as the calibration target, and the signal to noise ratio was better than 30 dB in all cases. The L- and C-band measurements were performed over the frequency range 1.1-1.4 GHz and 5-5.5 GHz, respectively. All the data presented in this report are measurements at the center frequencies, namely 1.25 GHz for L-band and 5.3 GHz for the C-band. The backscattered radar cross section patterns were measured over the range of incidence angle from -40 to +40 degrees relative to the boresight direction in the azimuth, elevation, 45°, and 135° planes.

The radar cross section of a PARC can be decomposed into two components. The first component is the contribution of the front panel and the antennas and the second component is the contribution of the delay line and amplifier. Using the range-gating capability of the scatterometers, the two responses can be separated. Figs. (6) and (7) represent the time-domain responses of an L-band and a C-band PARC, respectively, where the relative amplitudes of the two components can be compared. In all of the results shown in this report, the contribution of the front panel and the antennas has been gated out.

In this study three L-band and three C-band PARCs were measured. The L-band PARCs are designated according to their serial number and the C-band PARCs designations are according to Fig. (8). In order to measure the RCS patterns in the desired planes, the PARCs were oriented as shown in Fig. (9). Tables 1 and 2 give the measured elements of the scattering matrices for L- and C-band at boresight for quick reference.

The polarization signature of PARCs L1 and C1 are plotted in Figs. (10) - (13). It is shown that co-polarized signatures for the case where the antennas are oriented 45° with respect to vertical direction (45° and 135° for L-band and azimuth and elevation for C-band) are slightly different from the theoretical response due to small errors in the phase measurement. However, for the case where the antennas are parallel and perpendicular to the vertical direction (azimuth and elevation for L-band and 45° and 135° for C-band) the errors in phase measurement do not affect the polarization signatures.

In Figs. (14) - (49) the measured RCS patterns of L- and C-band PARCs are shown. The C-band patterns seem reasonable but the L-band patterns are not quite symmetric, the maximum RCS appears at about 10° from boresight, and the measured phases are very much different from the expected values. These problems are due to the fact that the transmit and receive antennas are very close to each other (touching). The antennas are in the near field of each other and therefore the amplitude and phase patterns are different from the patterns of isolated antennas.

5 Conclusions

The radar cross section patterns of three L-band and three C-band PARCs were measured polarimetrically. The measurements were performed in an anechoic chamber and accurate orientation of the PARCs was achieved by a very precise azimuth-over-elevation positioner.

The measurements show that the RCS is not very sensitive to changes in the

azimuth and elevation angles, but it is very sensitive to the rotation angle about the boresight direction. It is found that when the PARCs transmit and receive antennas are parallel and perpendicular to the vertical direction, small errors in the orientation angles or errors in phase measurement have a minor effect on calibration accuracy. It is also found that the close proximity of the L-band antennas has caused significant problems for the patterns and considerable errors in the scattering matrix elements. We recommend that the antennas be separated by at least one wavelength.

References

[1] Brunfeldt, D.R., and F.T. Ulaby, " Active calibrators for radar calibration ", *IEEE Trans. Geosci. Remote Sensing*, vol 22, no 2, 1984.

[2] Freeman, A., Y. Shen, and C.L. Werner, " Polarimetric SAR calibration experiment using active radar calibrators", *IEEE Trans. Geosci. Remote Sensing*, vol. 28, no. 2, 1990.

[3] Sarabandi, K., and F.T. Ulaby, " A convenient technique for polarimetric calibration of radar systems", *IEEE Trans. Geosci. Remote Sensing*, submitted for publication.

[4] Tassoudji, M.A., K. Sarabandi, and F.T. Ulaby, "Design consideration and implementation of the LCX polarimetric scatterometer (POLARSCAT)", *Radiation Laboratory Report No. 022486-T-2*, The University of Michigan, June 1989.

[5] Liepa, V.V., K. Sarabandi, and M.A. Tassoudji, " A pulsed network analyzer based scatterometer", *Proc. of IEEE Geosci. Remote Sens. Symp.*, Vancouver, July 1989.

		vv	vh	hv	hh
L_1	Az	1.9∠0.0	-31.1∠91.3	36.72∠121.4	1.4∠-120.0
	El	-6.1∠0.0	35.0∠14.2	-53.2∠-27.6	-2.5∠-84.6
	45^o	31.2∠0.0	30.6∠-13.4	30.6∠197.0	29.9∠184.5
	135^o	31.3∠0.0	30.9∠177.8	30.9∠19.4	30.8∠185.2
L_2	Az	-3.4∠0.0	-24.6∠-9.1	35.8∠153.0	-3.3∠-34.5
	El	-3.0∠0.0	36.4∠184.9	-47.6∠-81.2	-2.7∠20.0
	45^o	29.9∠0.0	29.5∠9.0	29.5∠175.7	29.2∠184.9
	135^o	30.8∠0.0	30.6∠187.8	30.6∠-6.5	30.2∠182.4
L_3	Az	-2.7∠0.0	-57.6∠-74.1	36.6∠173.4	-2.6∠186.6
	El	-17.4∠0.0	38.8∠-56.6	-44.2∠202.4	-1.7∠101.9
	45^o	32.2∠0.0	31.6∠8.0	31.8∠179.1	31.9∠182.7
	135^o	32.6∠0.0	32.2∠186.7	32.2∠0.3	32.3∠183.3

Table 1: Elements of scattering matrix for L-band PARCs. The entries are in the form $A_{ij}\angle\phi_{ij}$, where A_{ij} is the RCS σ_{ij} in dBsm ($\sigma_{ij} = 4\pi|s_{ij}|^2$) and ϕ_{ij} is the phase of s_{ij} in degrees.

		vv	vh	hv	hh
C_1	Az	27.2∠0.0	27.1∠187.2	27.1∠-1.7	27.1∠185.5
	El	27.2∠0.0	27.1∠-3.1	27.0∠183.7	26.8∠180.8
	45°	-1.9∠0.0	-24.2∠119.0	32.8∠-59.0	-7.1 ∠182.2
	135°	-1.2∠0.0	33.0∠-52.3	-46.0∠122.9	-3.1∠-163.6
C_2	Az	26.7∠0.0	26.7∠-2.7	26.7∠181.6	26.6∠179.3
	El	26.6∠0.0	26.7∠180.1	26.7∠-0.2	26.8∠180.3
	45°	-19.6∠0.0	32.5∠-148.8	-46.6∠52.2	-10.9 ∠145.8
	135°	-40.2∠0.0	-55.2∠6.3	32.4 ∠-55.7	-15.6∠186.5
C_3	Az	26.5∠0.0	26.4∠1.0	26.4∠178.6	26.2∠179.6
	El	26.3∠0.0	26.1∠180.0	26.1∠-1.3	25.9∠178.9
	45°	-5.2∠0.0	32.3∠145.3	-51.0∠-18.6	-8.3∠179.3
	135°	-8.5∠0.0	-44.3∠-141.4	31.5∠46.8	-3.8∠184.4

Table 2: Elements of scattering matrix for L-band PARCs. The entries are in the form $A_{ij}\angle\phi_{ij}$, where A_{ij} is the RCS σ_{ij} in dBsm ($\sigma_{ij} = 4\pi|s_{ij}|^2$) and ϕ_{ij} is the phase of s_{ij} in degrees.

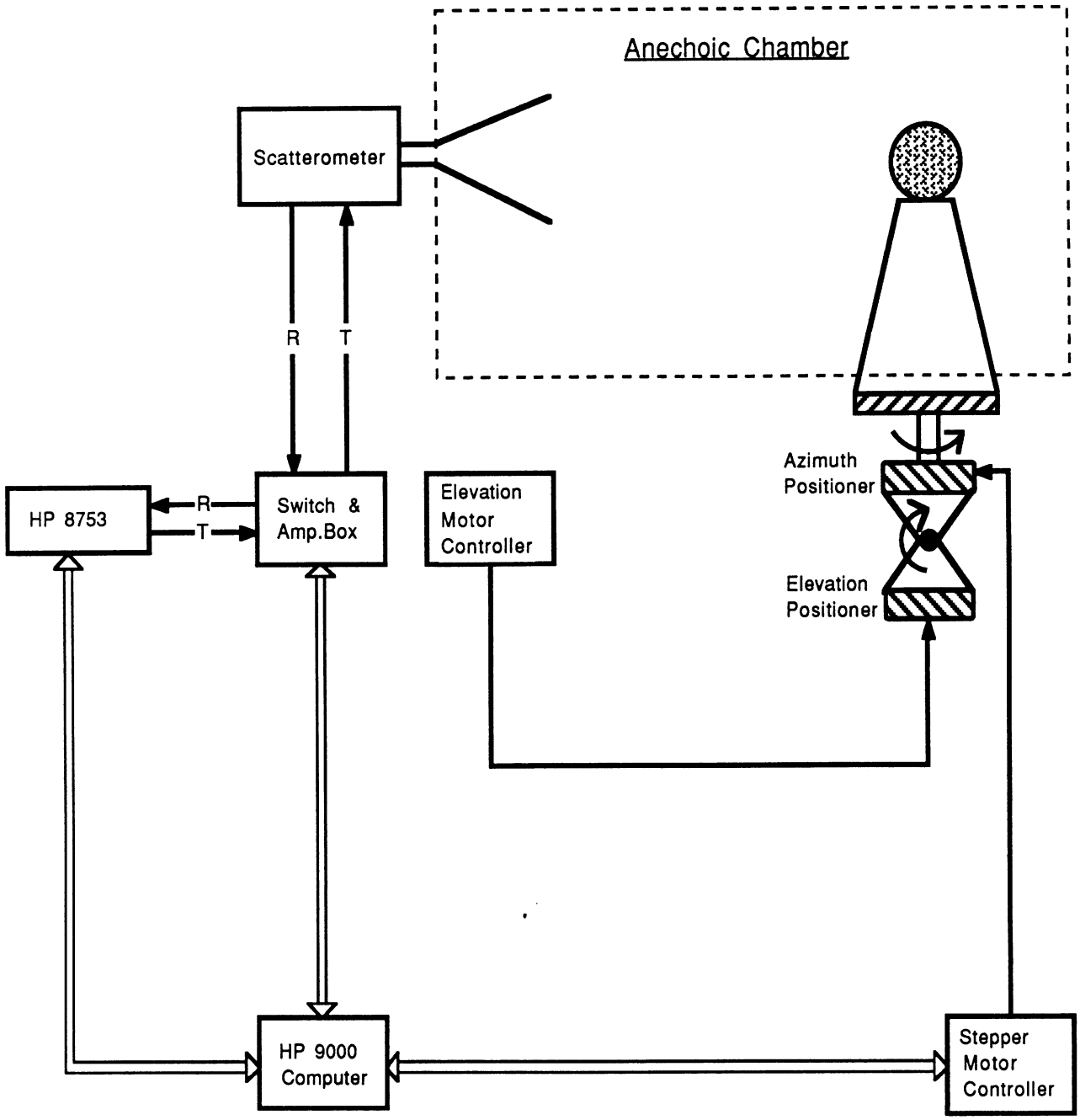

Figure 5: Automatic radar cross section measurement setup.

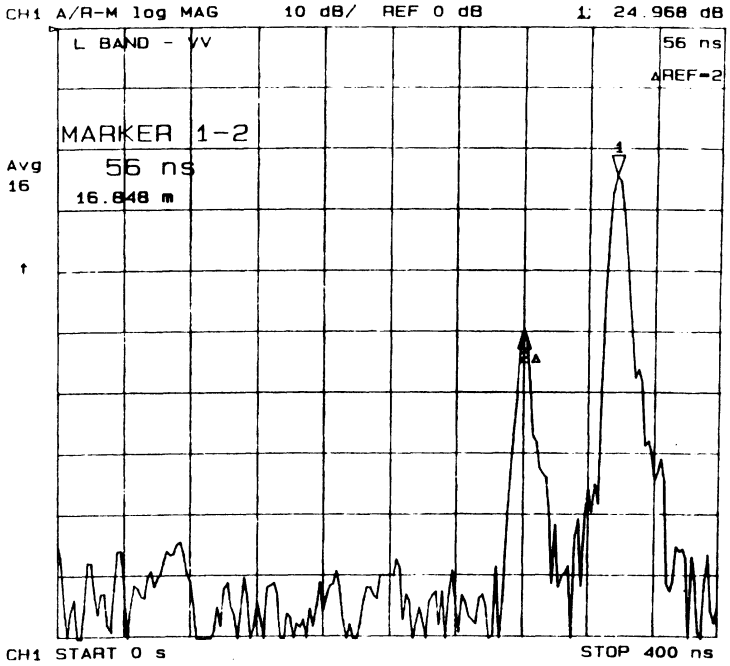

Figure 6: Time domain response of an L-band PARC.

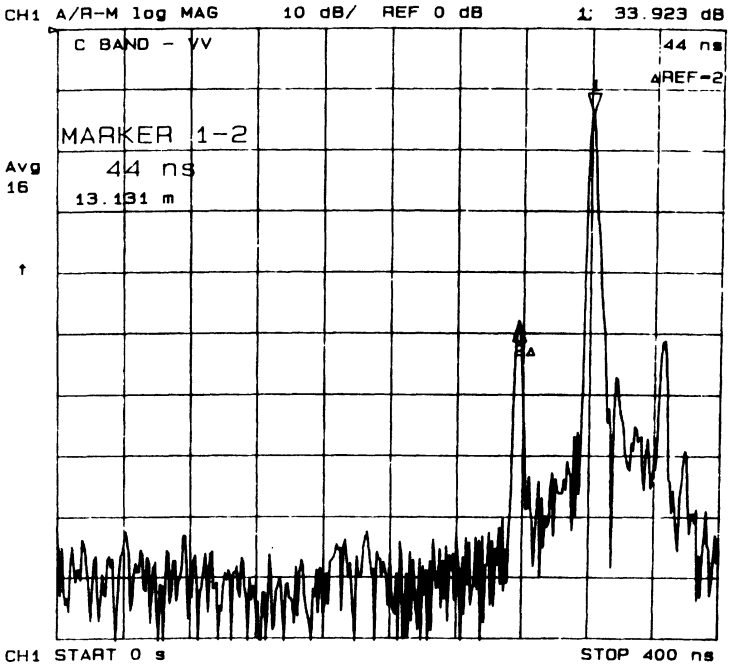

Figure 7: Time domain response of a C-band PARC.

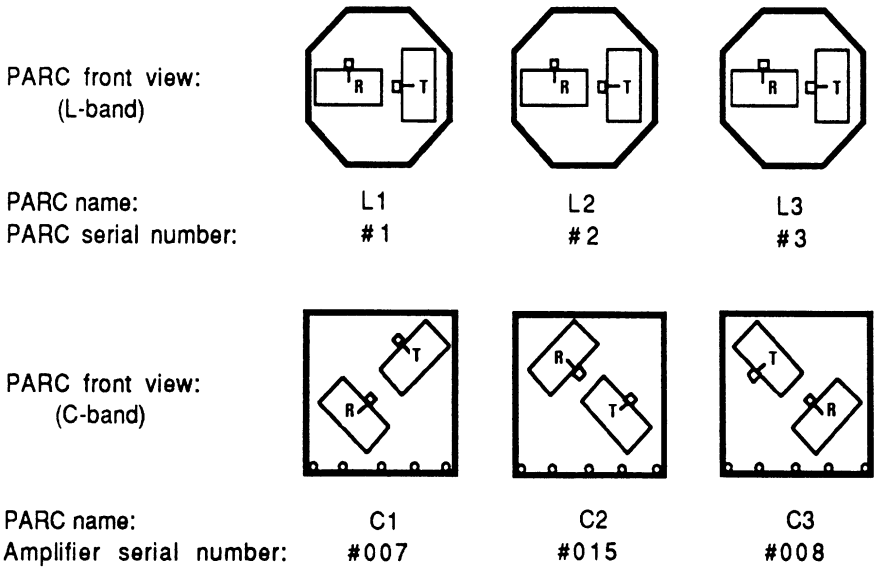

Figure 8: The front panel of L- and C-band PARC's as seen by a radar.

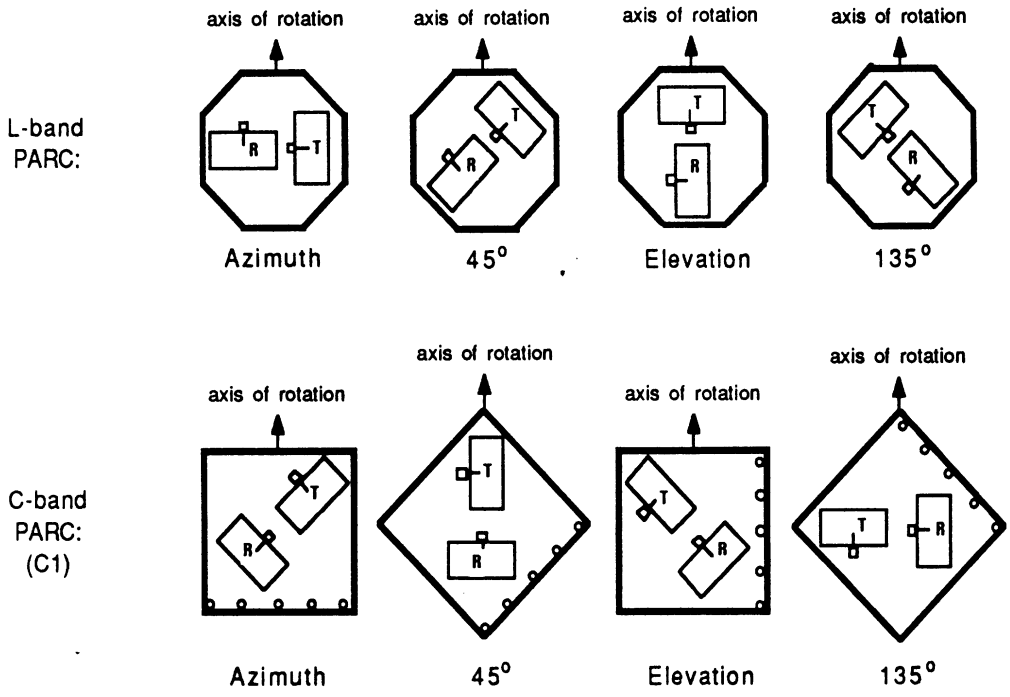

Figure 9: The orientation of L- and C-band PARC's for pattern measurement.

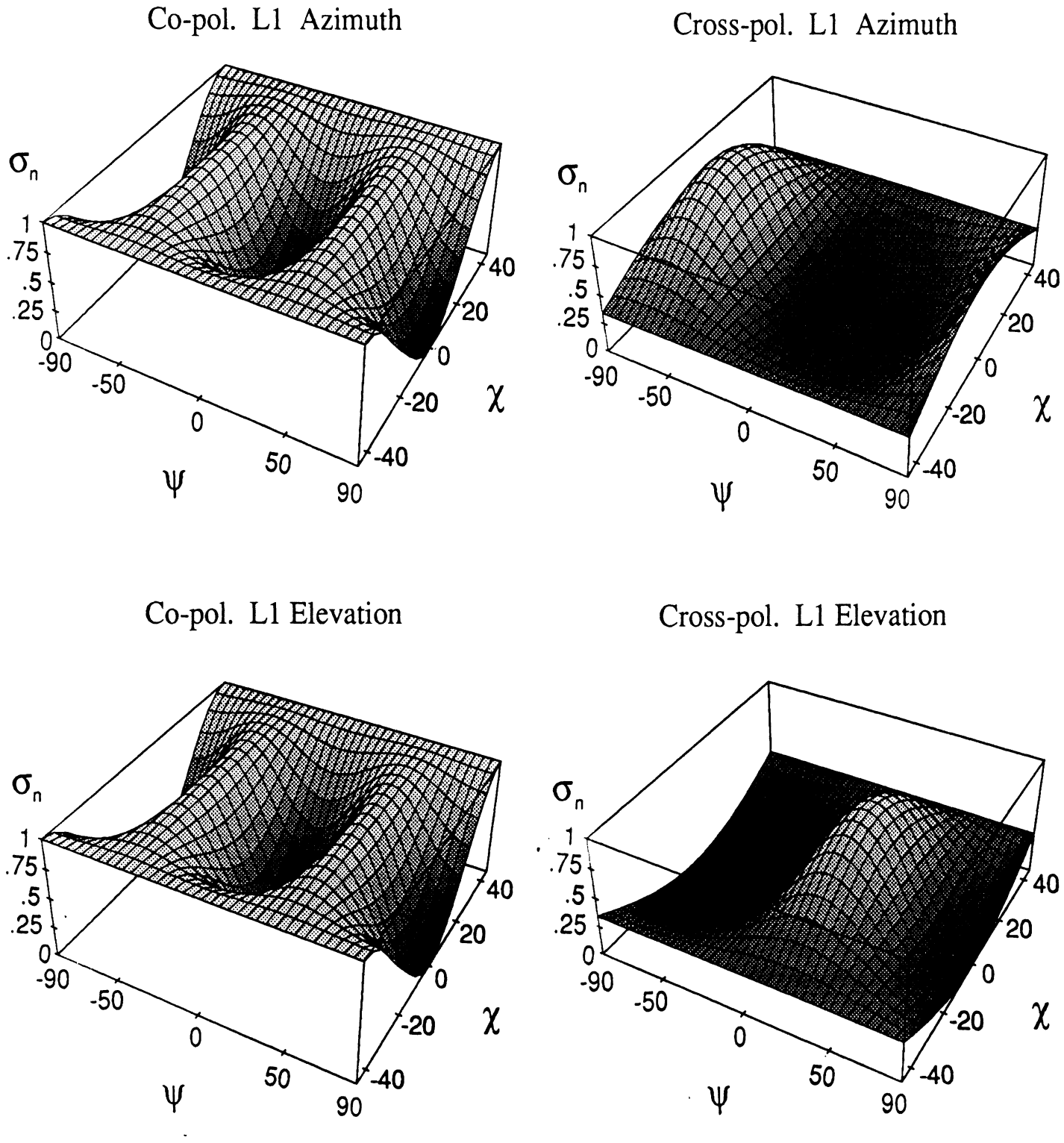

Figure 10: The azimuth and elevation polarization signature for L1 PARC.

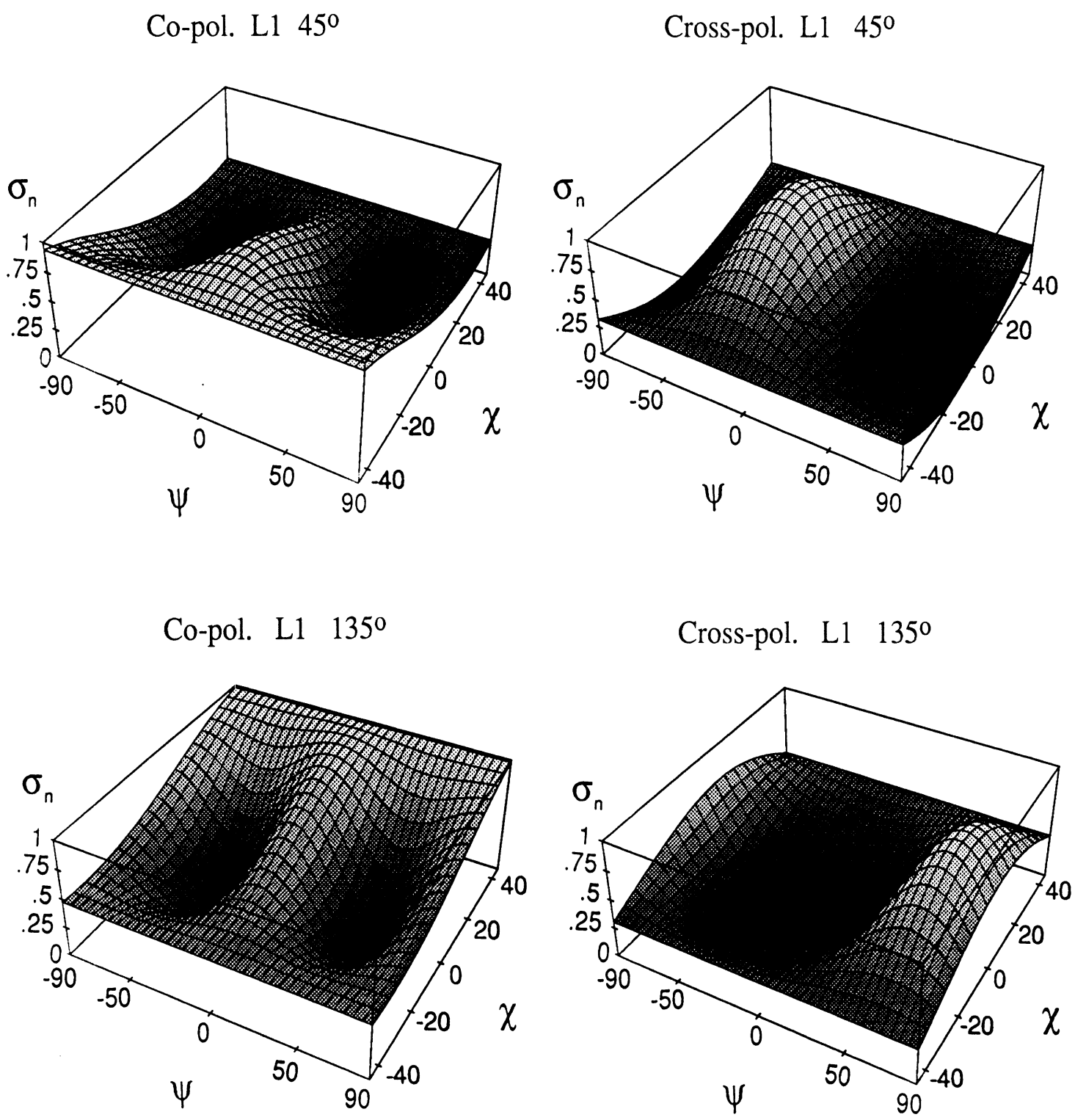

Figure 11: The 45° and 135° polarization signature for L1 PARC.

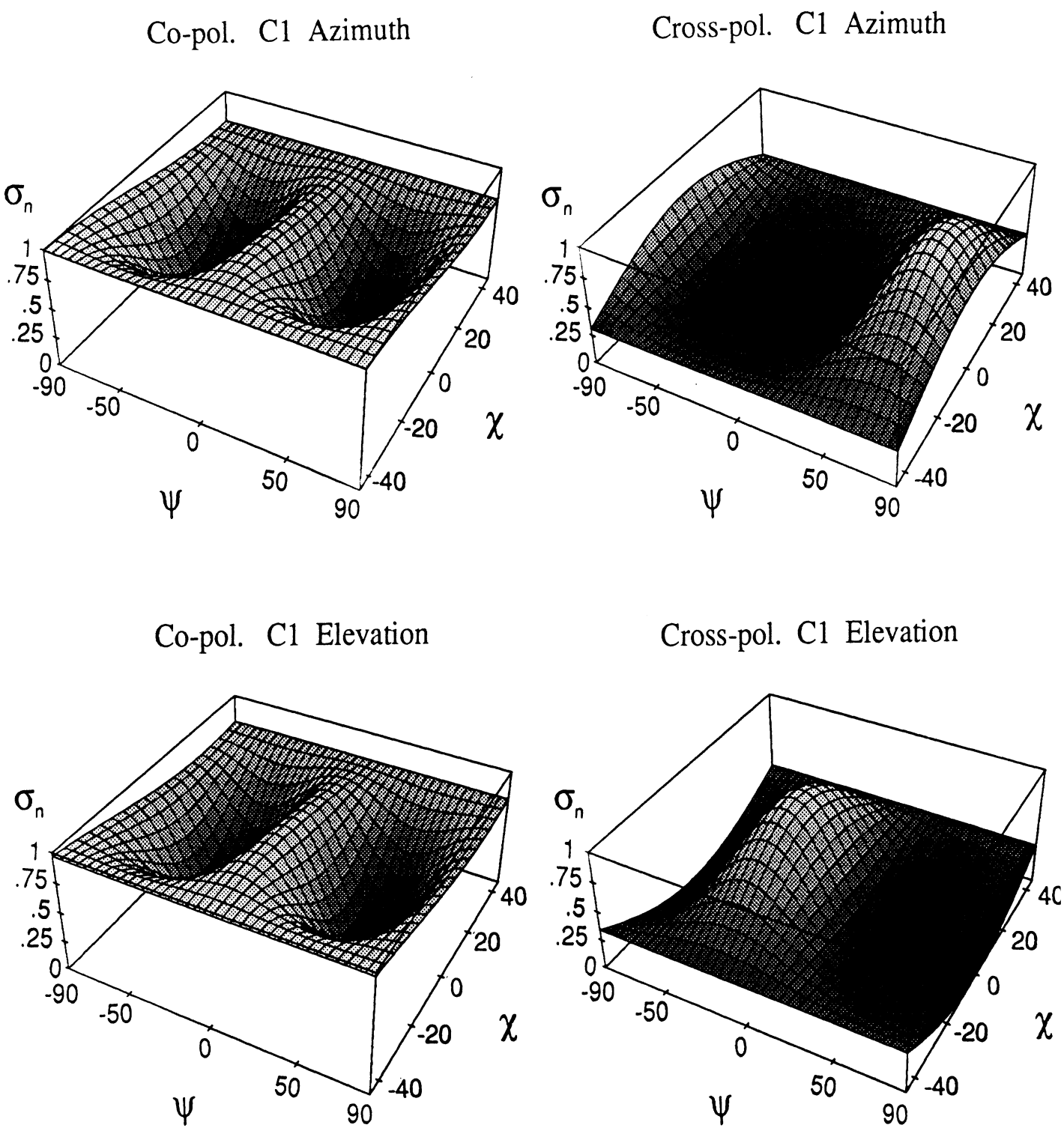

Figure 12: The azimuth and elevation polarization signature for C1 PARC.

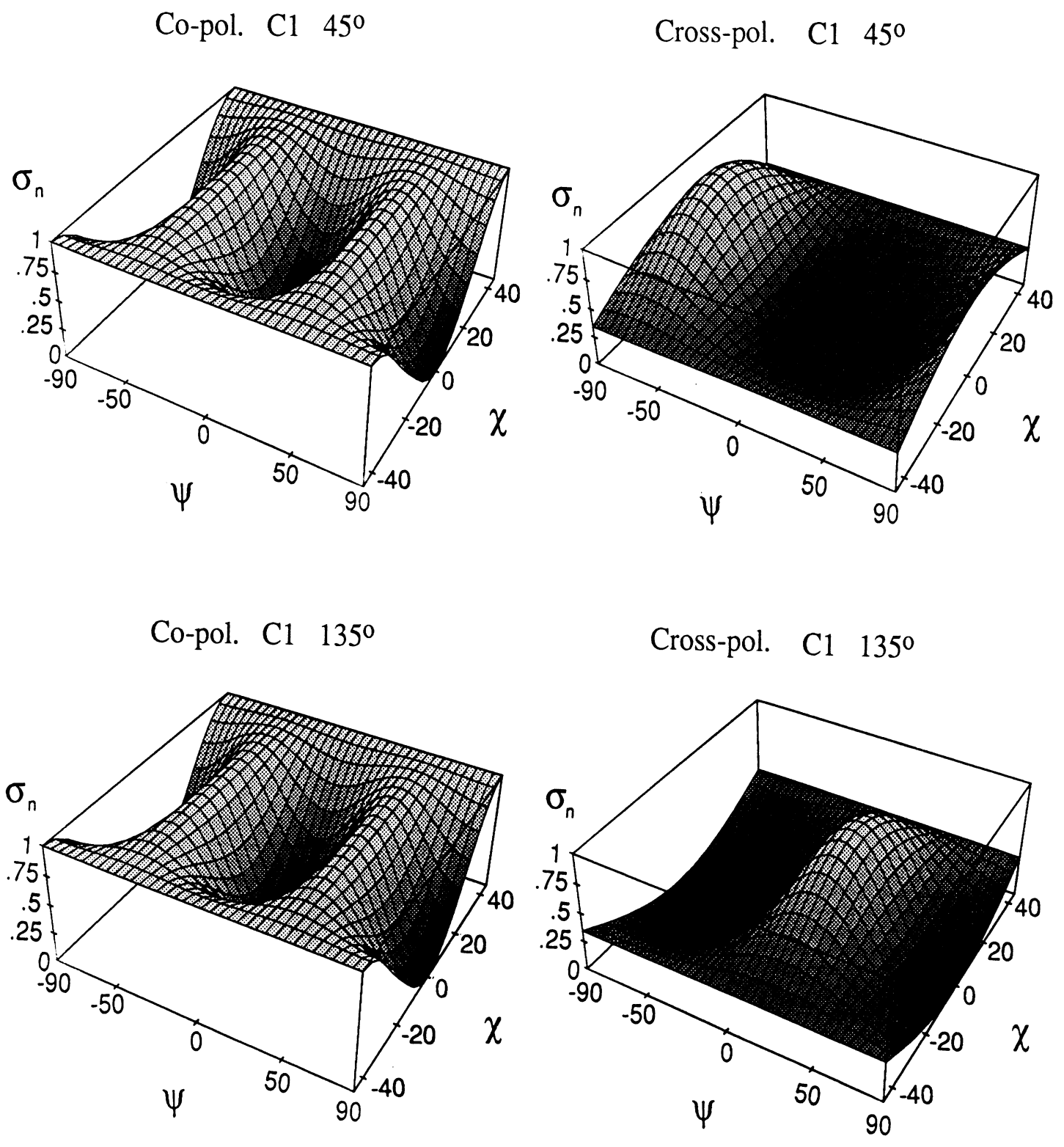

Figure 13: The 45° and 135° polarization signature for C1 PARC.

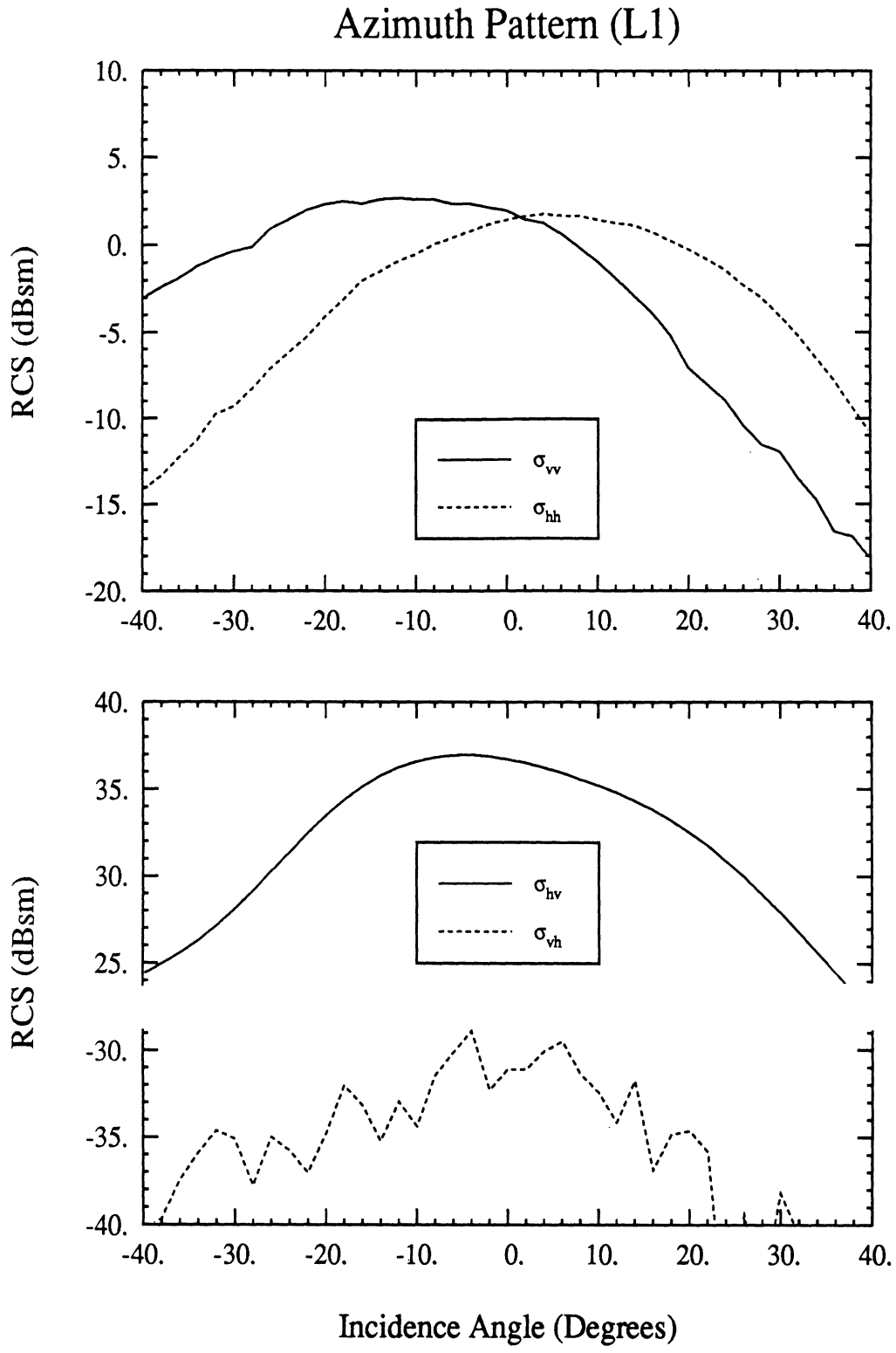

Figure 14: Azimuth pattern of amplitude of scattering matrix elements for L1 PARC.

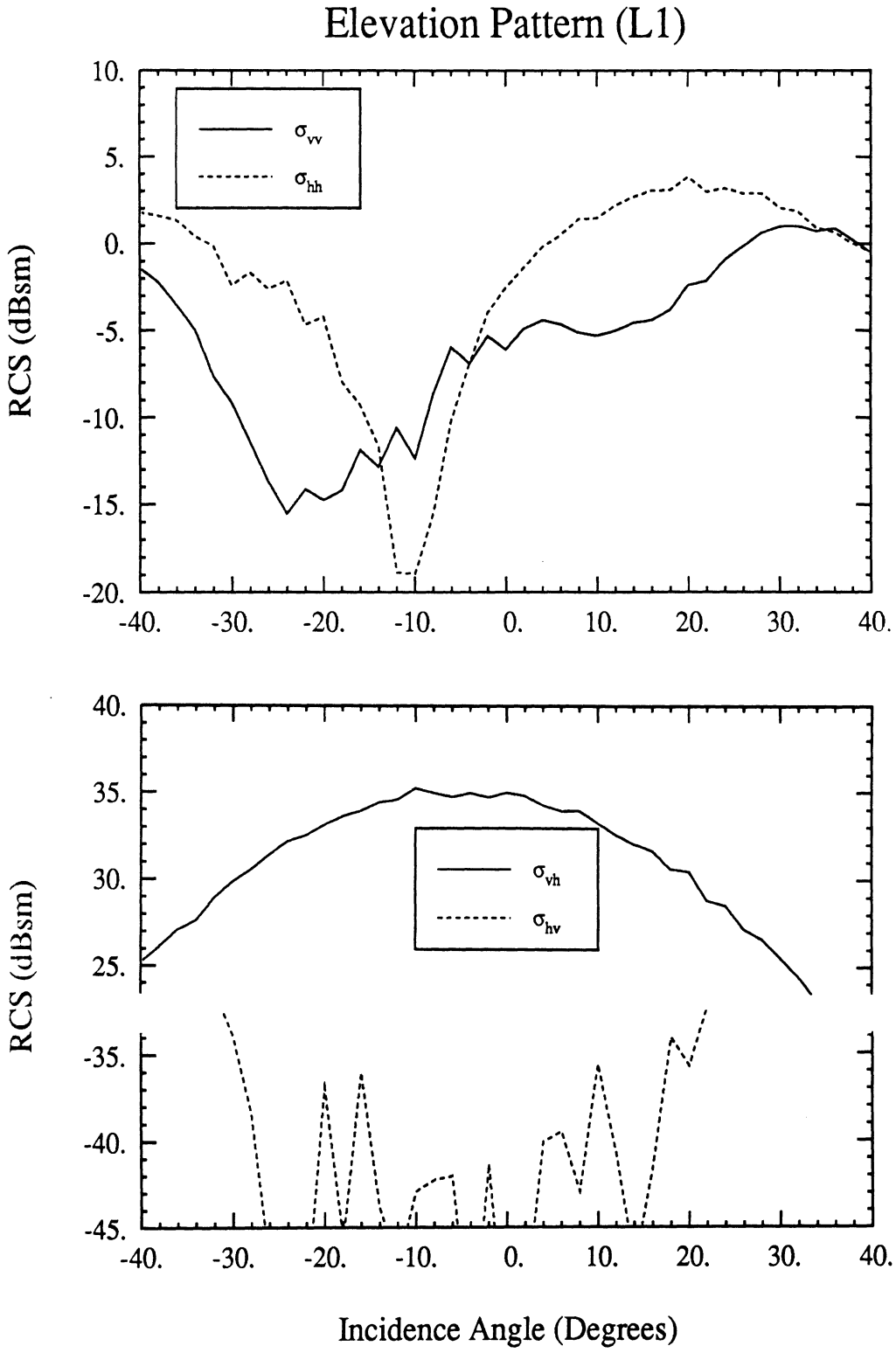

Figure 15: Elevation pattern of amplitude of scattering matrix elements for L1 PARC.

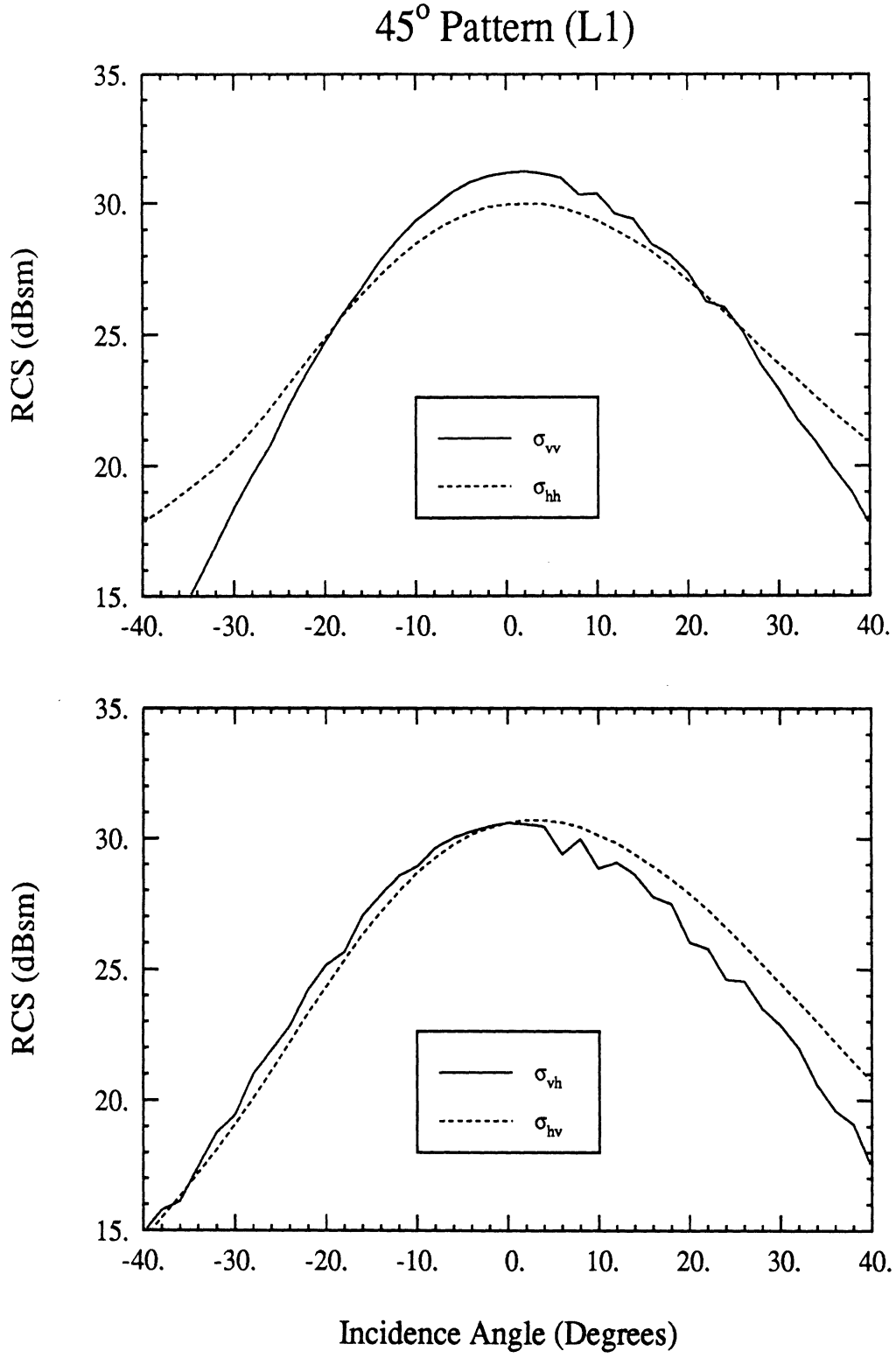

Figure 16: 45° pattern of amplitude of scattering matrix elements for L1 PARC.

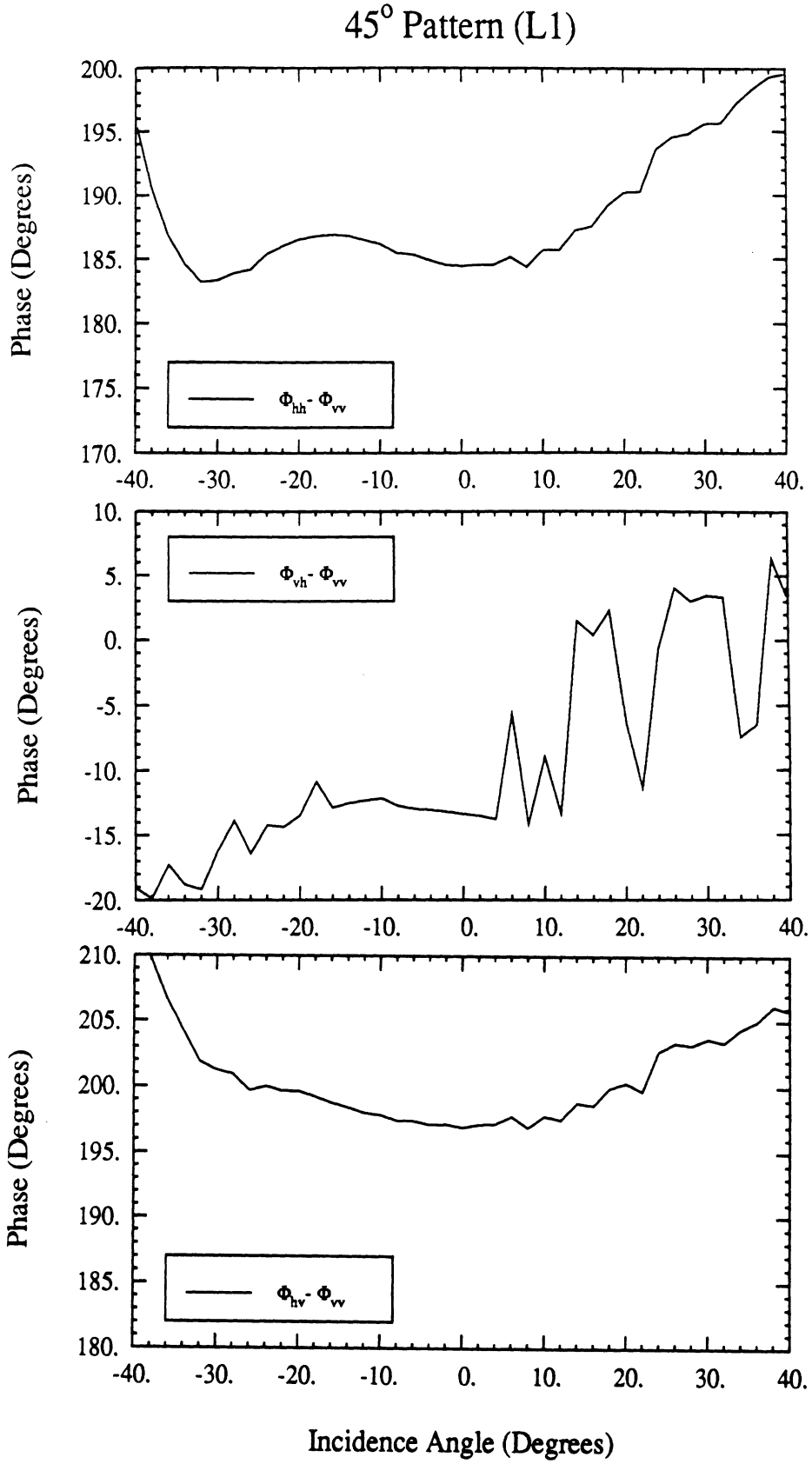

Figure 17: 45° pattern of phase of scattering matrix elements for L1 PARC.

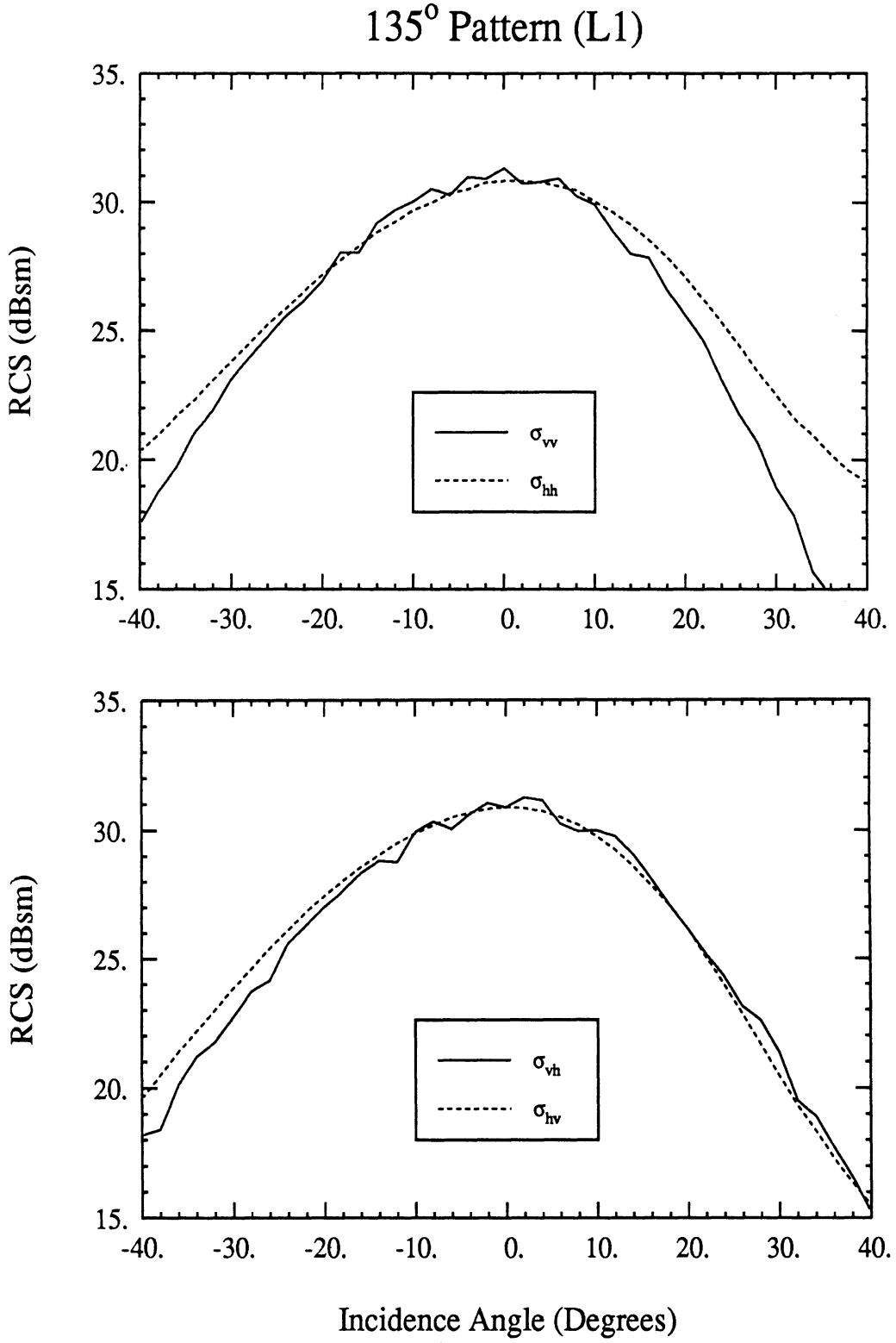

Figure 18: 135° pattern of amplitude of scattering matrix elements for L1 PARC.

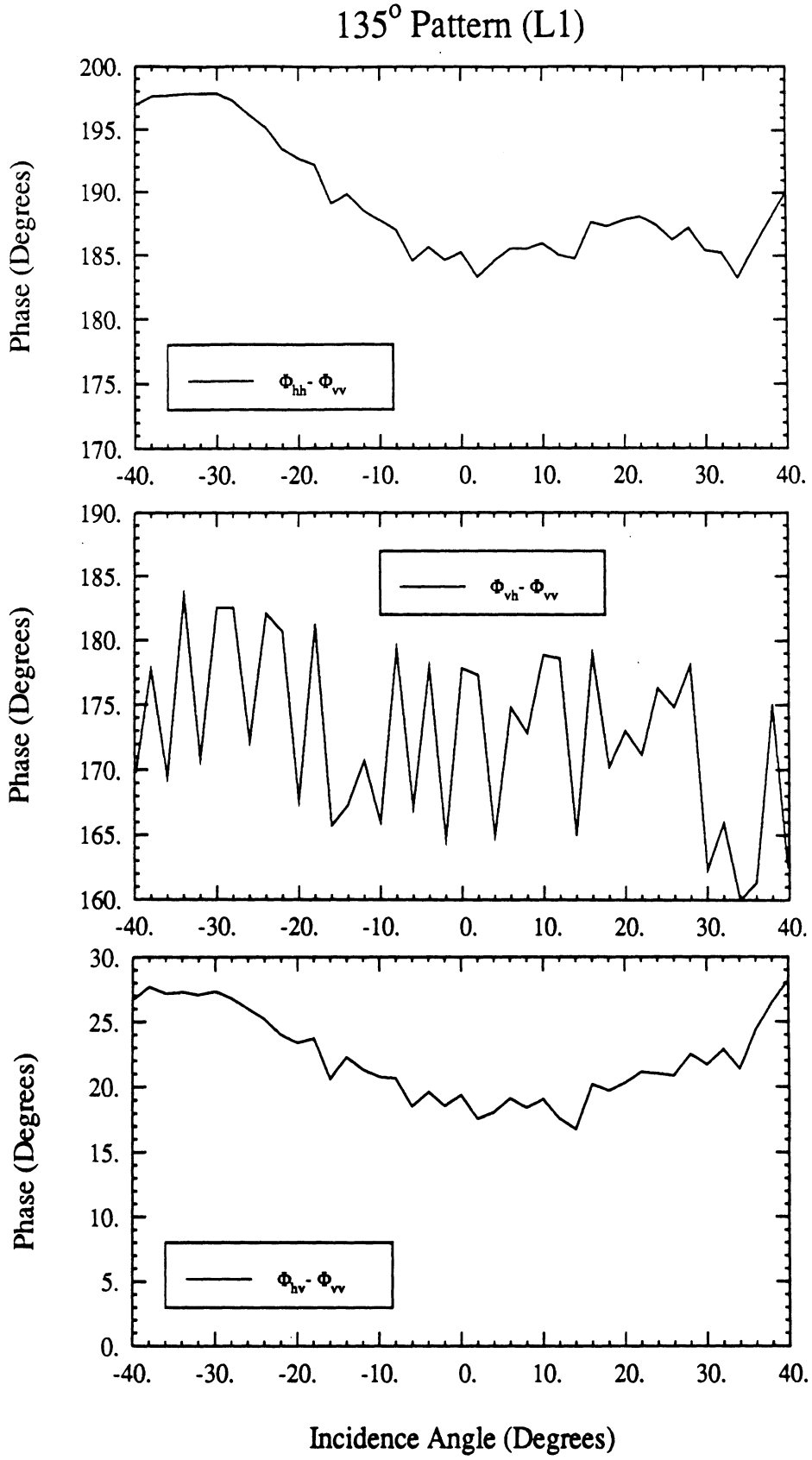

Figure 19: 135° pattern of phase of scattering matrix elements for L1 PARC.

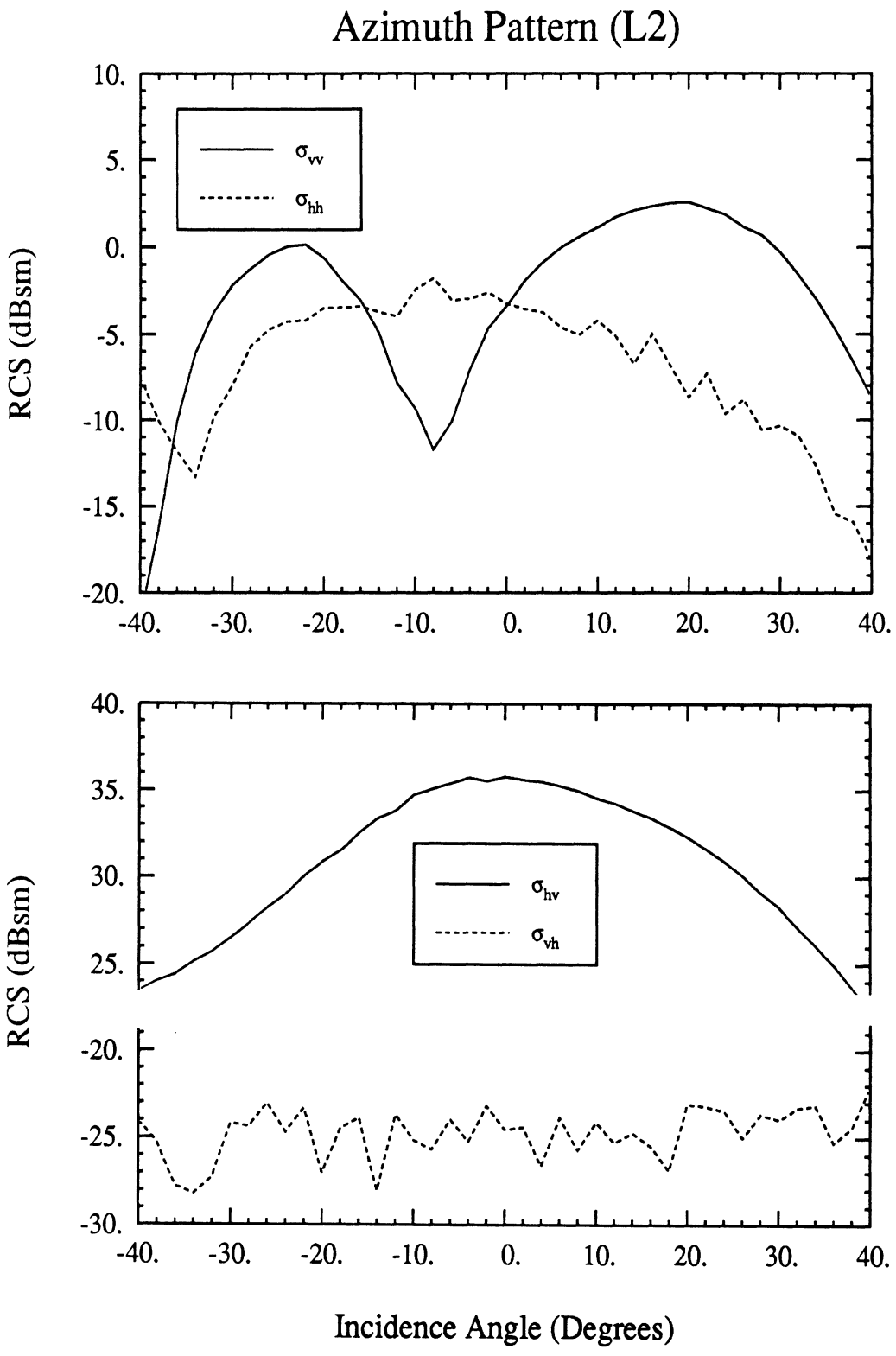

Figure 20: Azimuth pattern of amplitude of scattering matrix elements for L2 PARC.

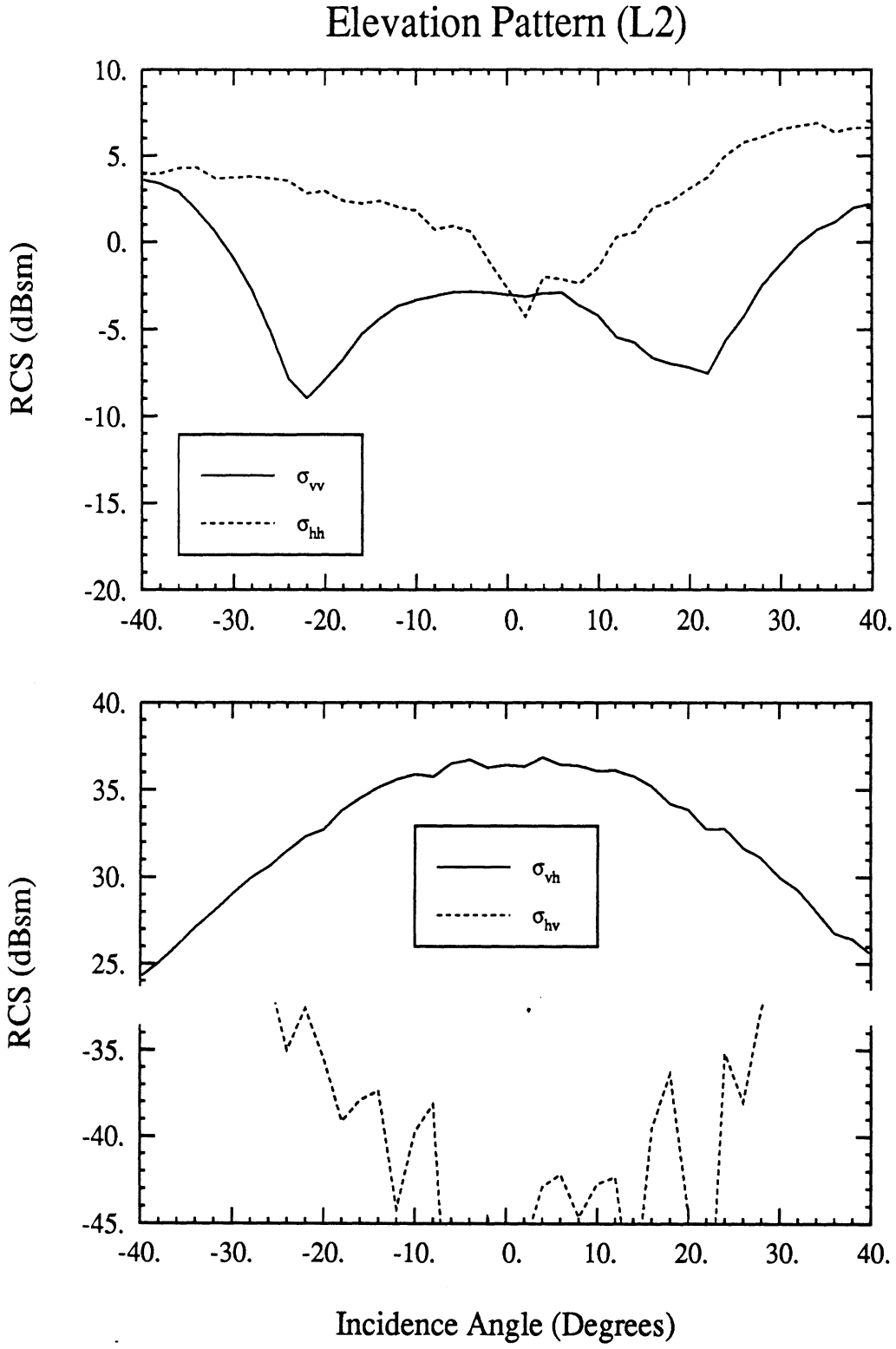

Figure 21: Elevation pattern of amplitude of scattering matrix elements for L2 PARC.

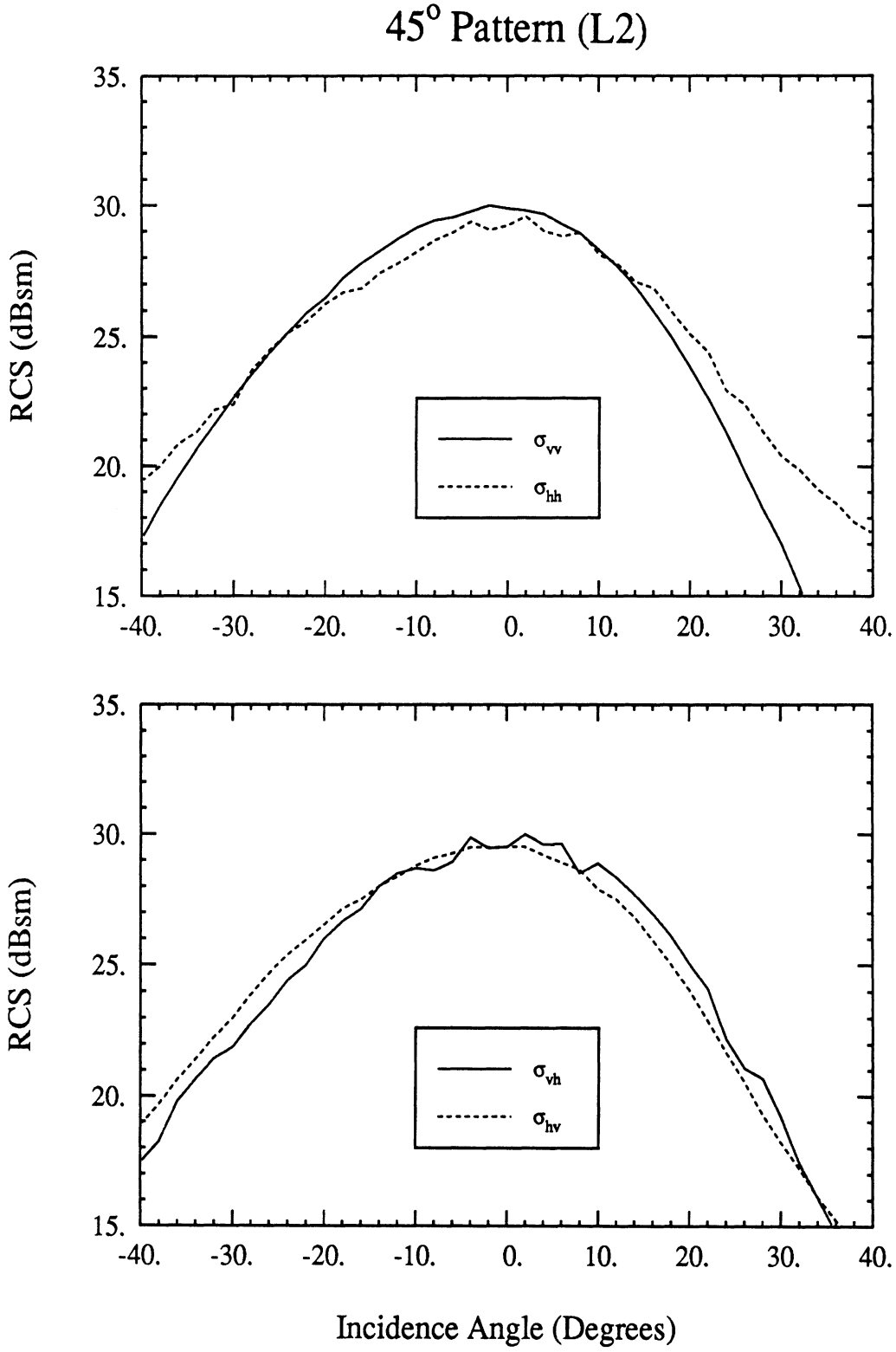

Figure 22: 45° pattern of amplitude of scattering matrix elements for L2 PARC.

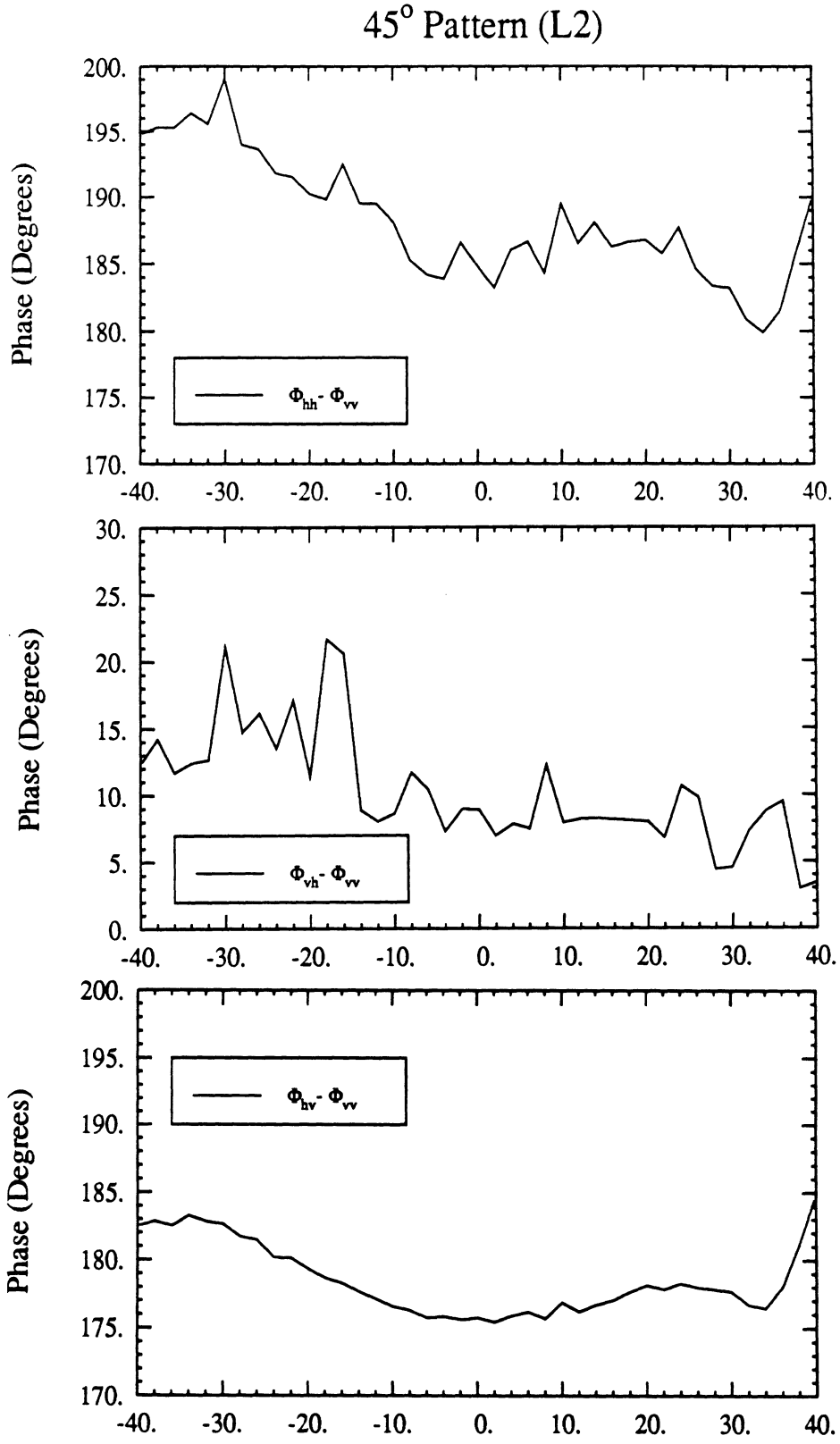

Figure 23: 45° pattern of phase of scattering matrix elements for L2 PARC.

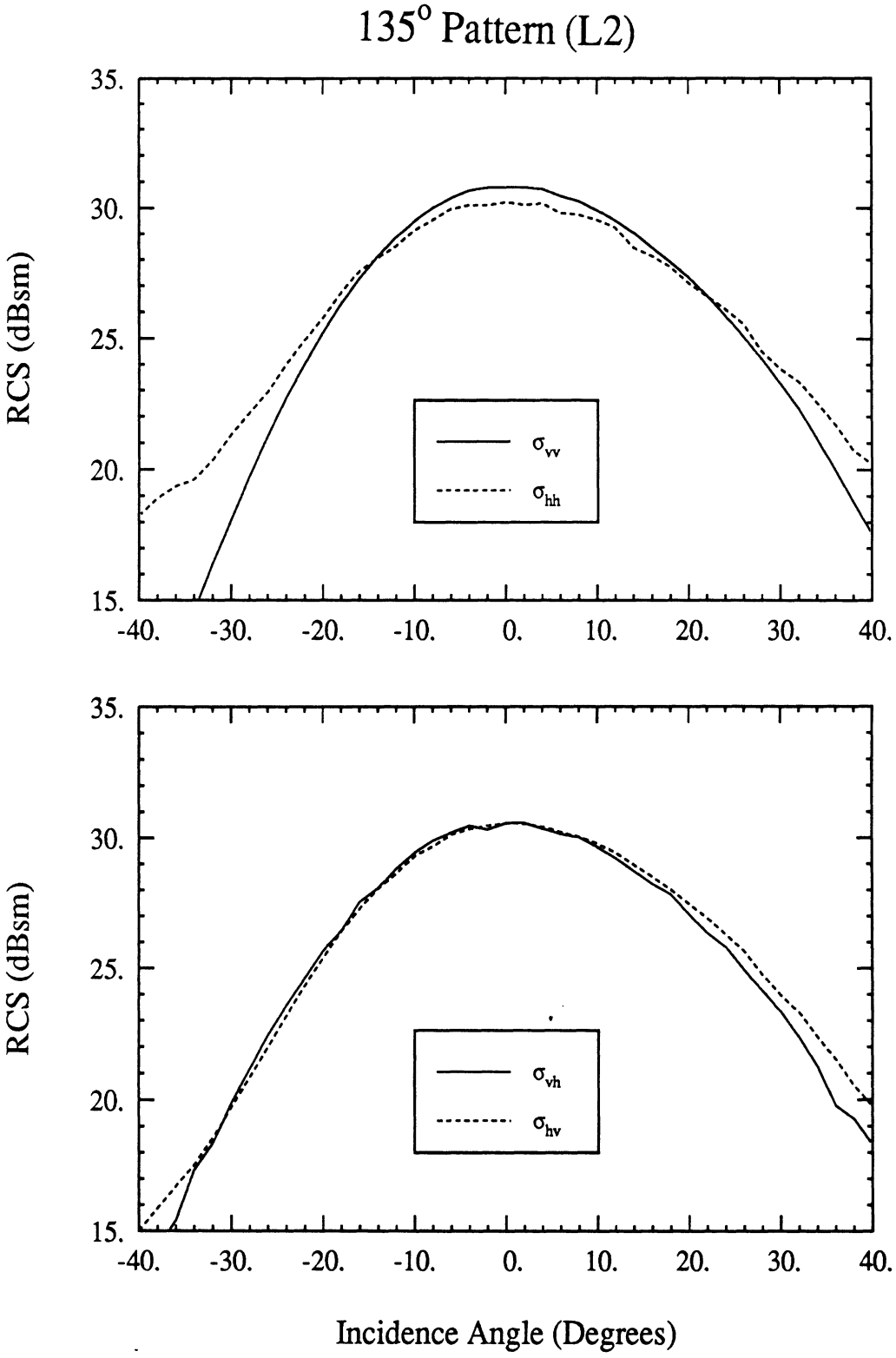

Figure 24: 135° pattern of amplitude of scattering matrix elements for L2 PARC.

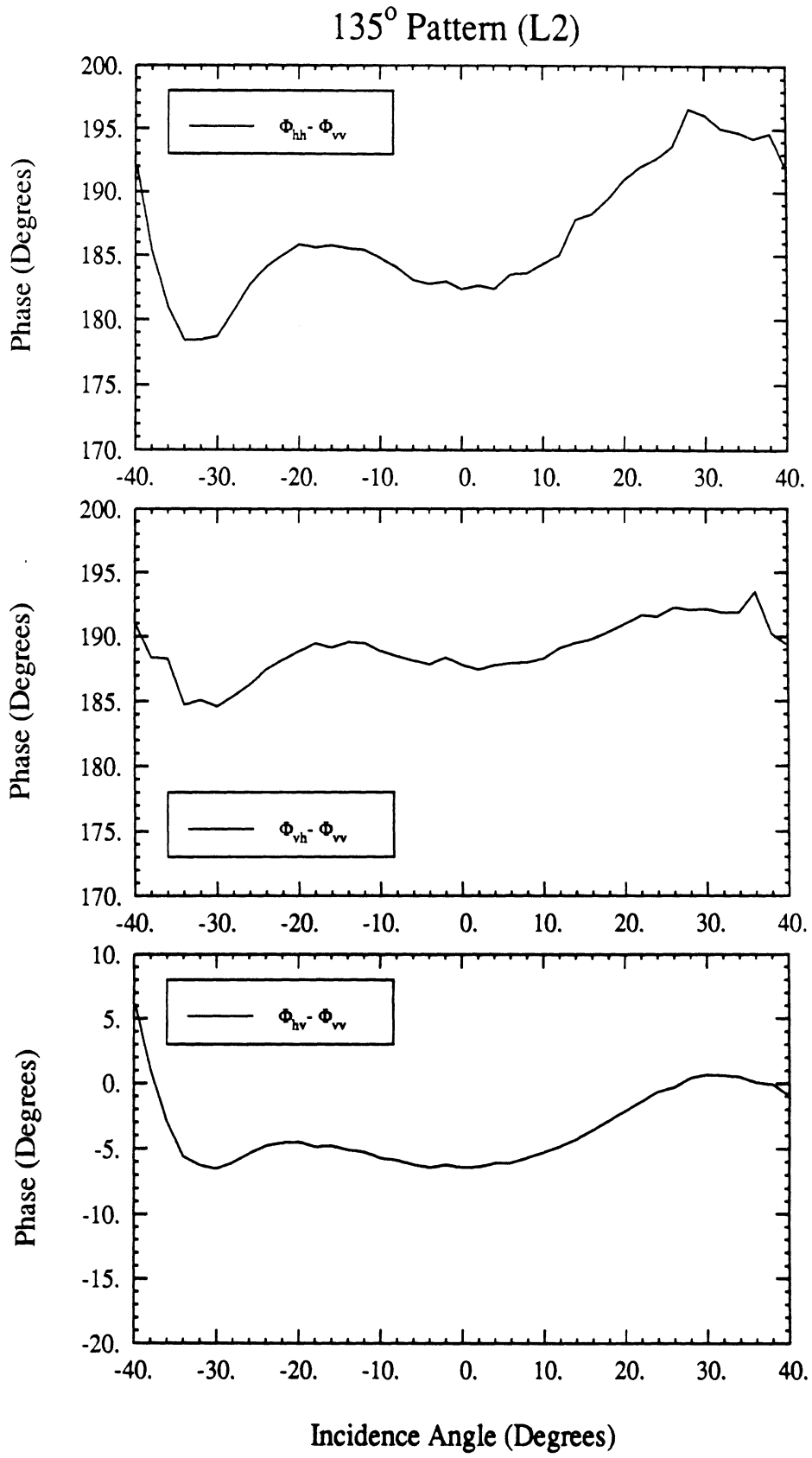

Figure 25: 135° pattern of phase of scattering matrix elements for L2 PARC.

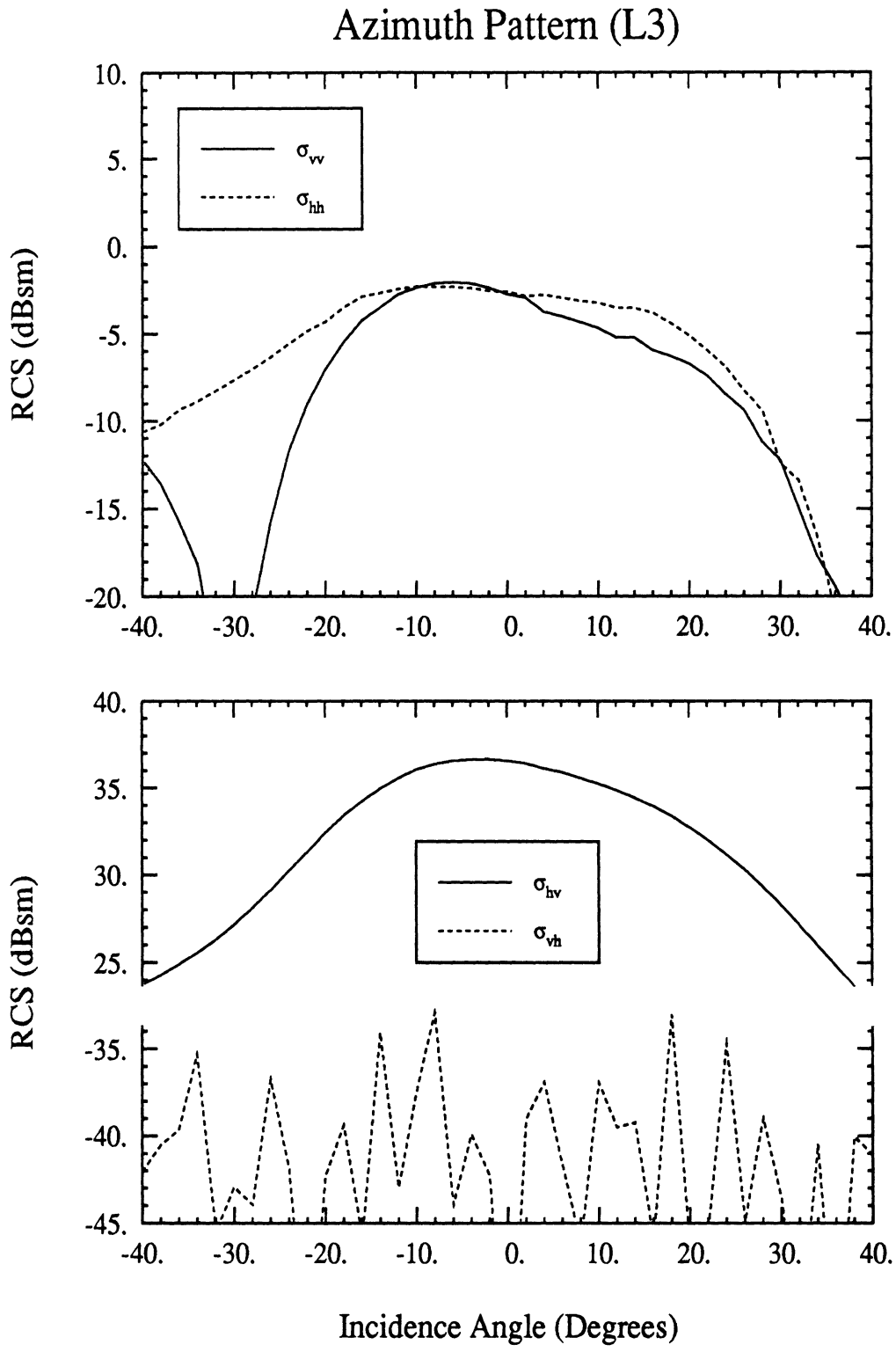

Figure 26: Azimuth pattern of amplitude of scattering matrix elements for L3 PARC.

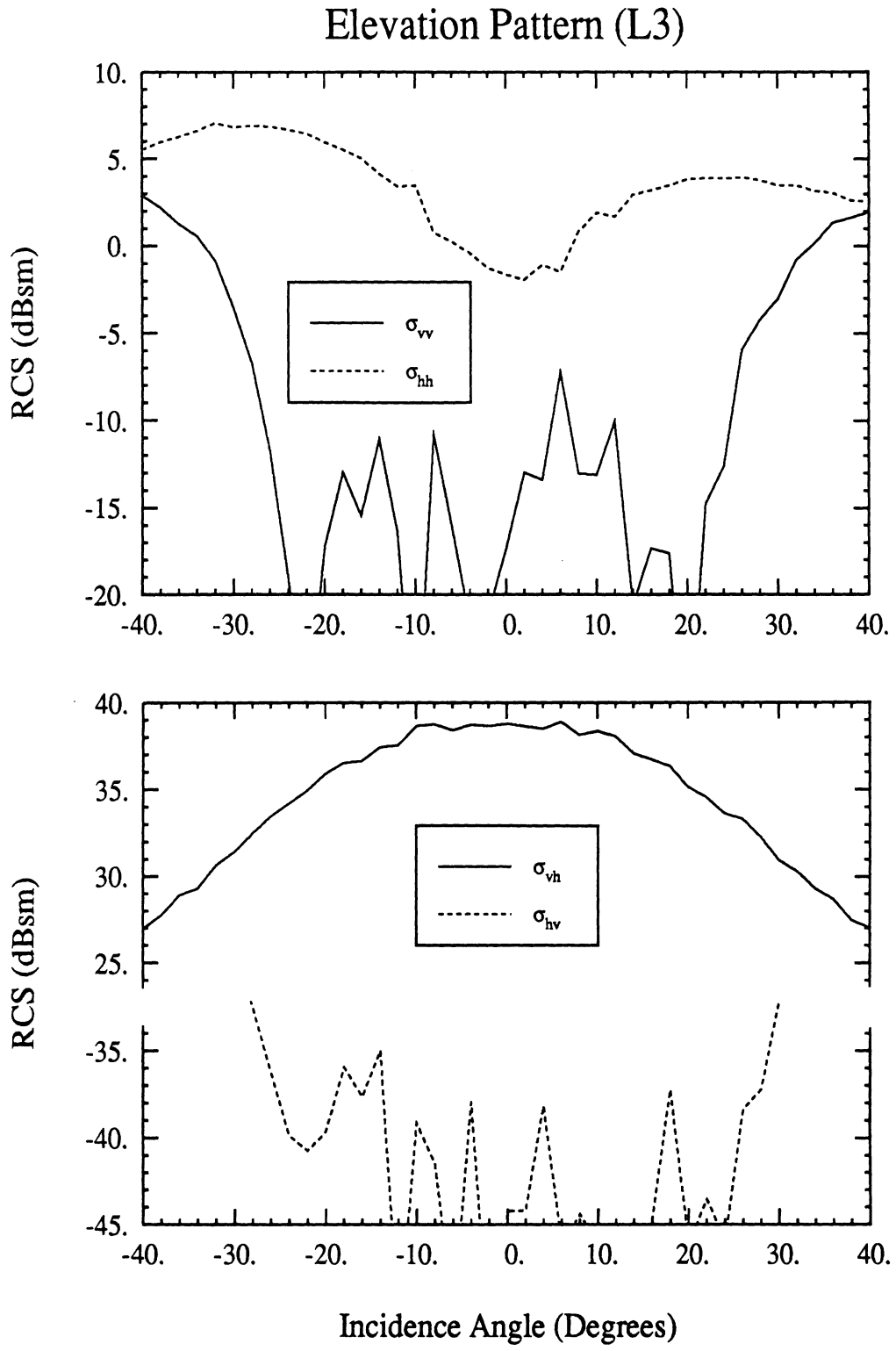

Figure 27: Elevation pattern of amplitude of scattering matrix elements for L3 PARC.

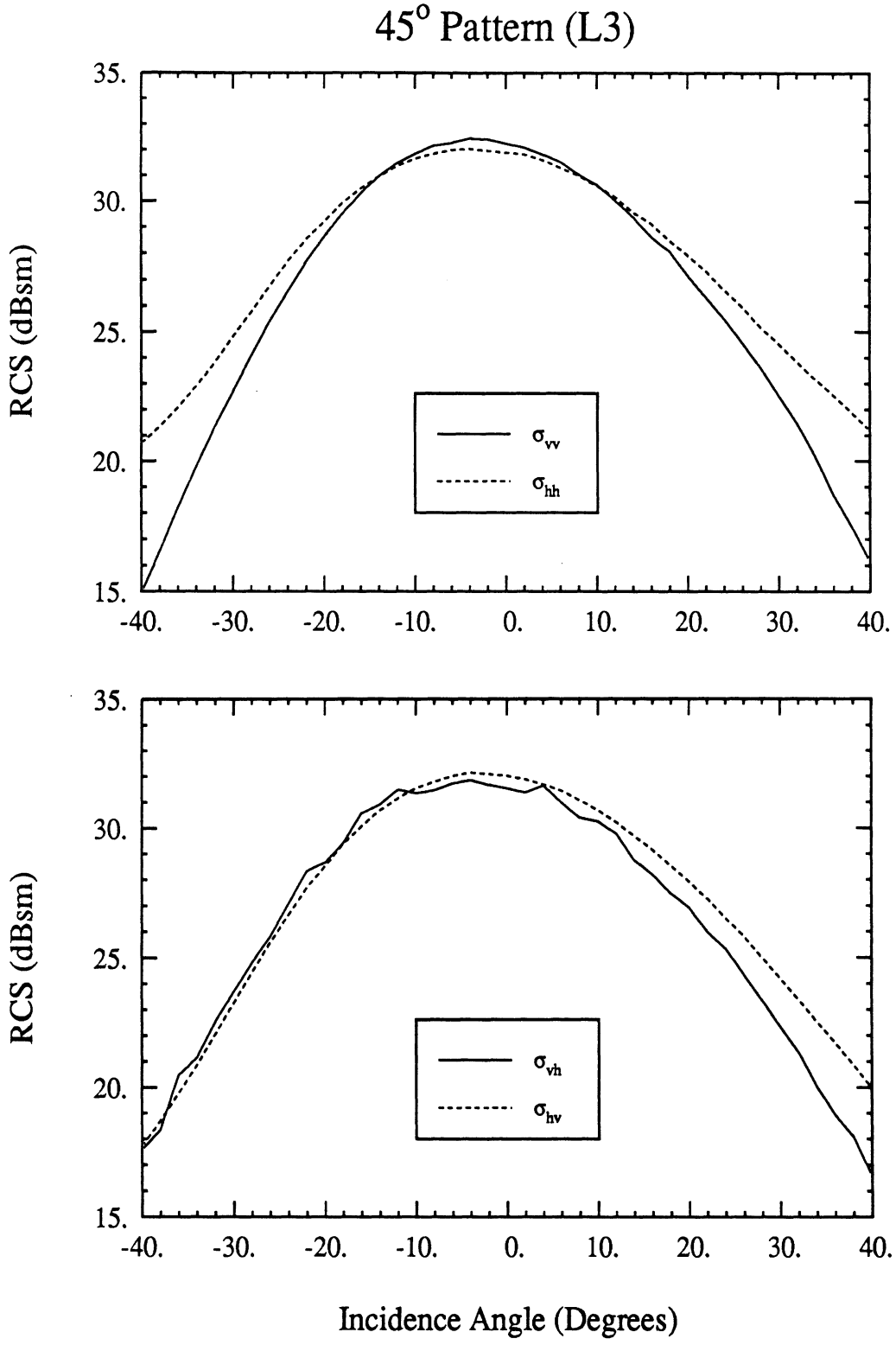

Figure 28: 45° pattern of amplitude of scattering matrix elements for L3 PARC.

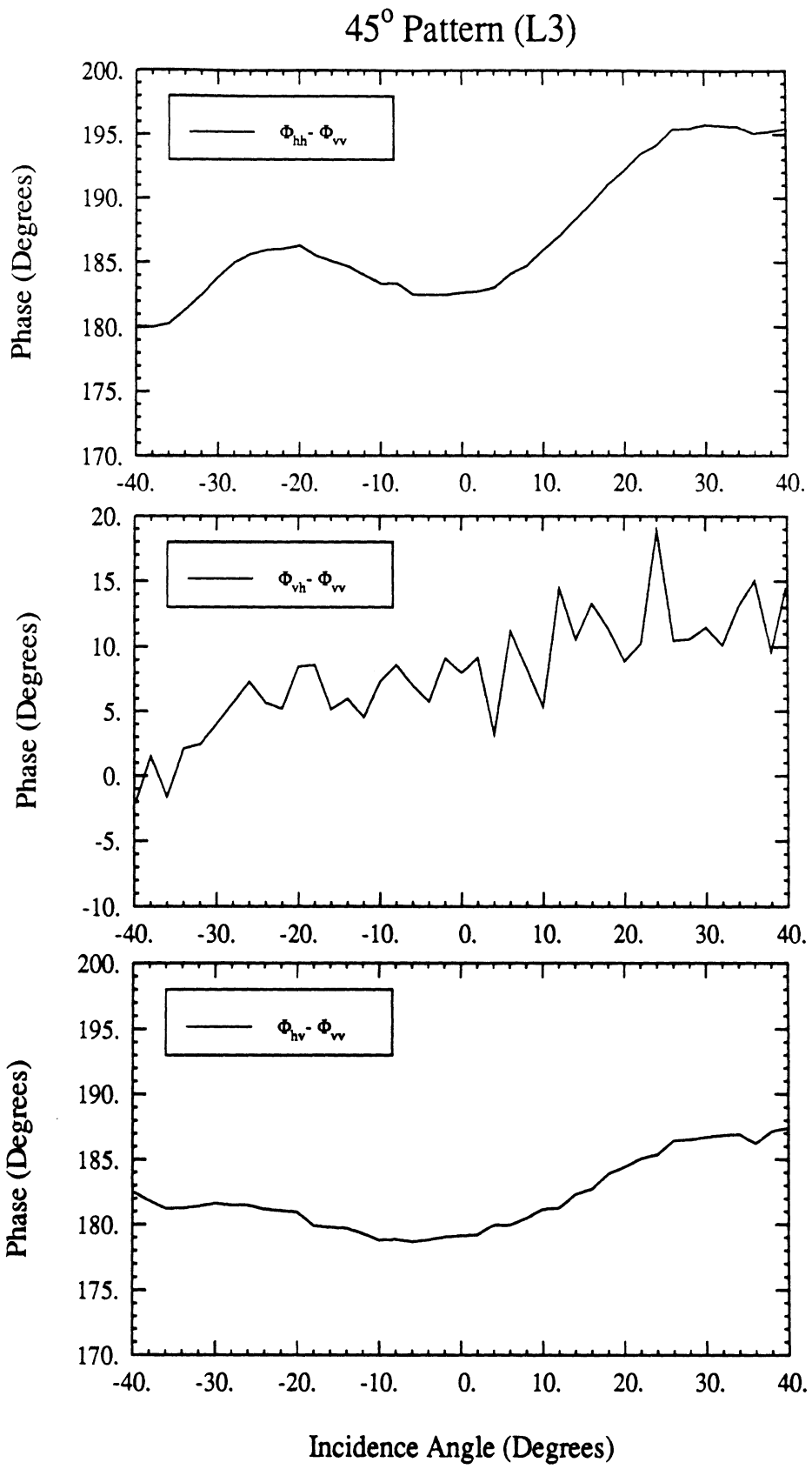

Figure 29: 45° pattern of phase of scattering matrix elements for L3 PARC.

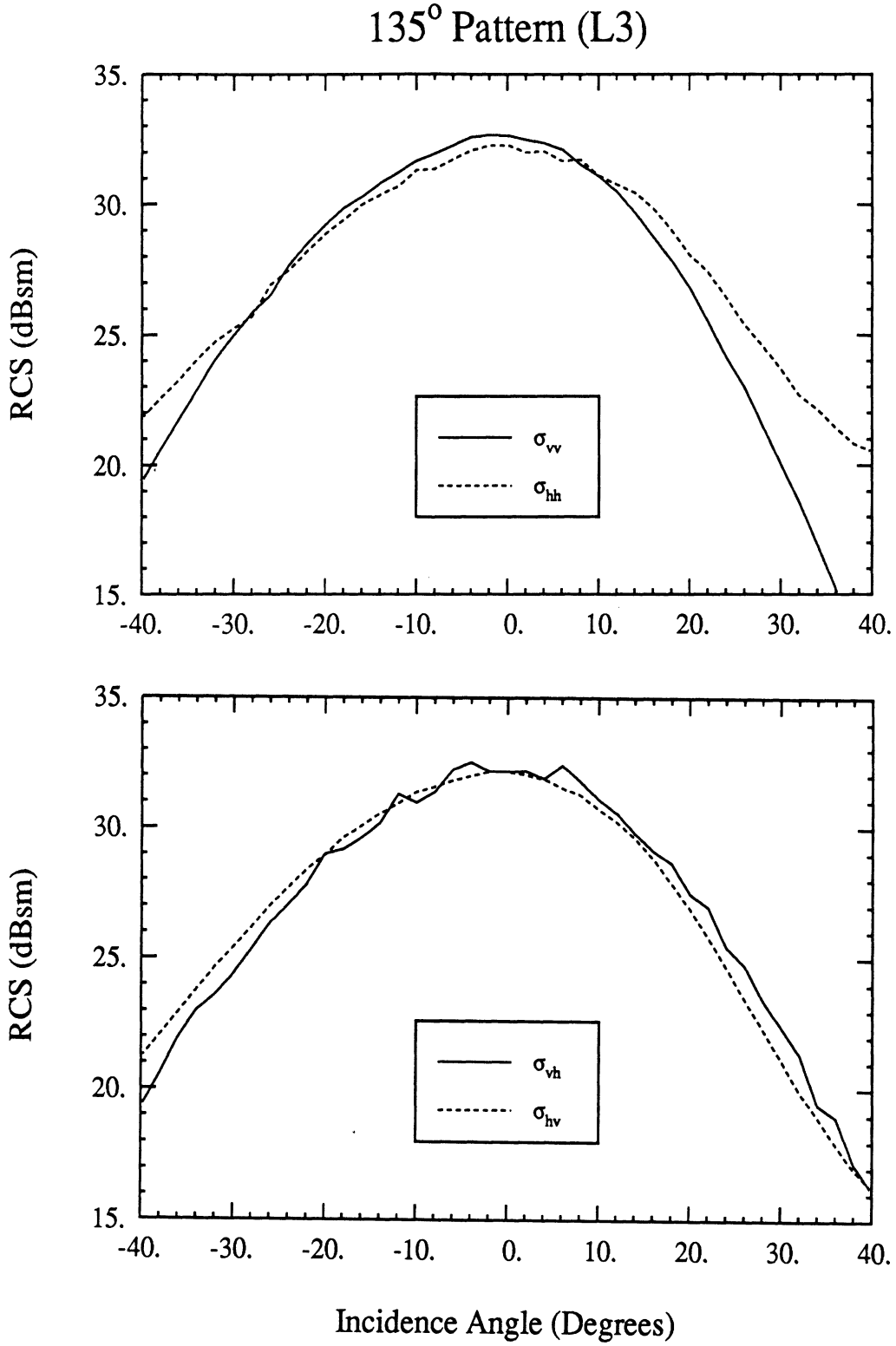

Figure 30: 135° pattern of amplitude of scattering matrix elements for L3 PARC.

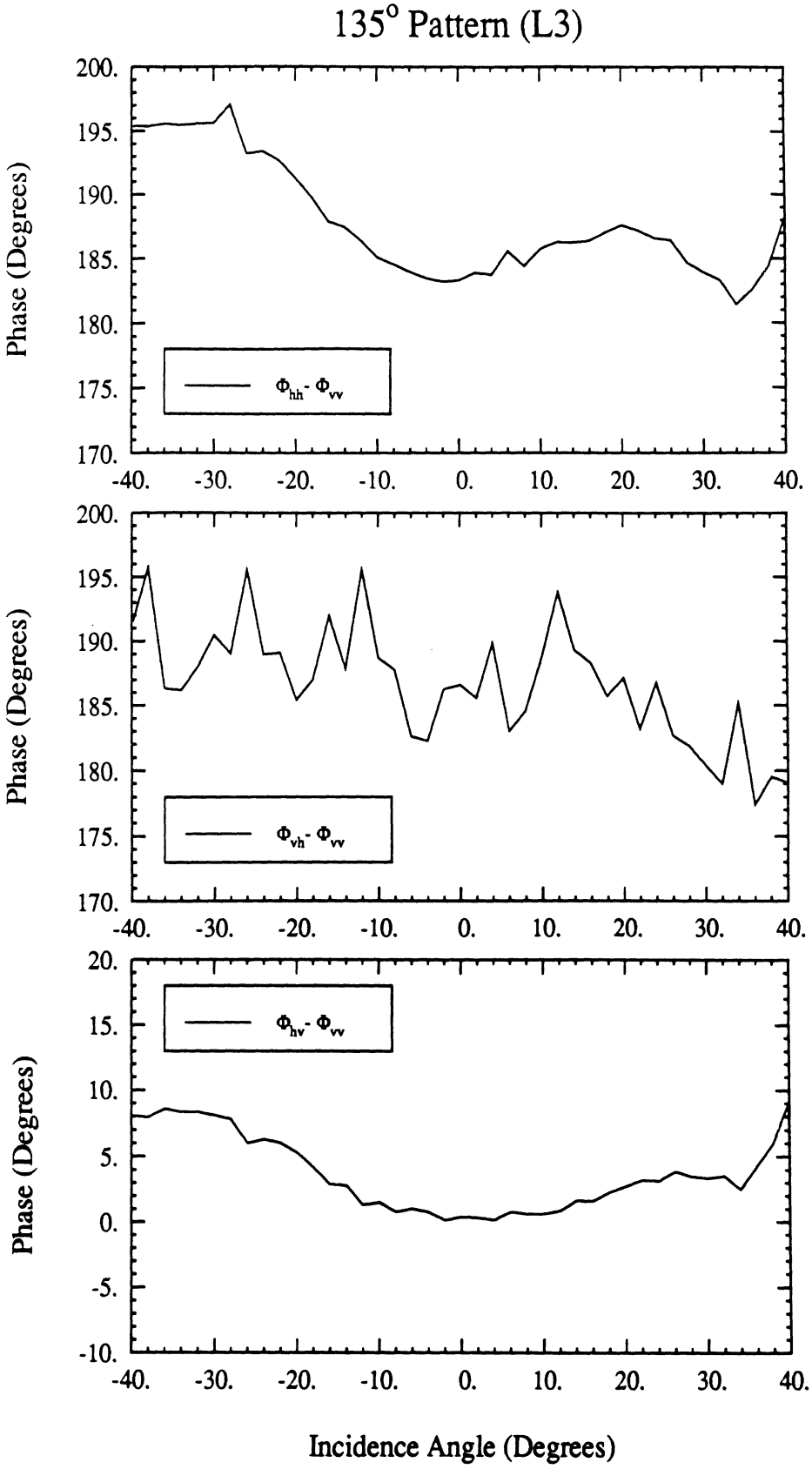

Figure 31: 135° pattern of phase of scattering matrix elements for L3 PARC.

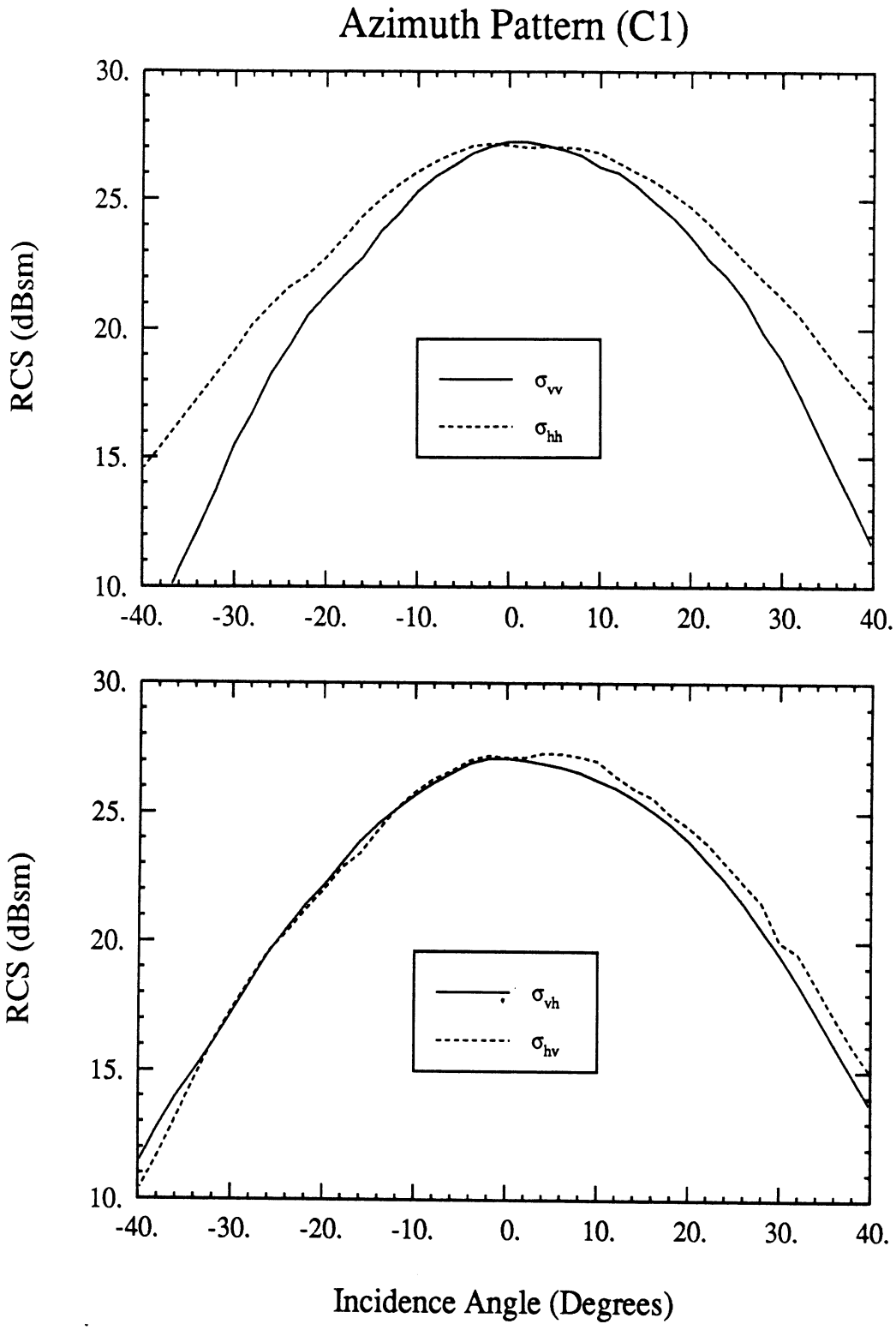

Figure 32: Azimuth pattern of amplitude of scattering matrix elements for C1 PARC.

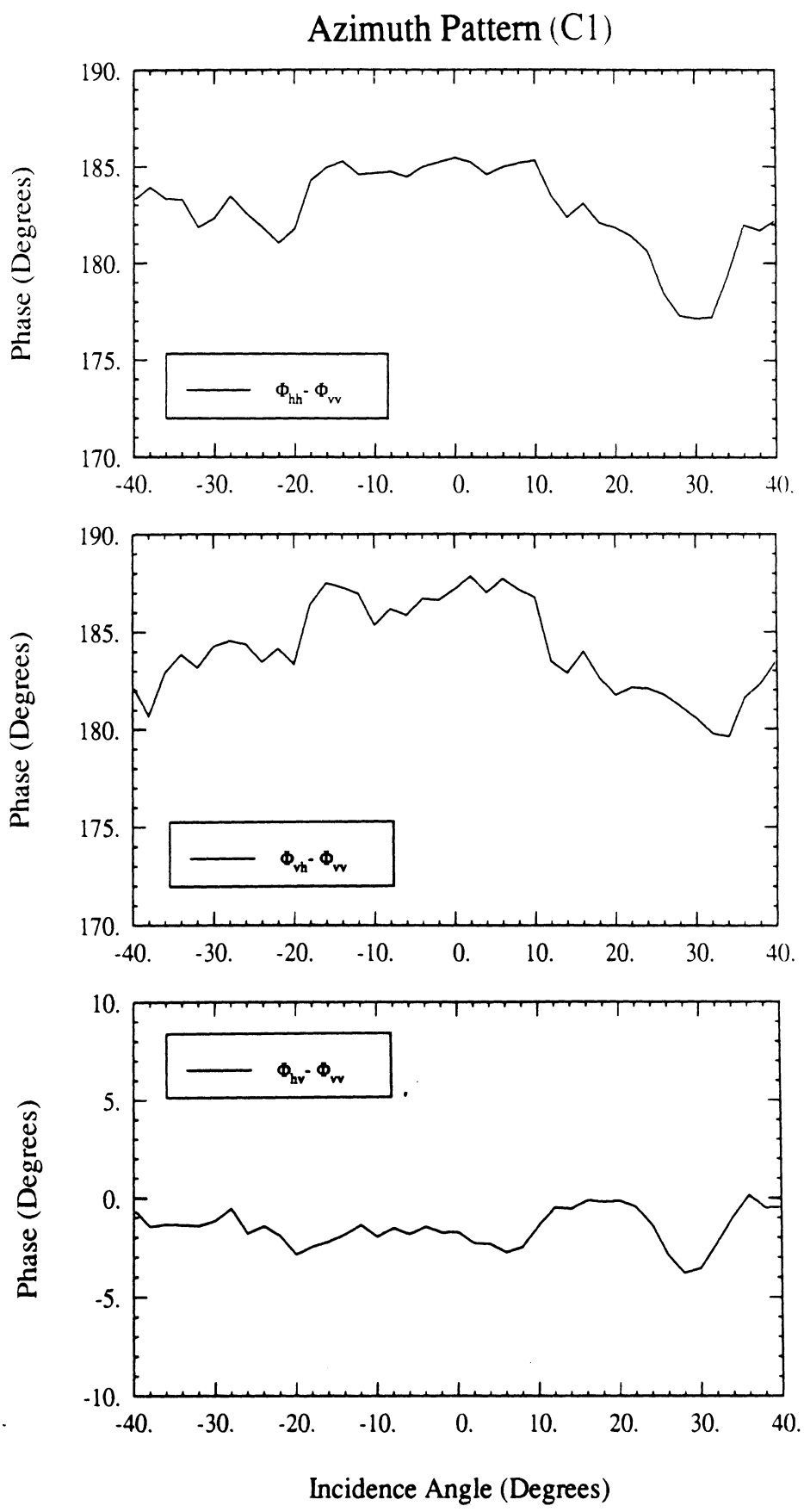

Figure 33: Azimuth pattern of phase of scattering matrix elements for C1 PARC.

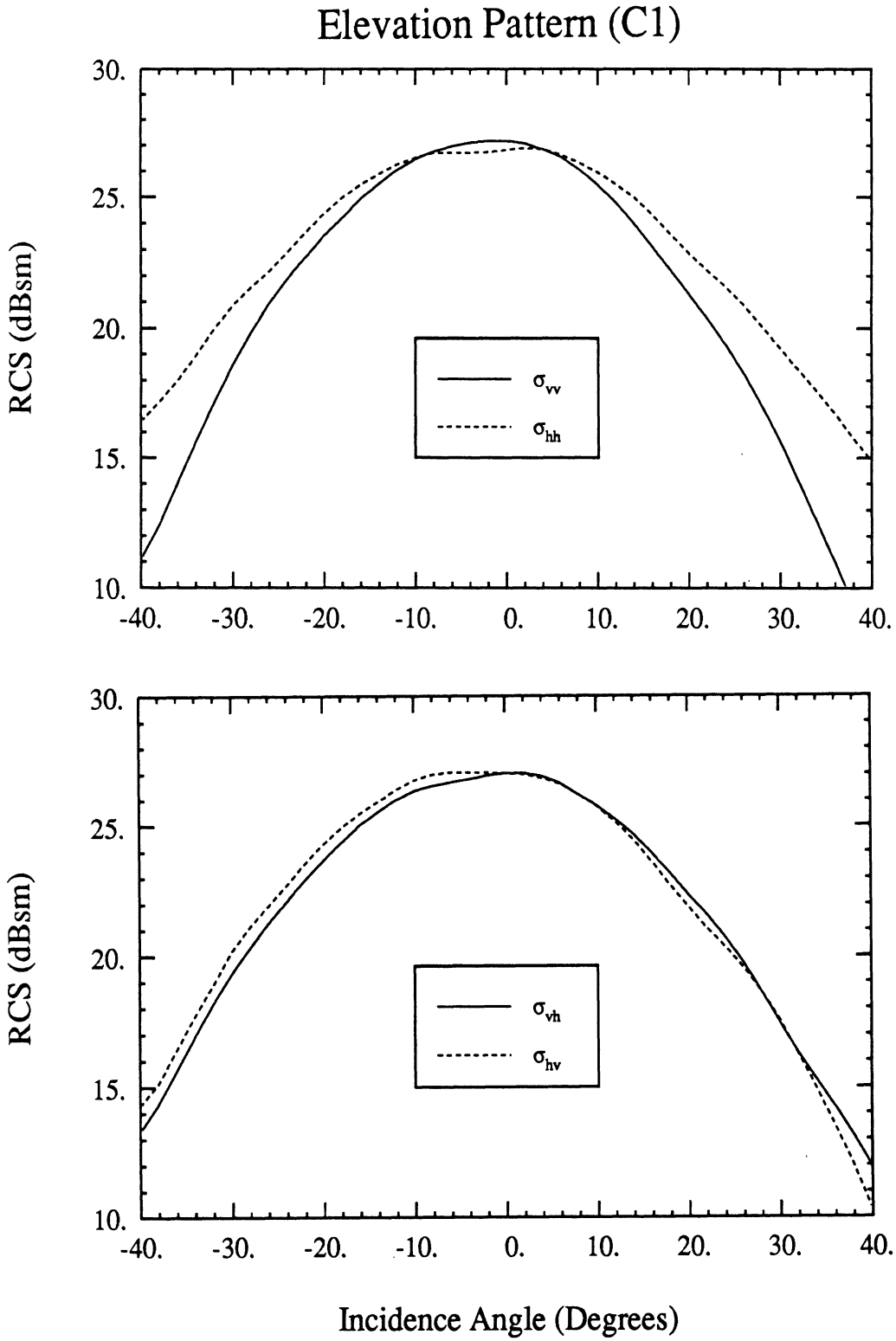

Figure 34: Elevation pattern of amplitude of scattering matrix elements for C1 PARC.

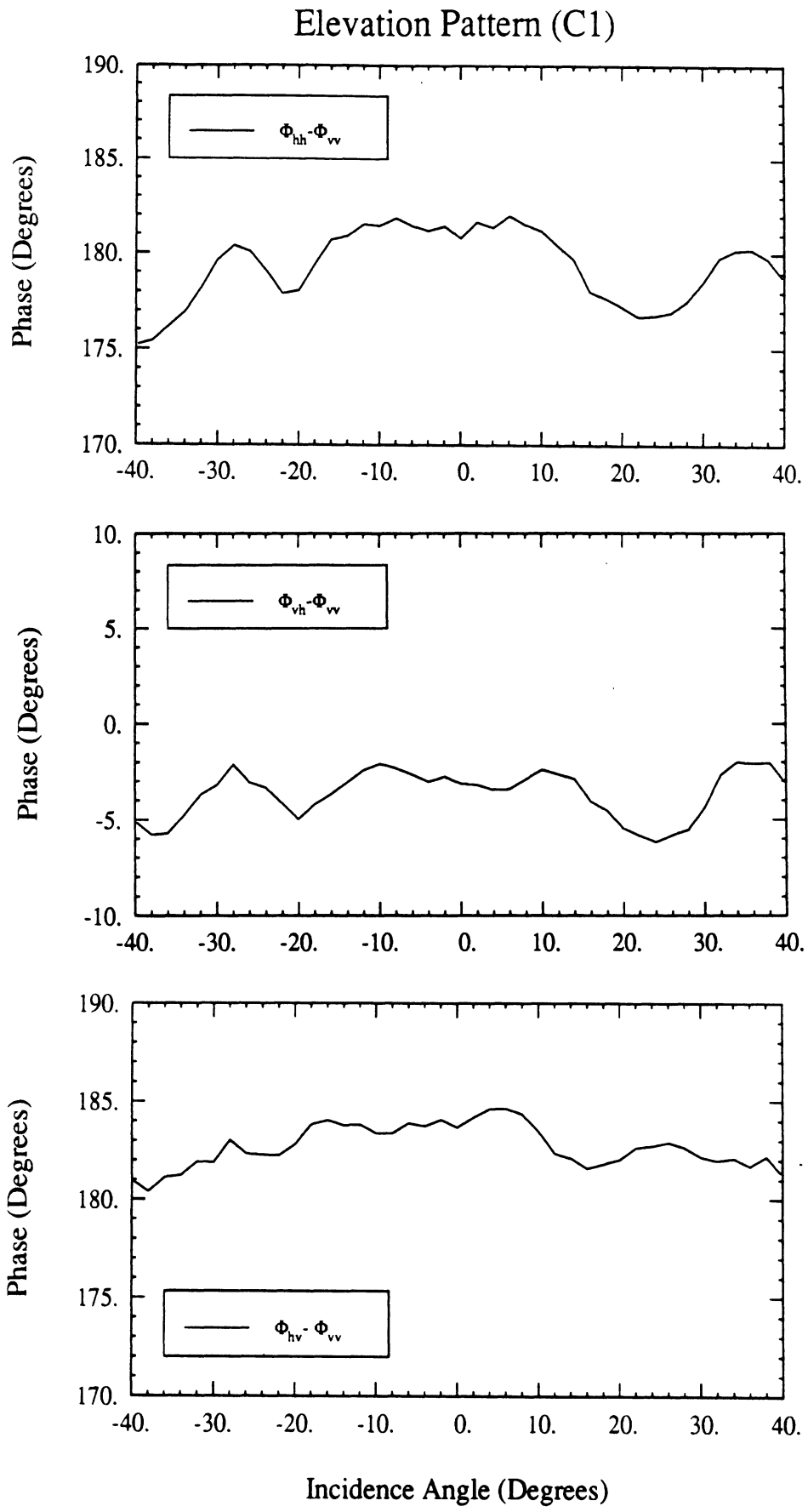

Figure 35: Elevation pattern of phase of scattering matrix elements for C1 PARC.

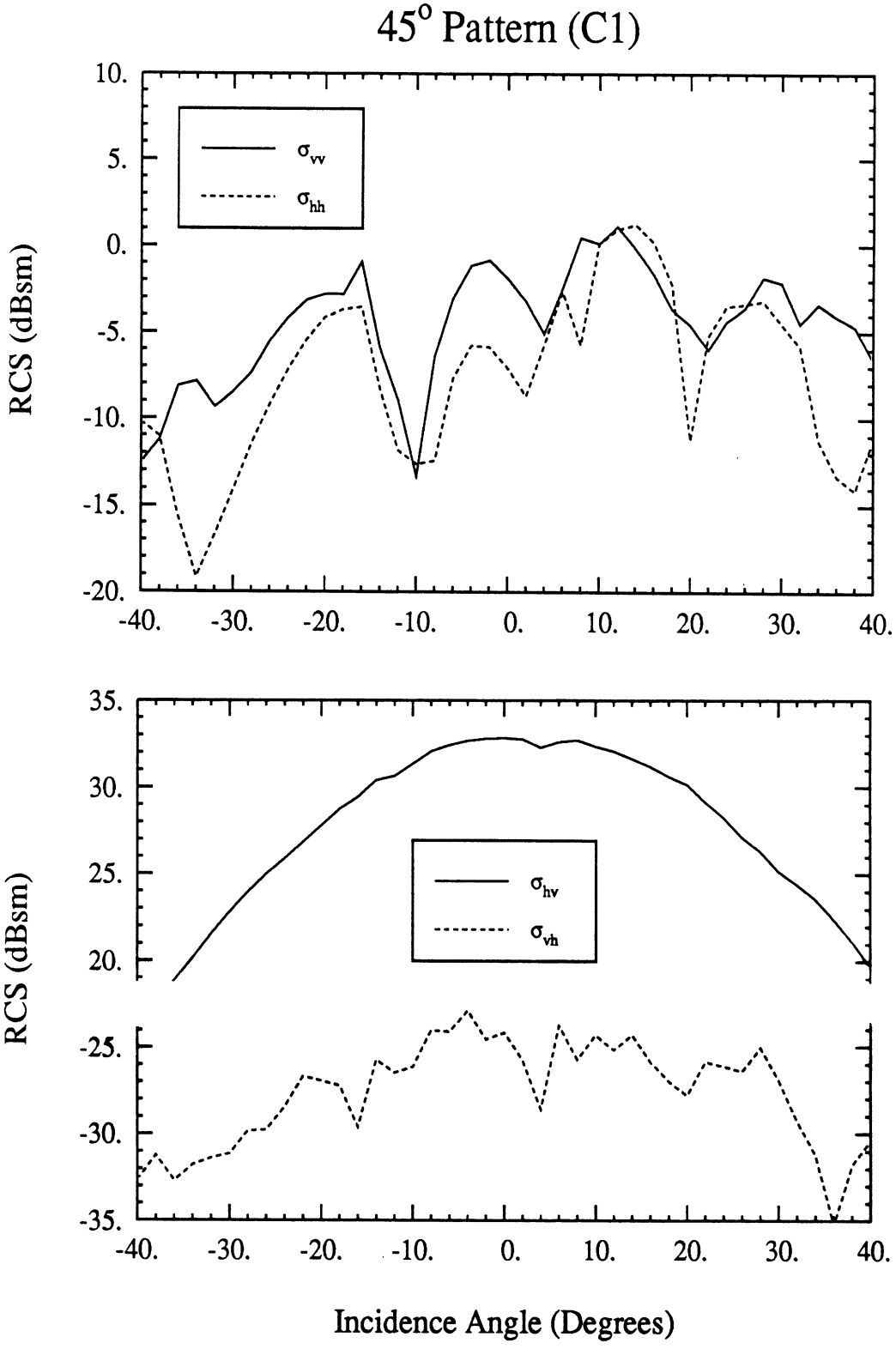

Figure 36: 45° pattern of amplitude of scattering matrix elements for C1 PARC.

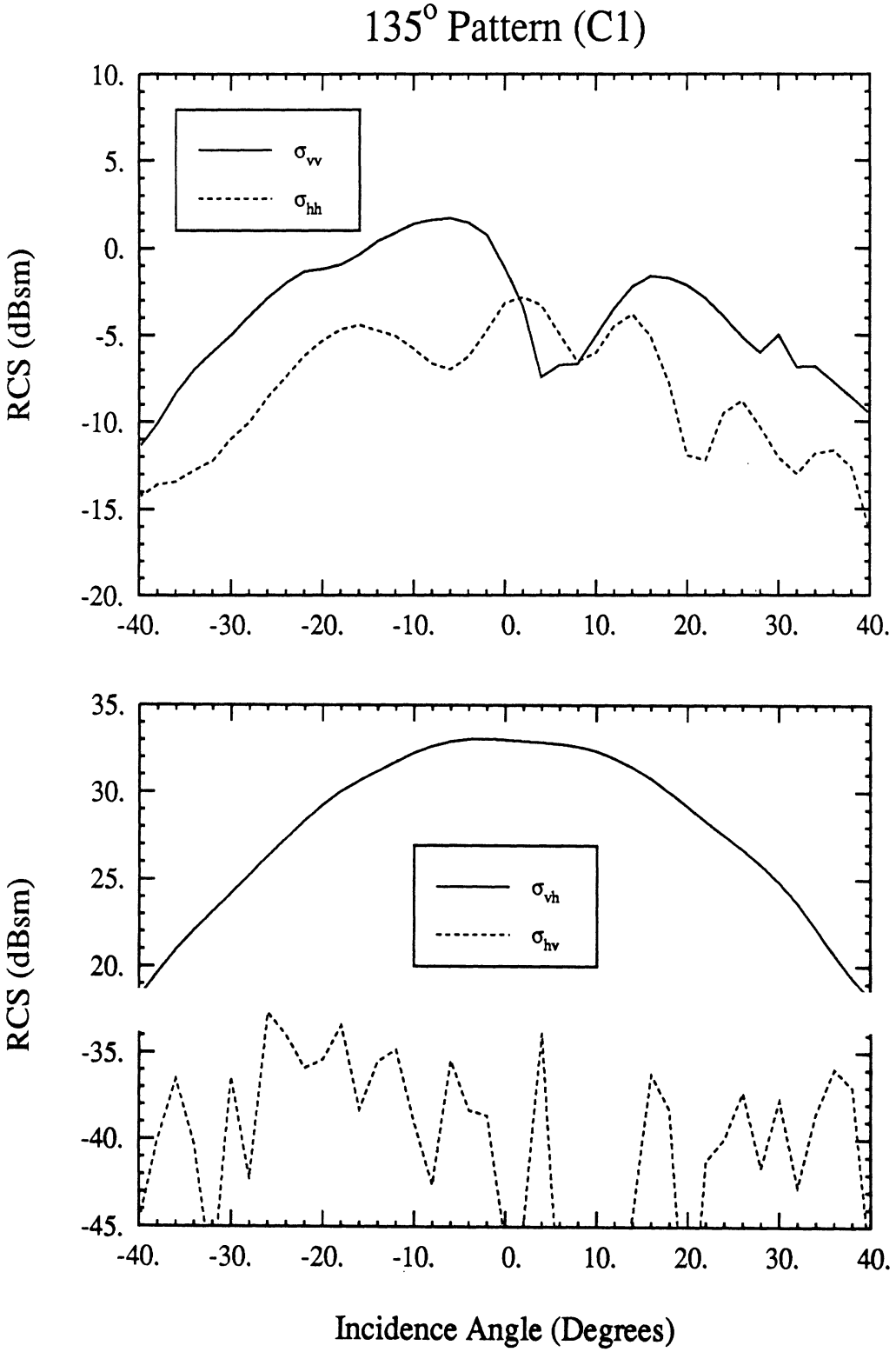

Figure 37: 135° pattern of amplitude of scattering matrix elements for C1 PARC.

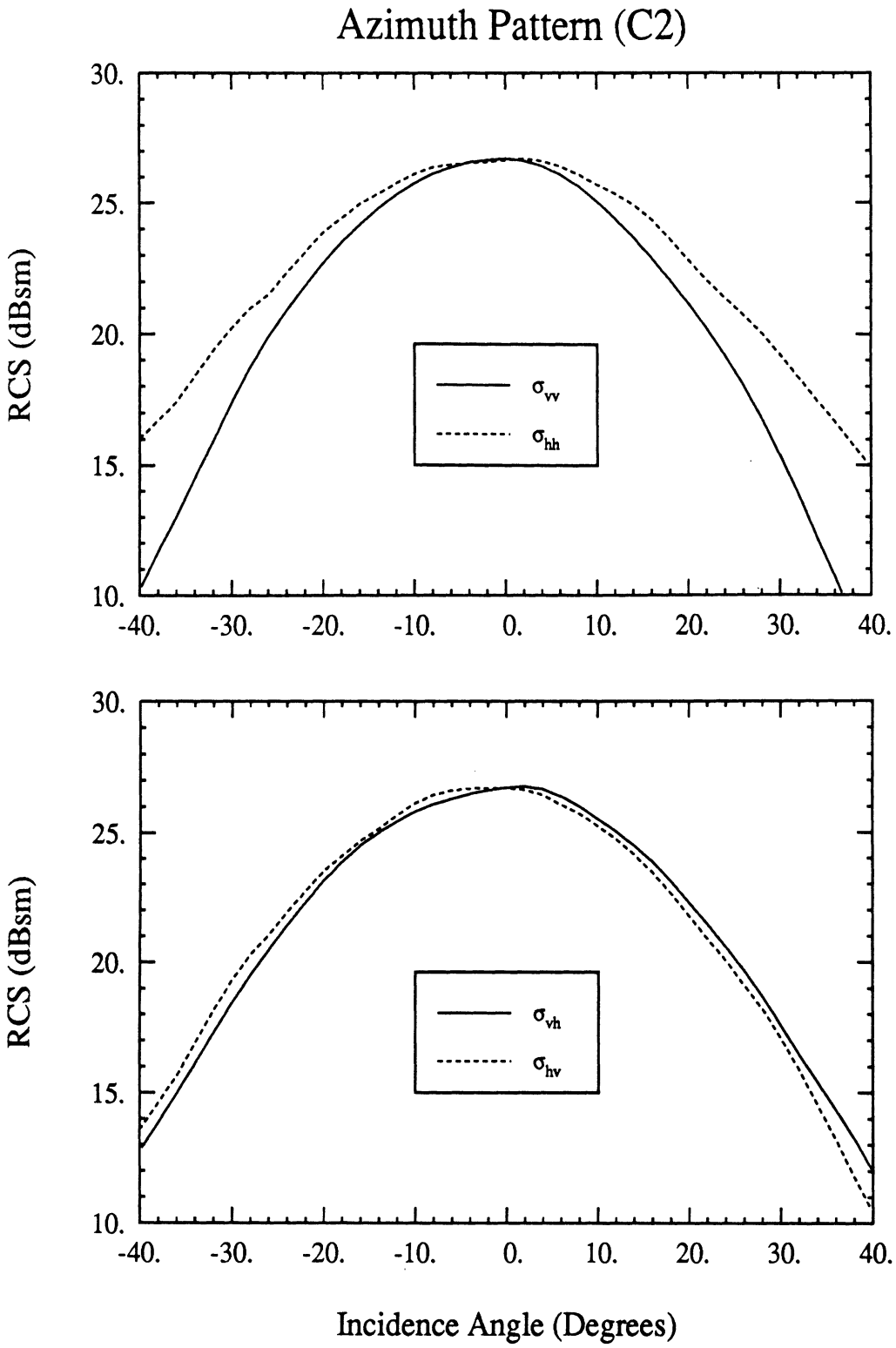

Figure 38: Azimuth pattern of amplitude of scattering matrix elements for C2 PARC.

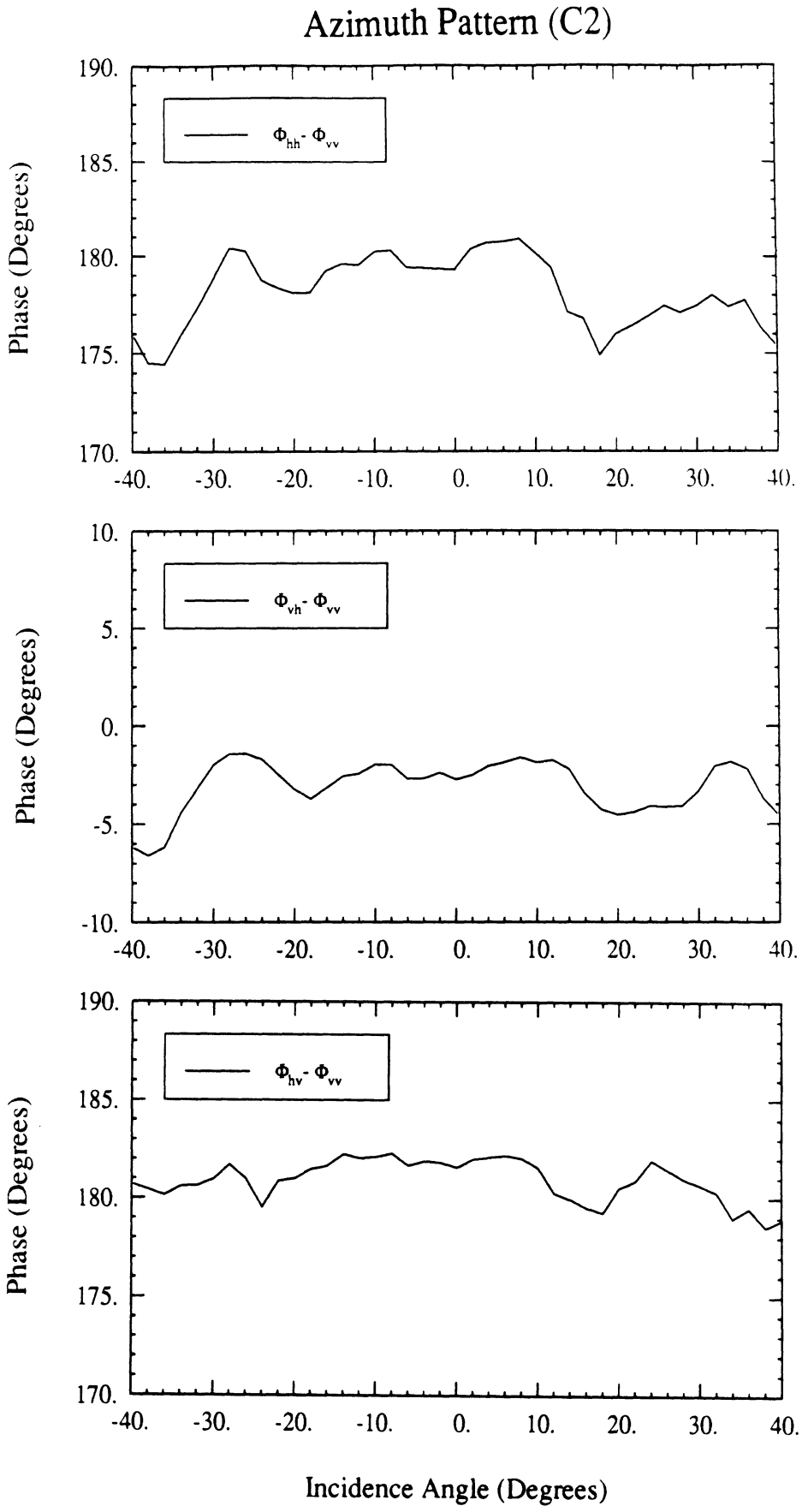

Figure 39: Azimuth pattern of phase of scattering matrix elements for C2 PARC.

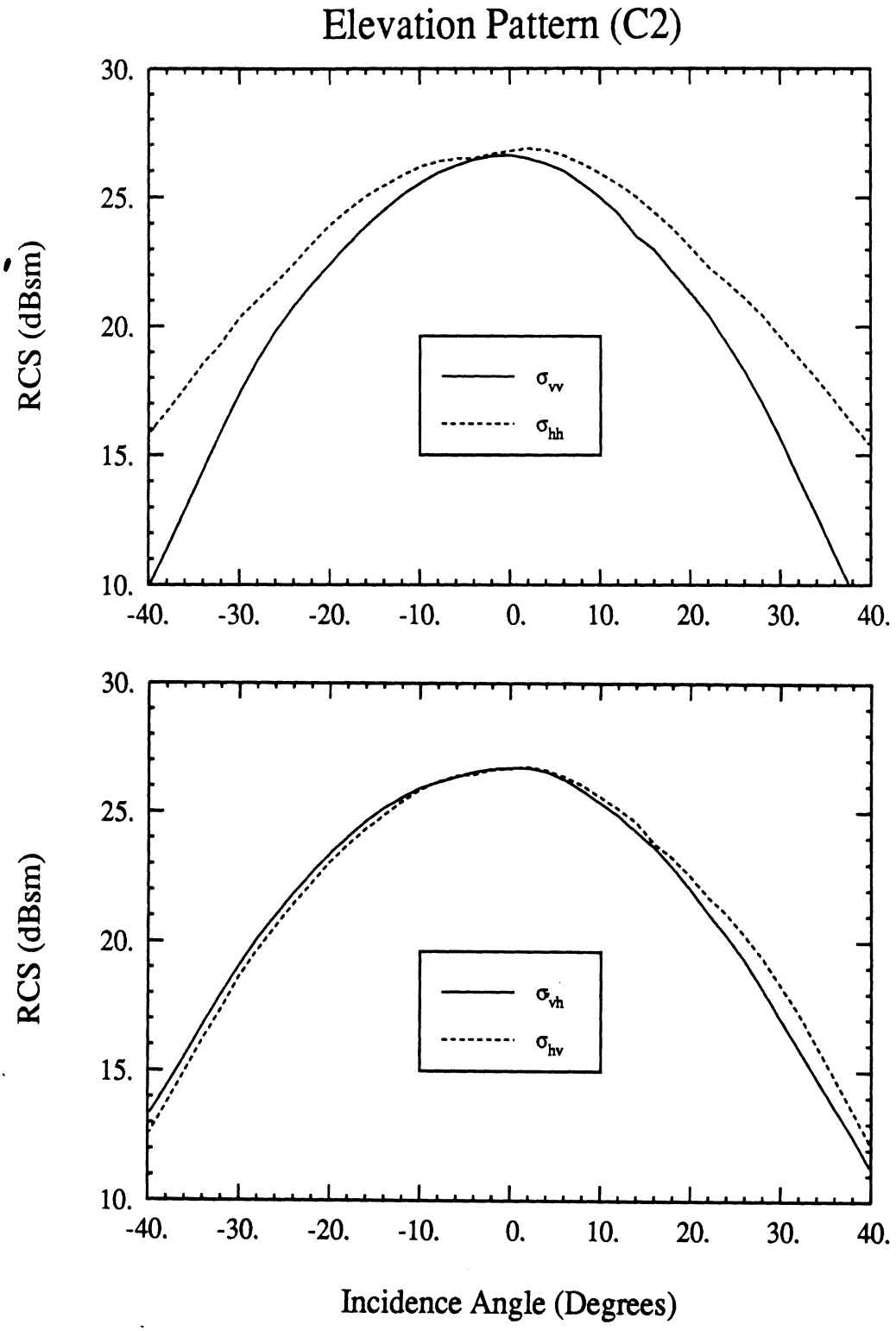

Figure 40: Elevation pattern of amplitude of scattering matrix elements for C2 PARC.

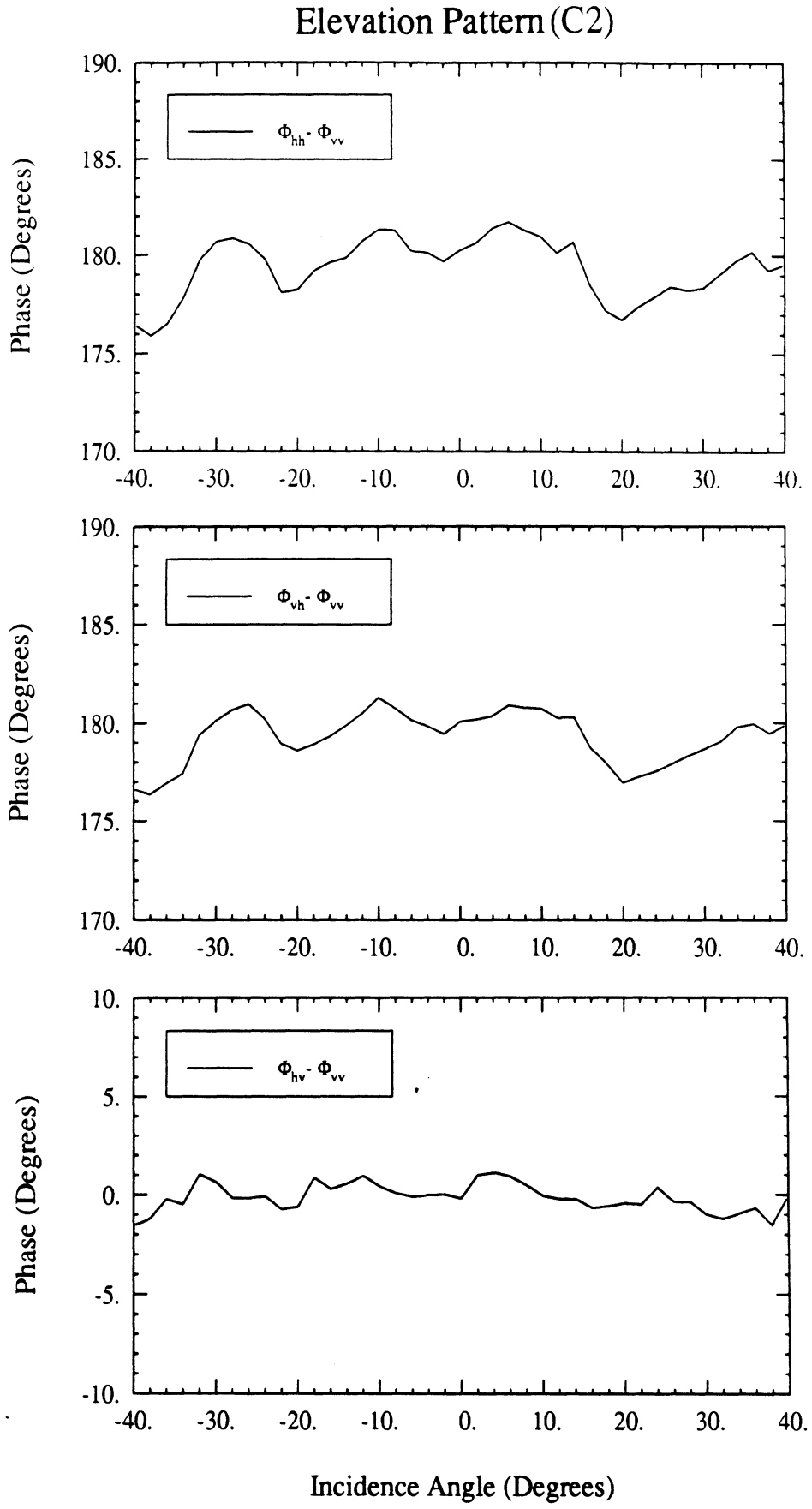

Figure 41: Elevation pattern of phase of scattering matrix elements for C2 PARC.

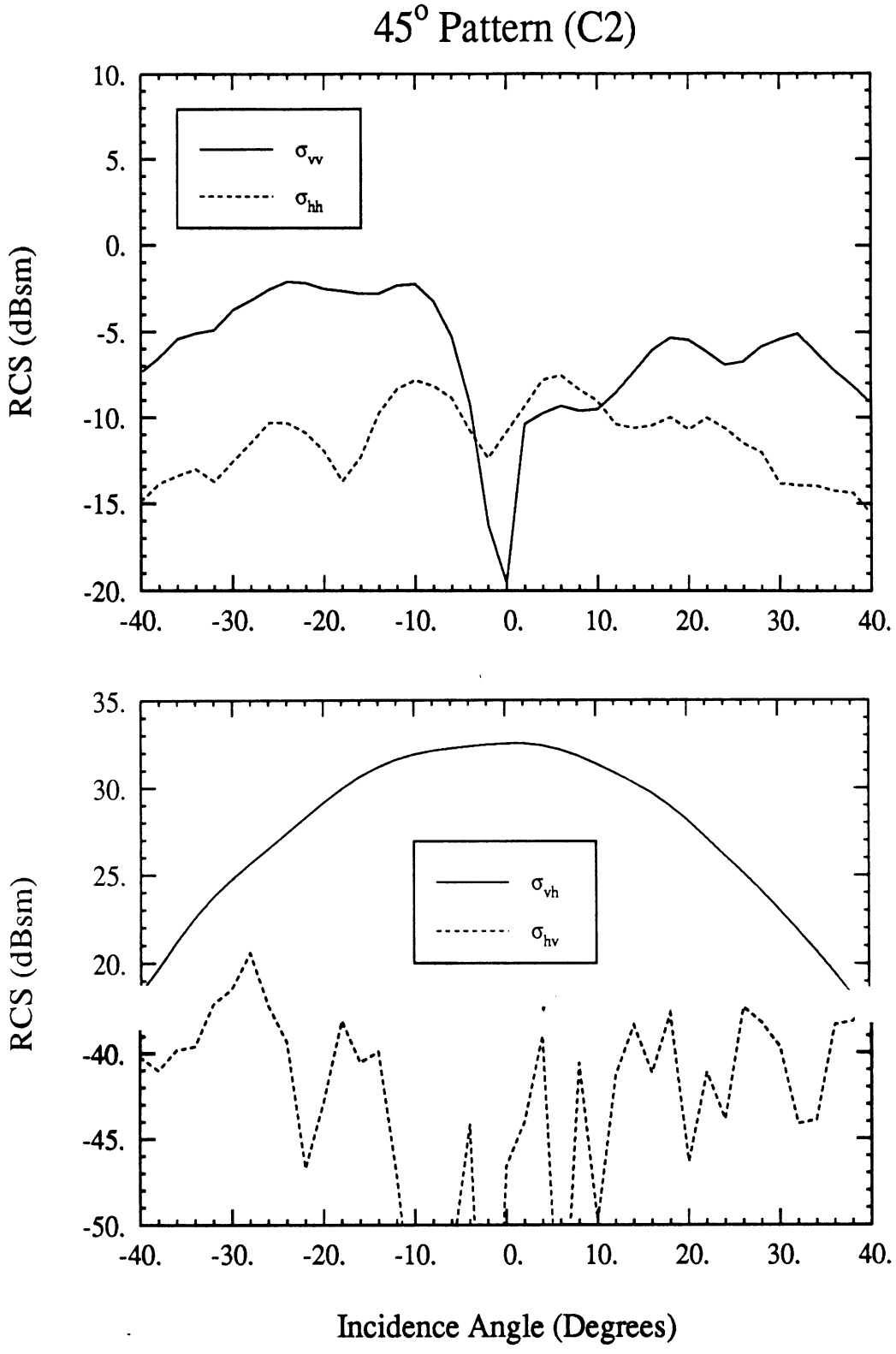

Figure 42: 45° pattern of amplitude of scattering matrix elements for C2 PARC.

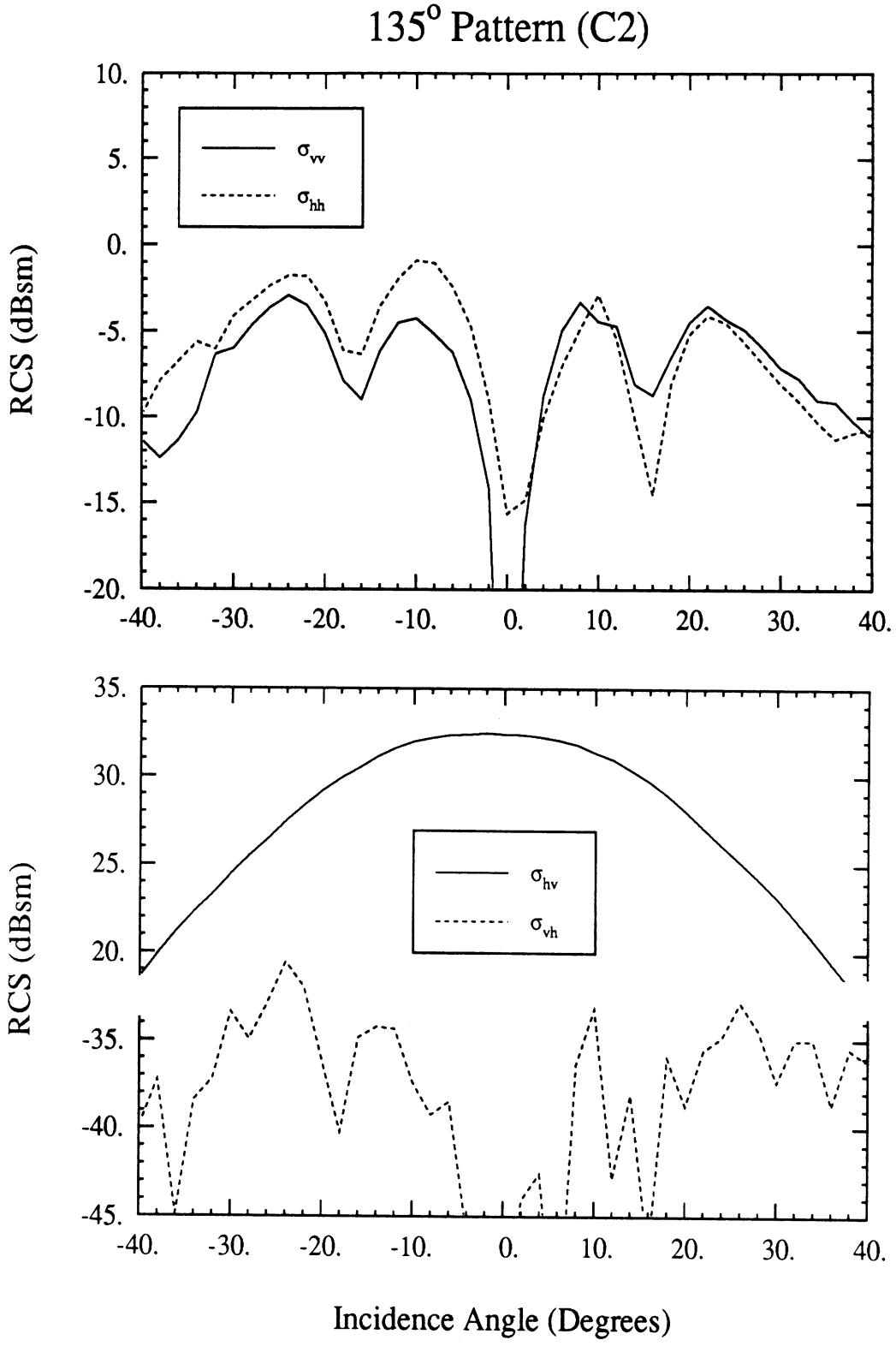

Figure 43: 135° pattern of amplitude of scattering matrix elements for C2 PARC.

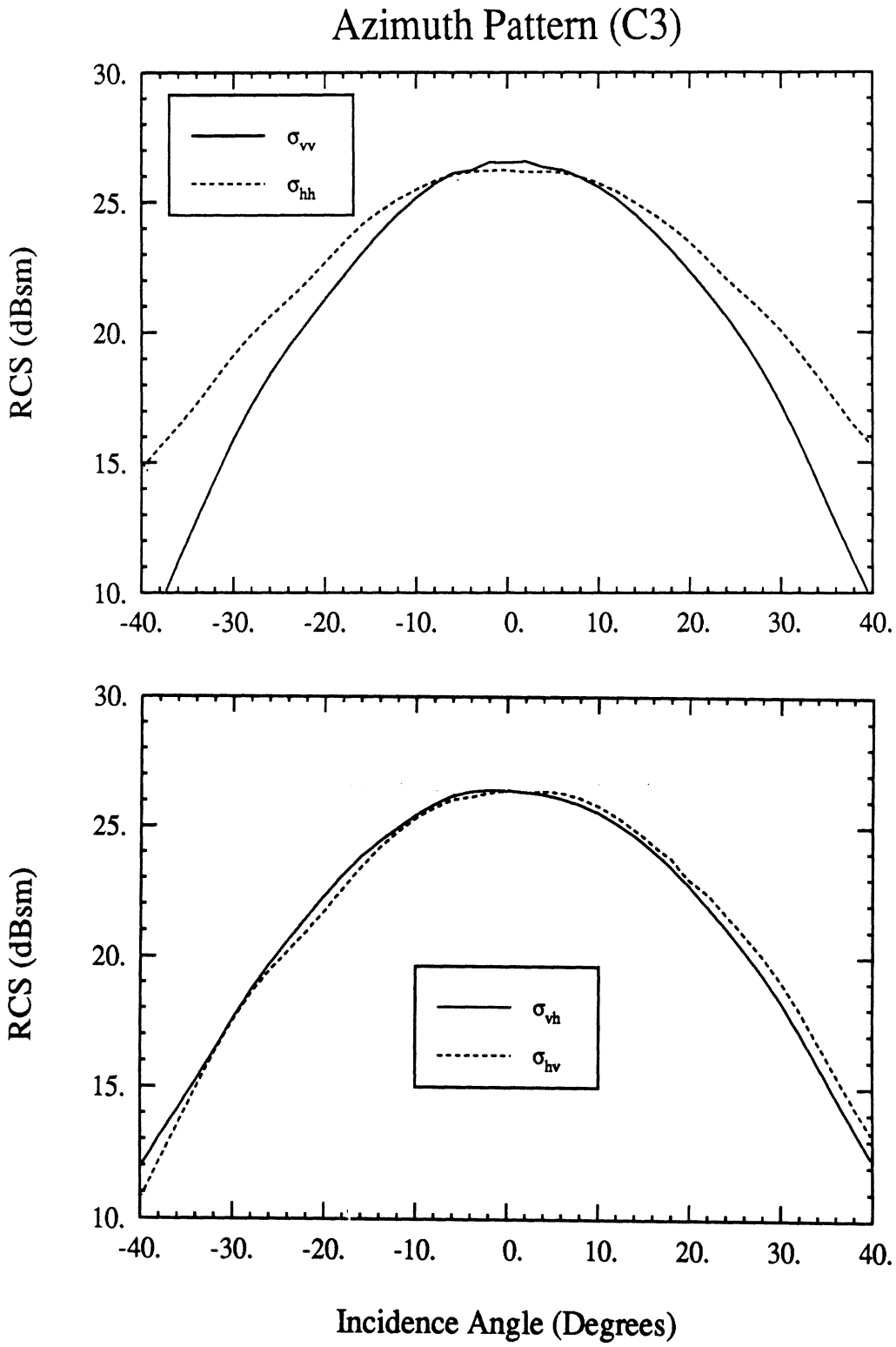

Figure 44: Azimuth pattern of amplitude of scattering matrix elements for C3 PARC.

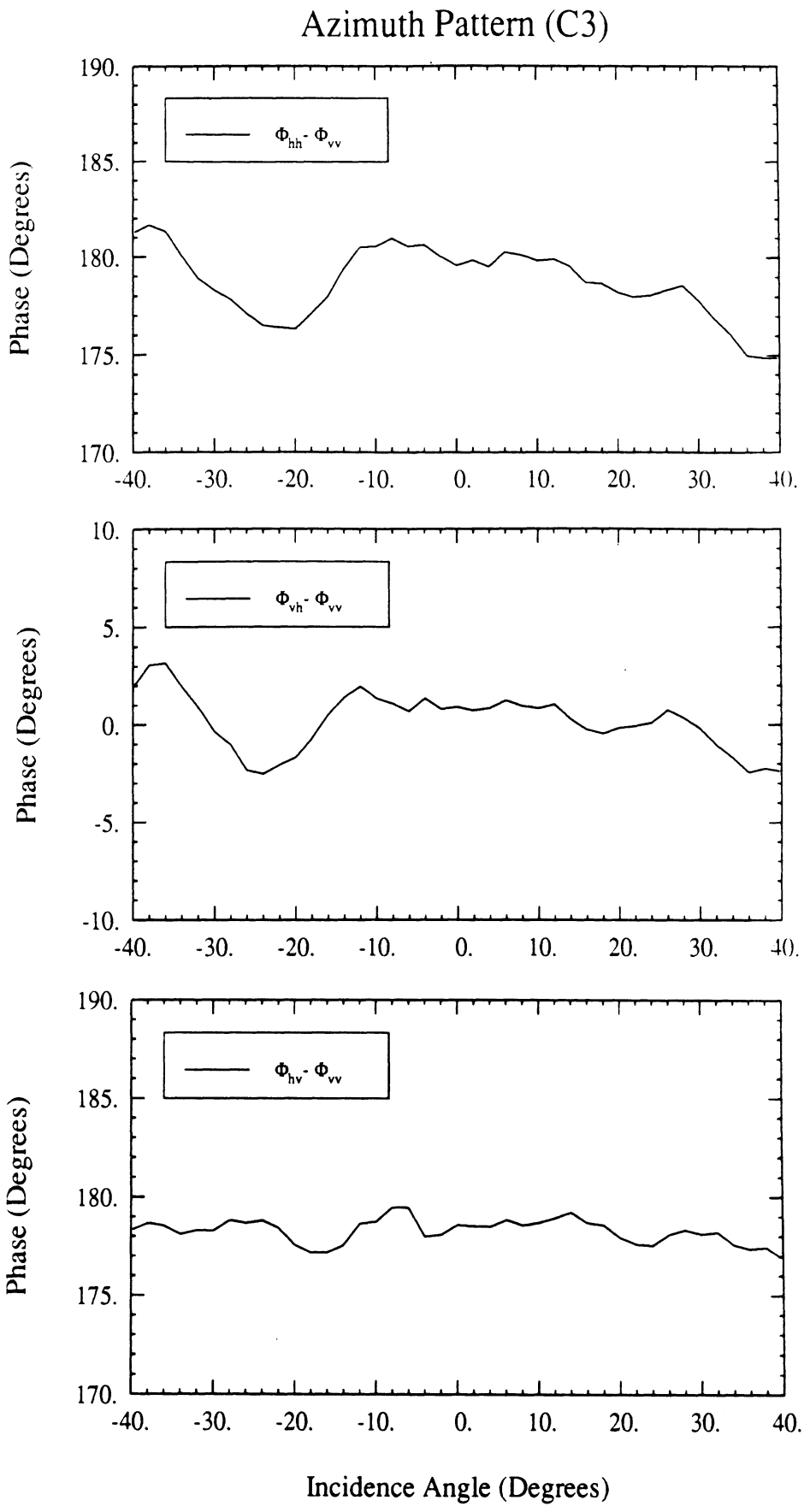

Figure 45: Azimuth pattern of phase of scattering matrix elements for C3 PARC.

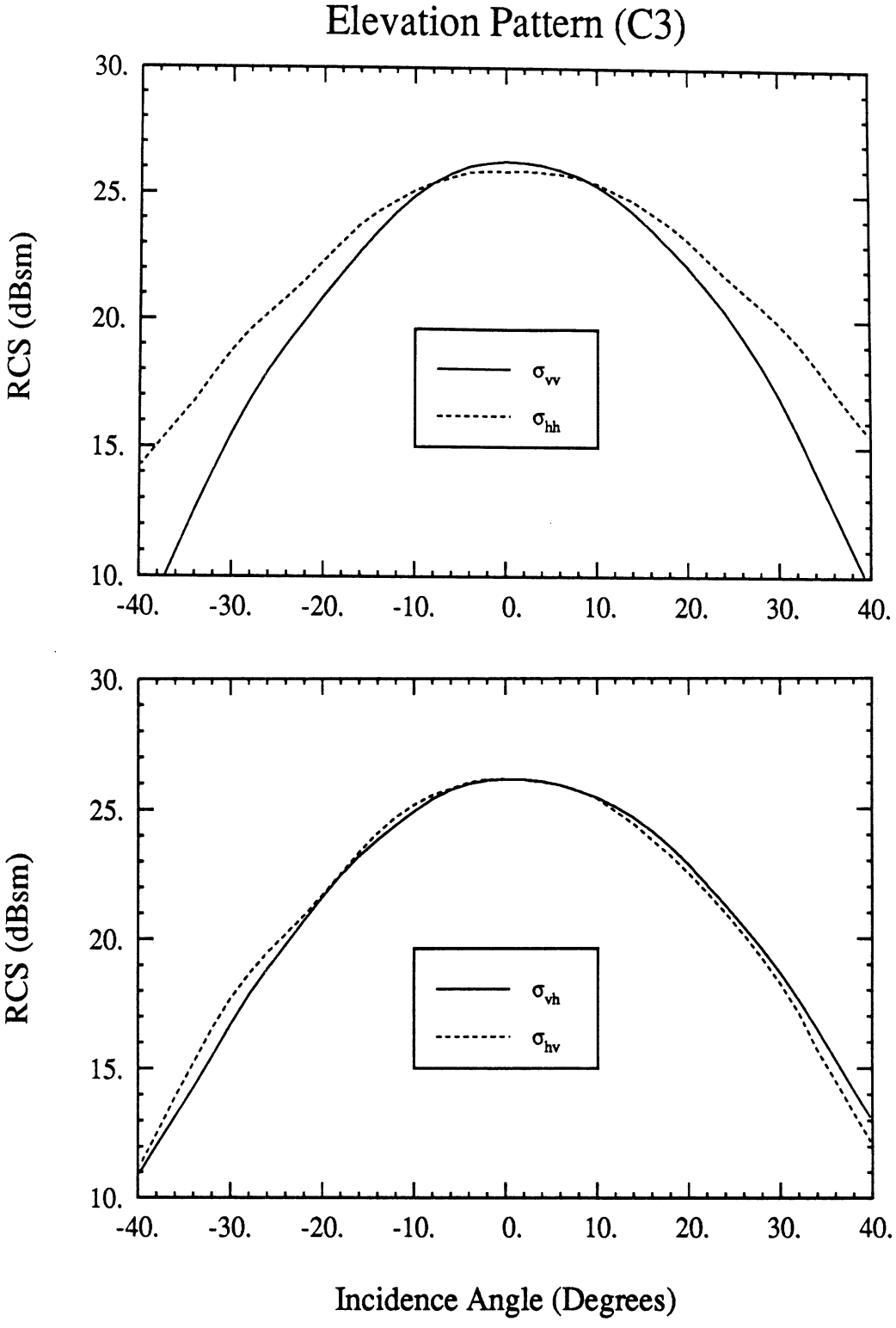

Figure 46: Elevation pattern of amplitude of scattering matrix elements for C3 PARC.

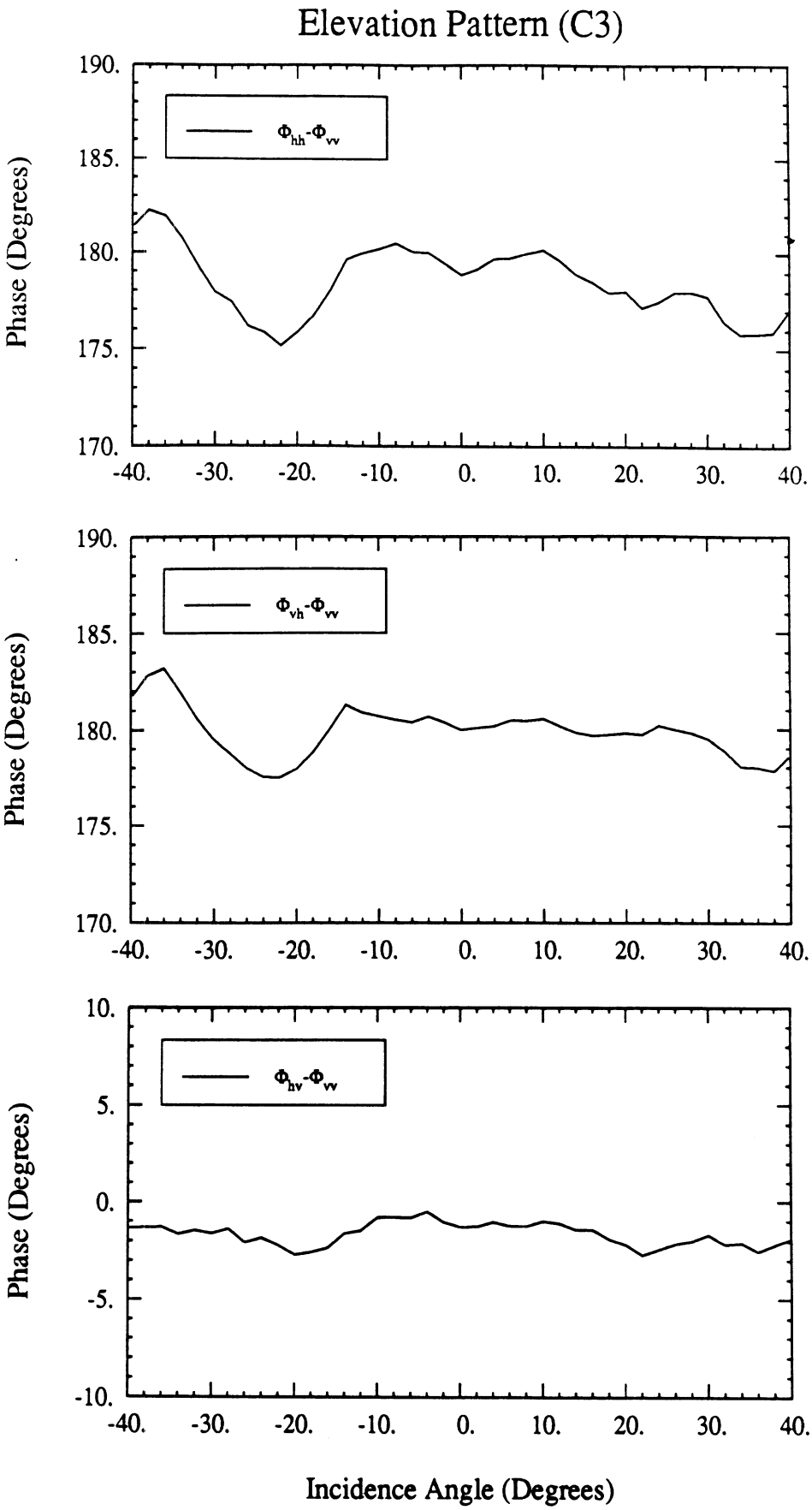

Figure 47: Elevation pattern of phase of scattering matrix elements for C3 PARC.

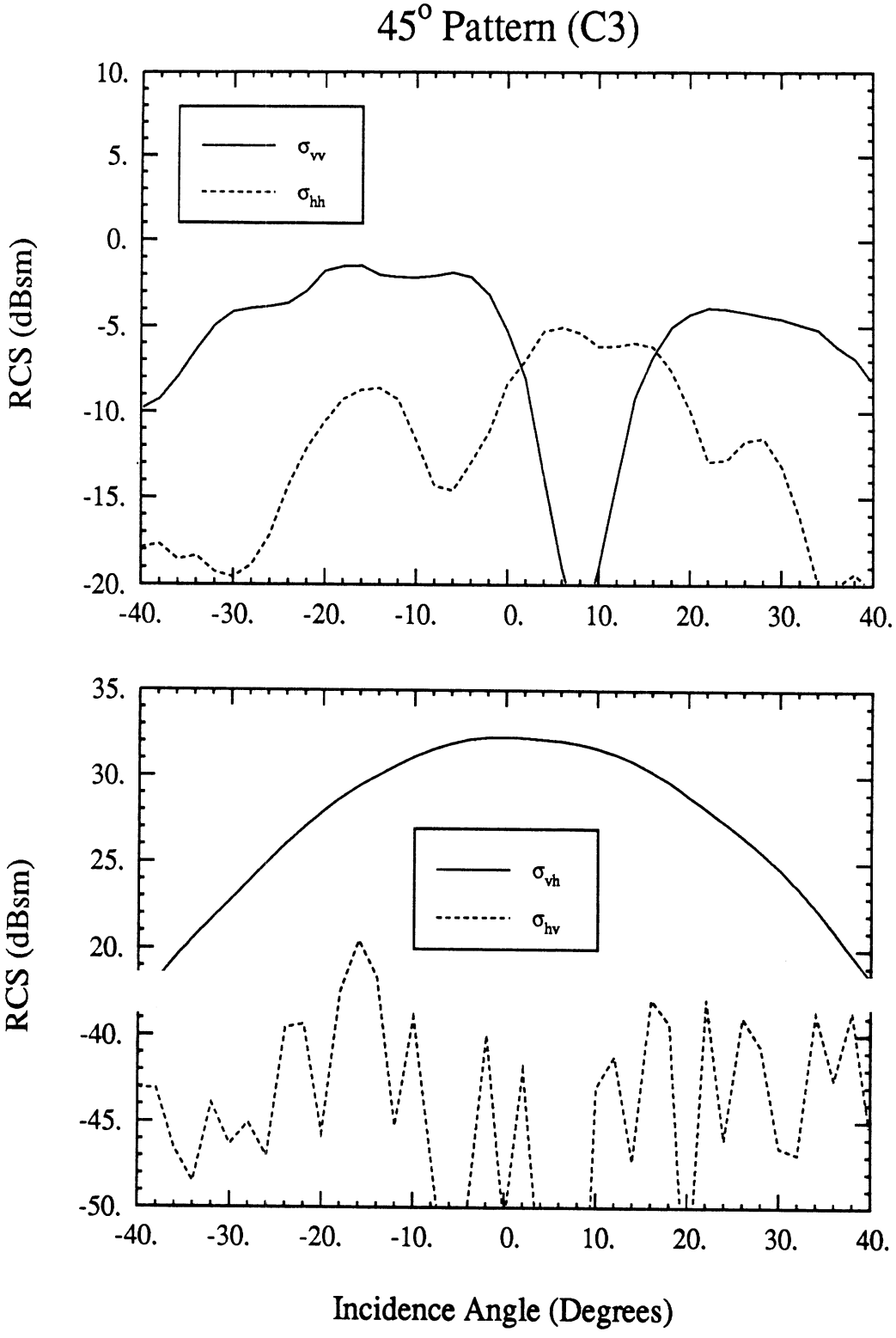

Figure 48: 45° pattern of amplitude of scattering matrix elements for C3 PARC.

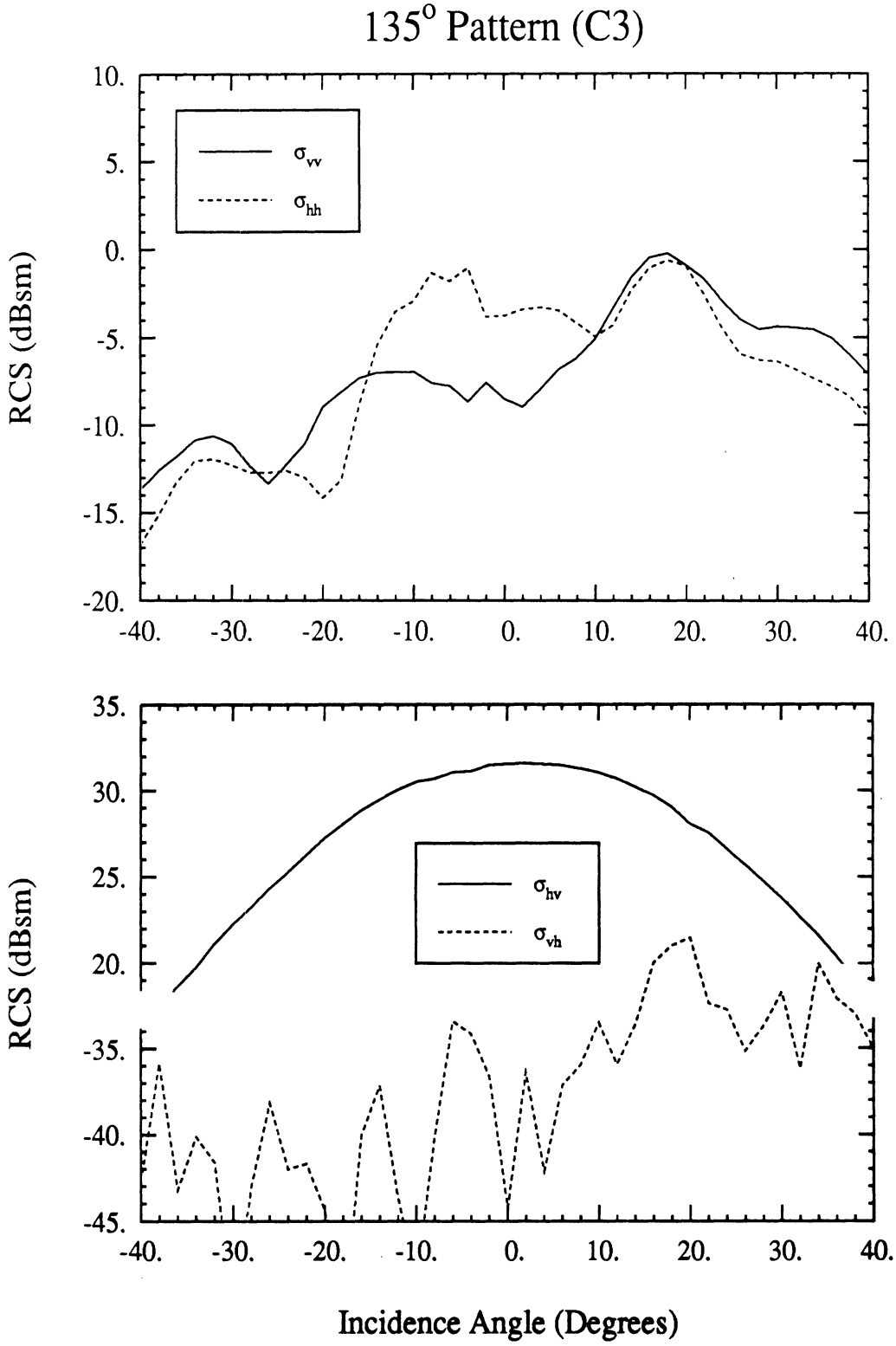

Figure 49: 135° pattern of amplitude of scattering matrix elements for C3 PARC.

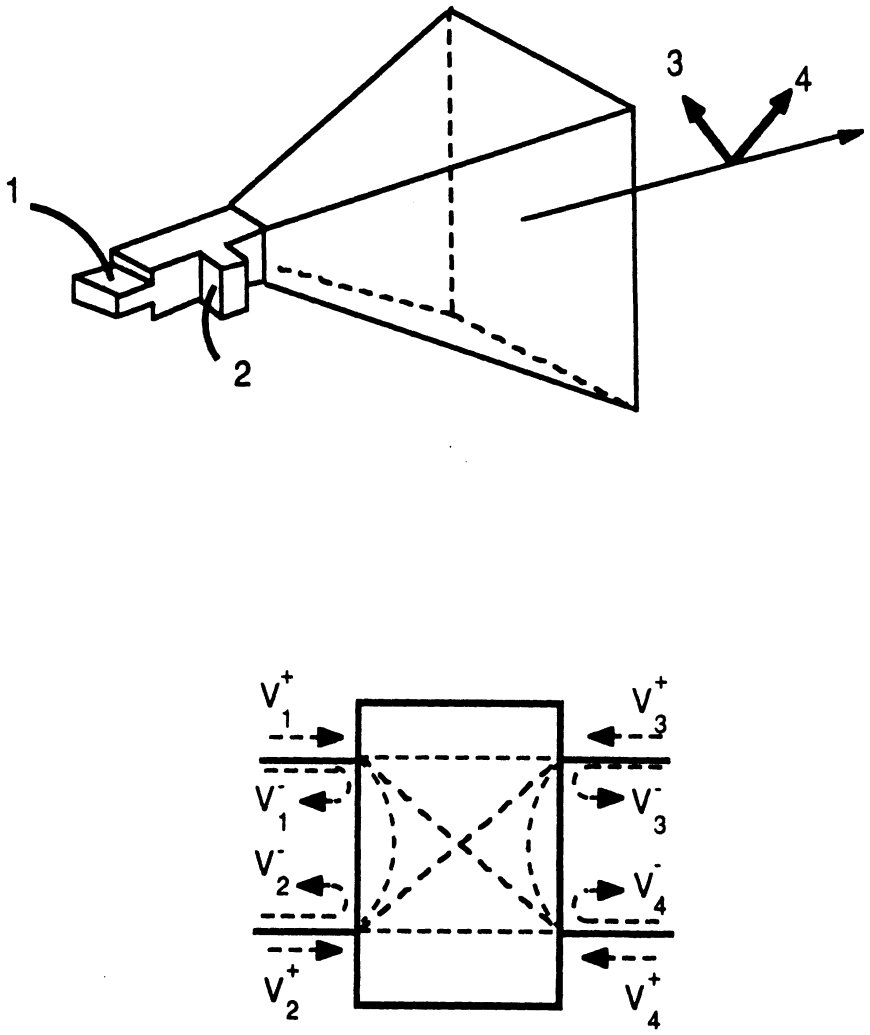

Figure A-1: Antenna system and its equivalent circuit four-port representation.

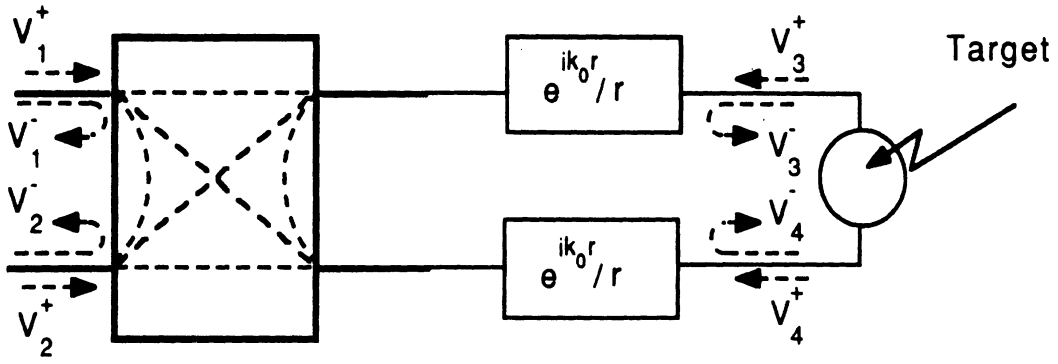

Figure A-2: Signal flow-chart of the antenna system, free space, and the target.

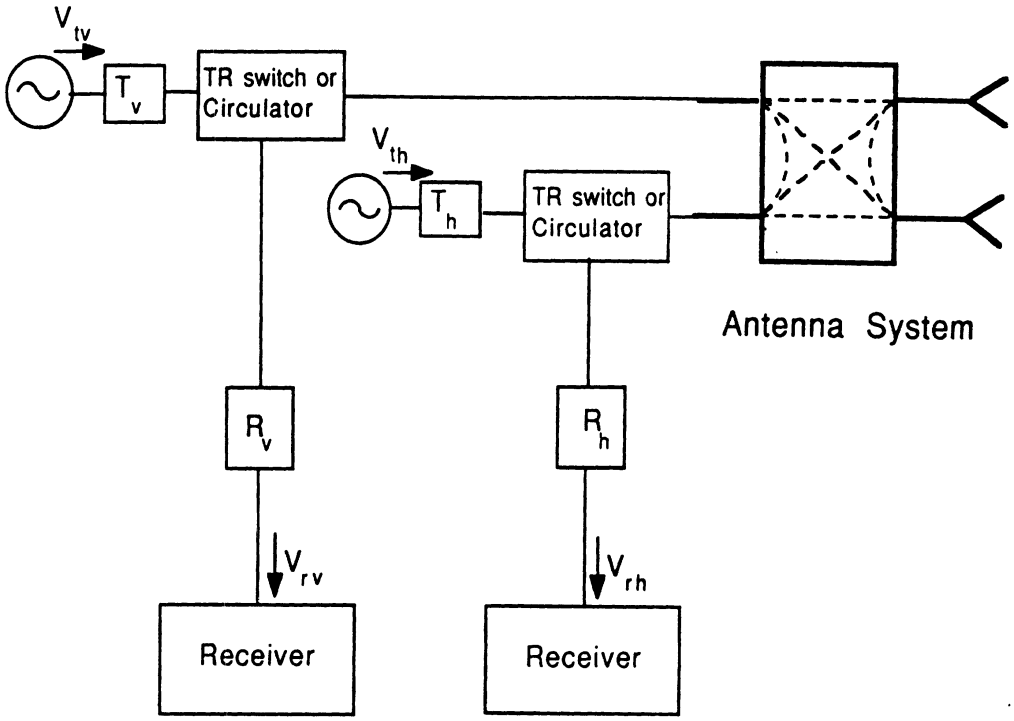

Figure A-3: Simplified block diagram of a typical polarimetric radar.

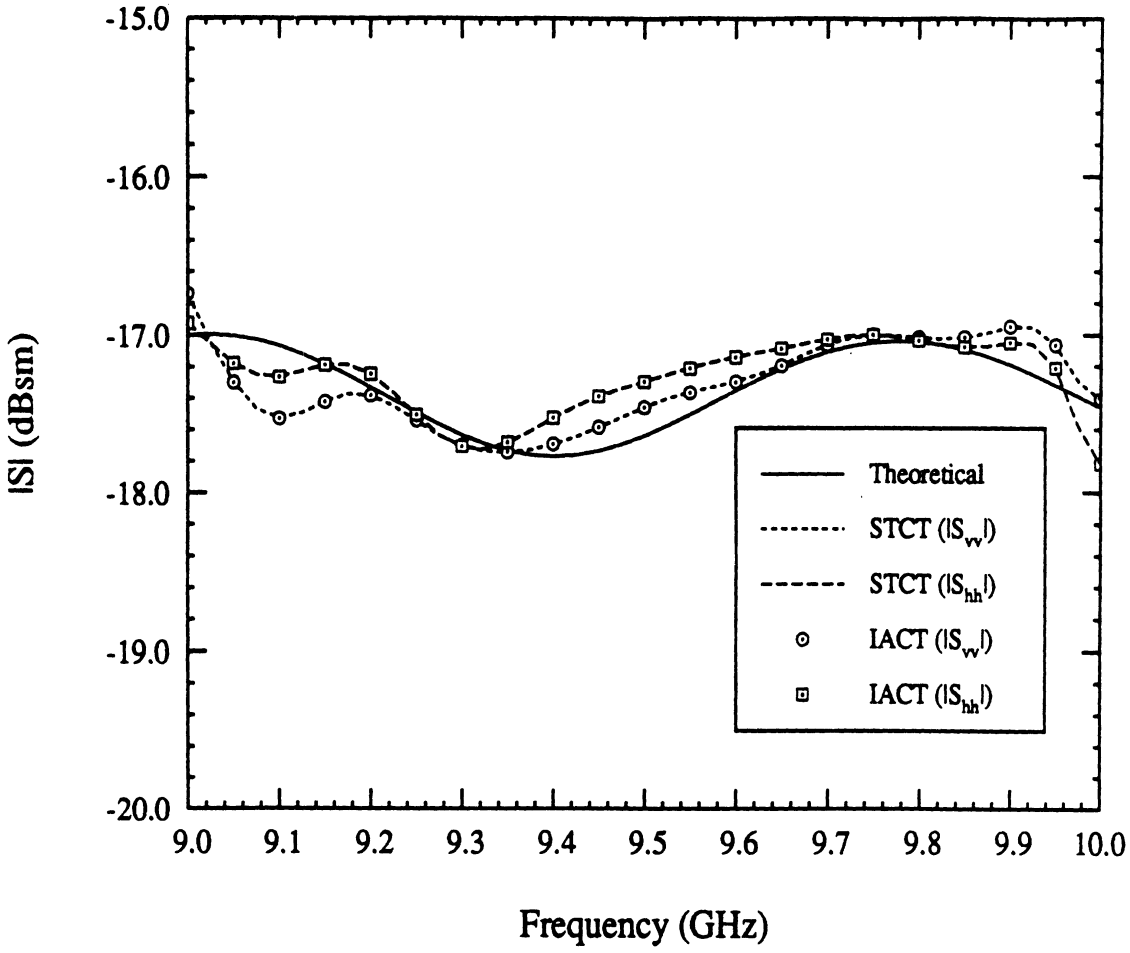

Figure A-4: Magnitude of the diagonal elements of the scattering matrix of a 6-inch sphere.

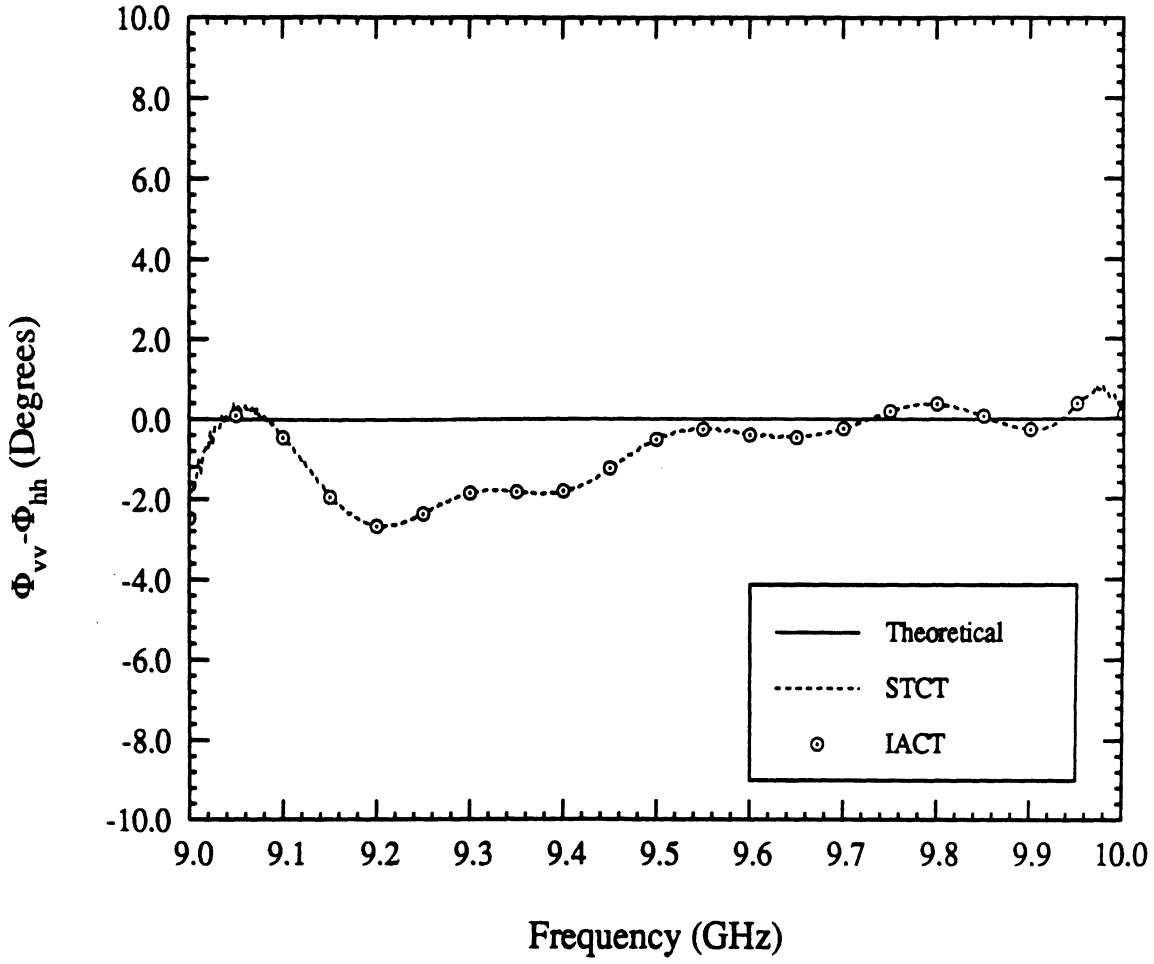

Figure A-5: Phase difference between the diagonal elements of the scattering matrix of a 6-inch sphere.

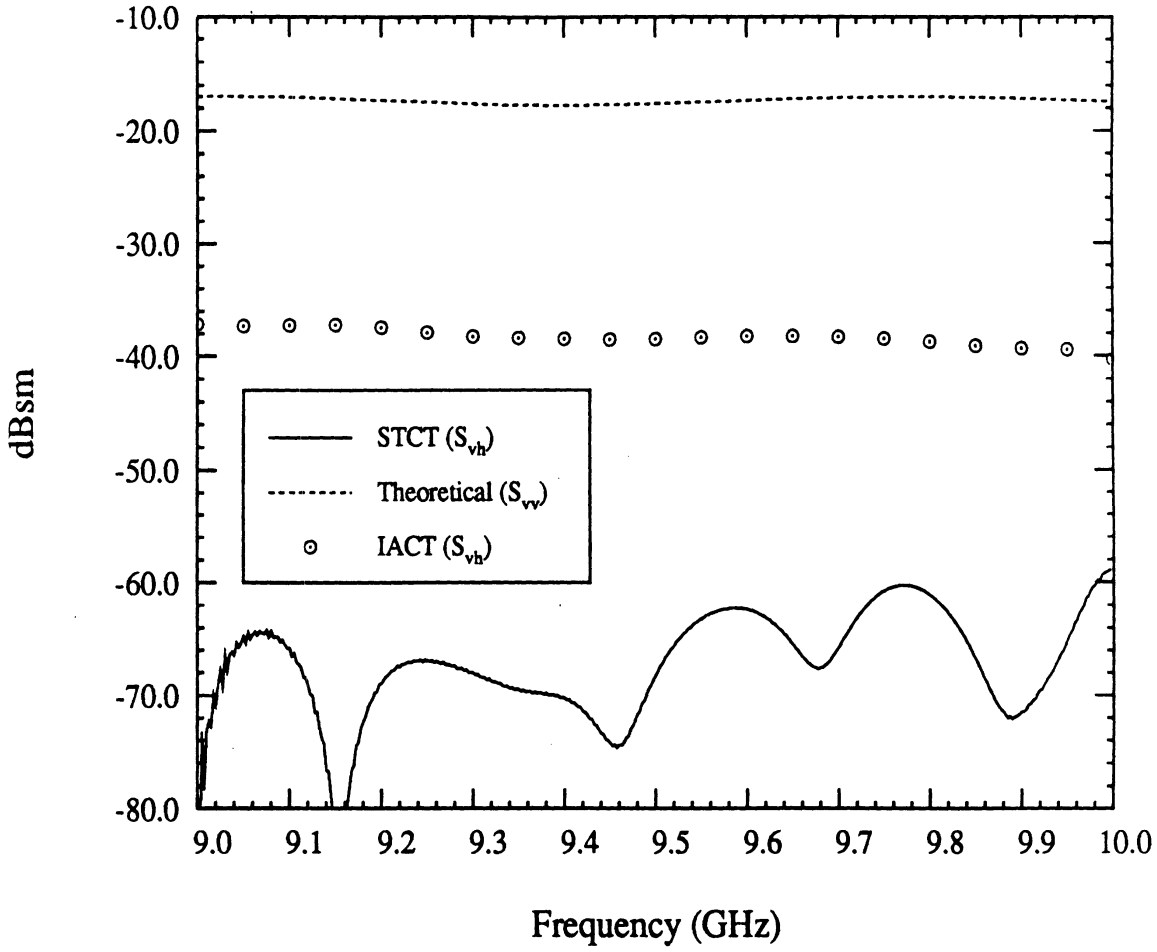

Figure A-6: Magnitude of the off-diagonal element of the scattering matrix of a 6-inch sphere compared with one of the diagonal elements.

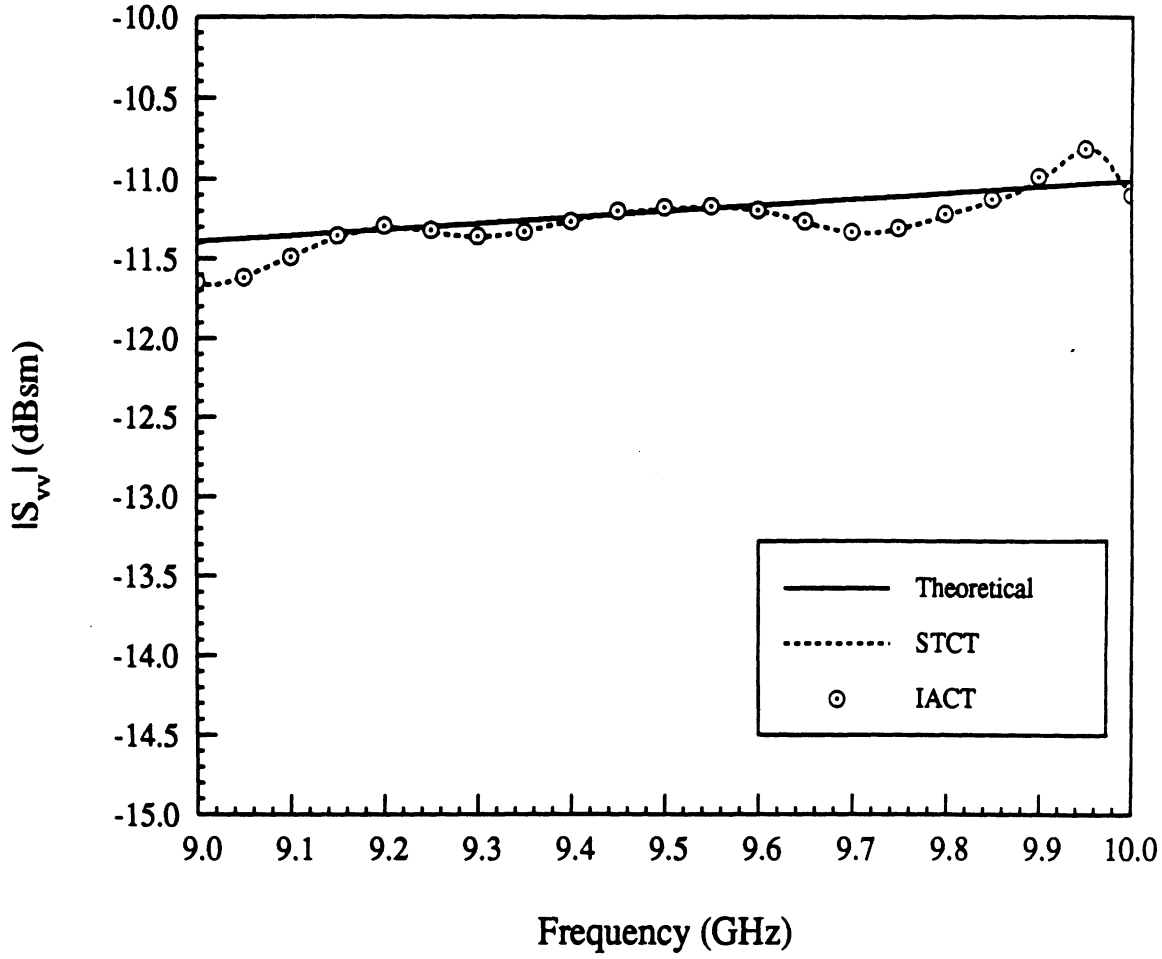

Figure A-7: Magnitude of the diagonal element (s_{vv}) of the scattering matrix of the vertical cylinder.

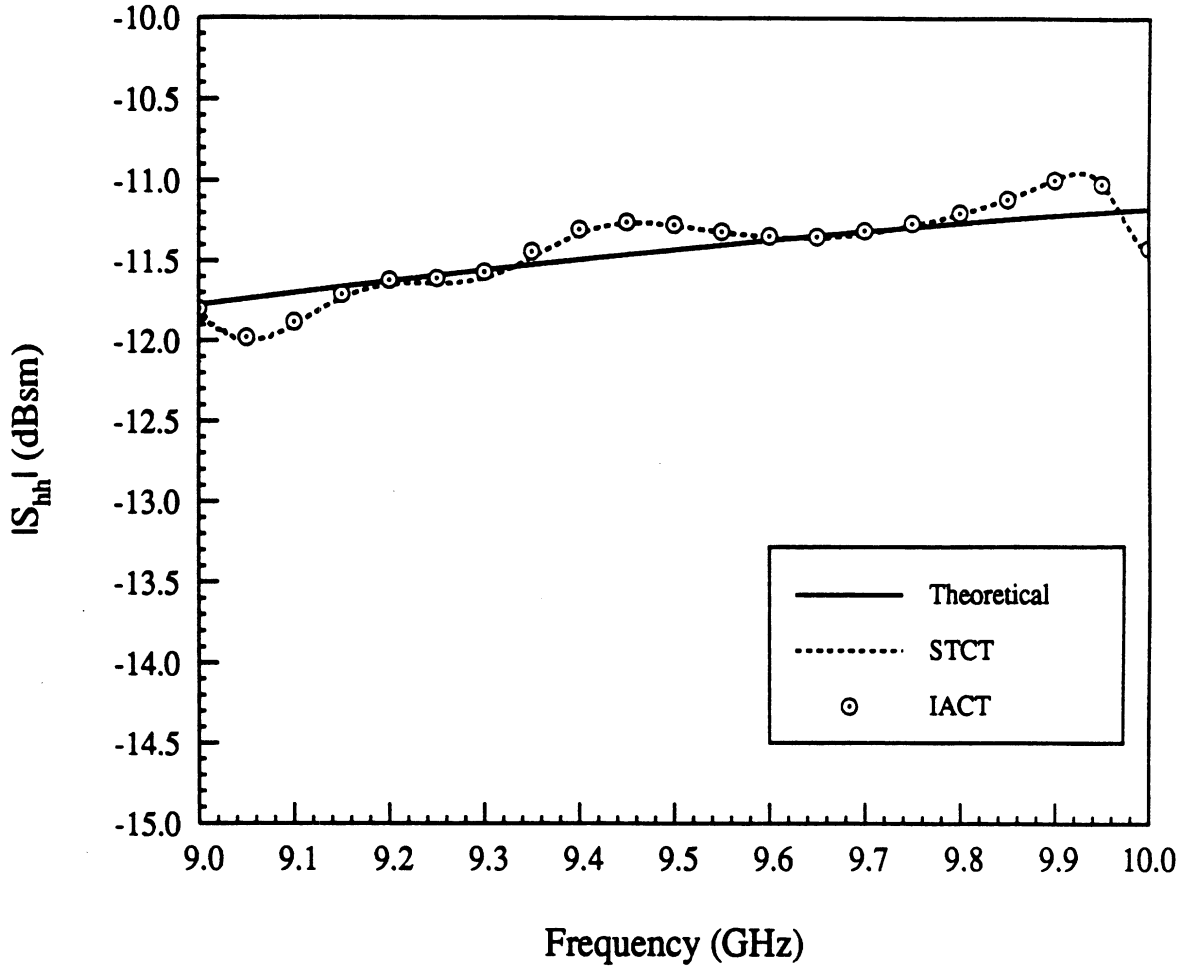

Figure A-8: Magnitude of the diagonal element (s_{hh}) of the scattering matrix of the vertical cylinder.

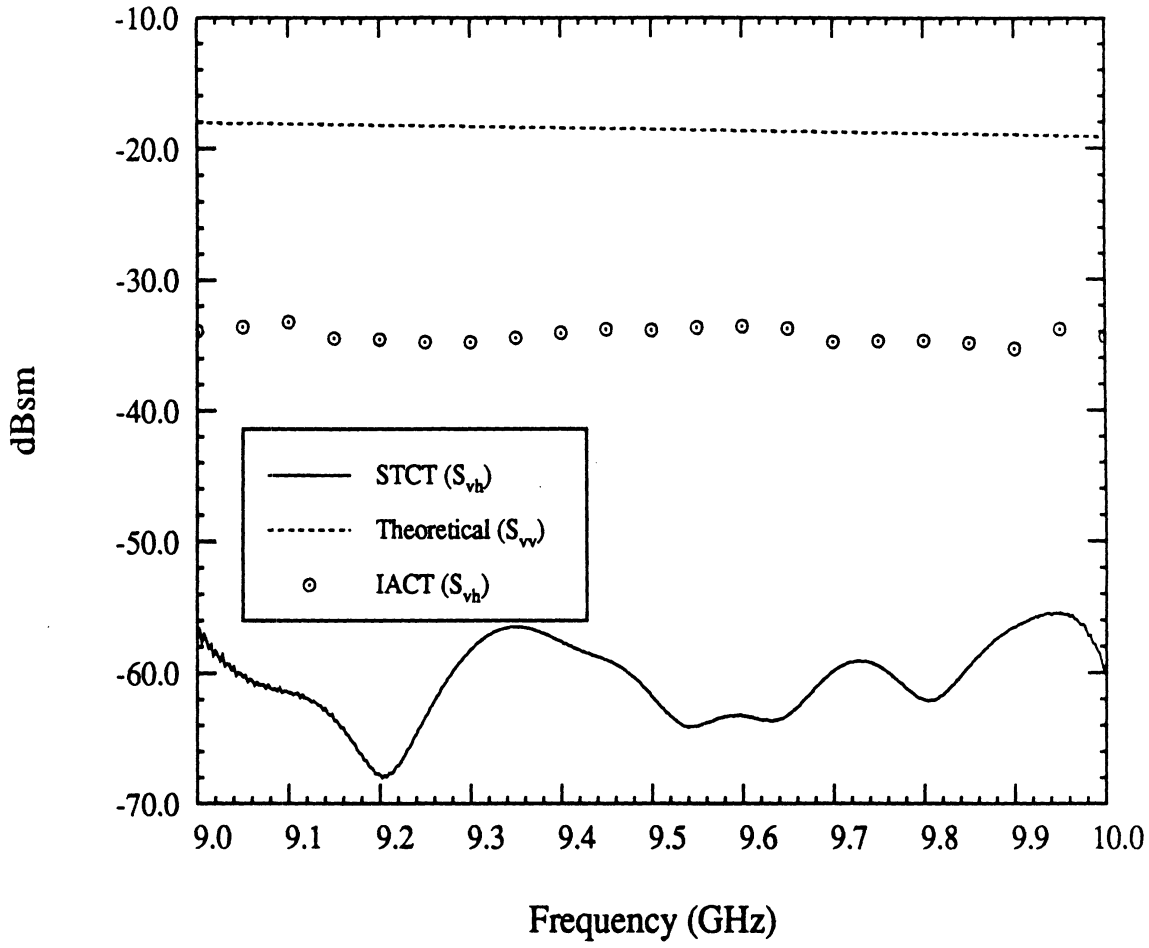

Figure A-9: Magnitude of the off-diagonal element (s_{vh}) of the scattering matrix of the vertical cylinder compared with s_{vv}.

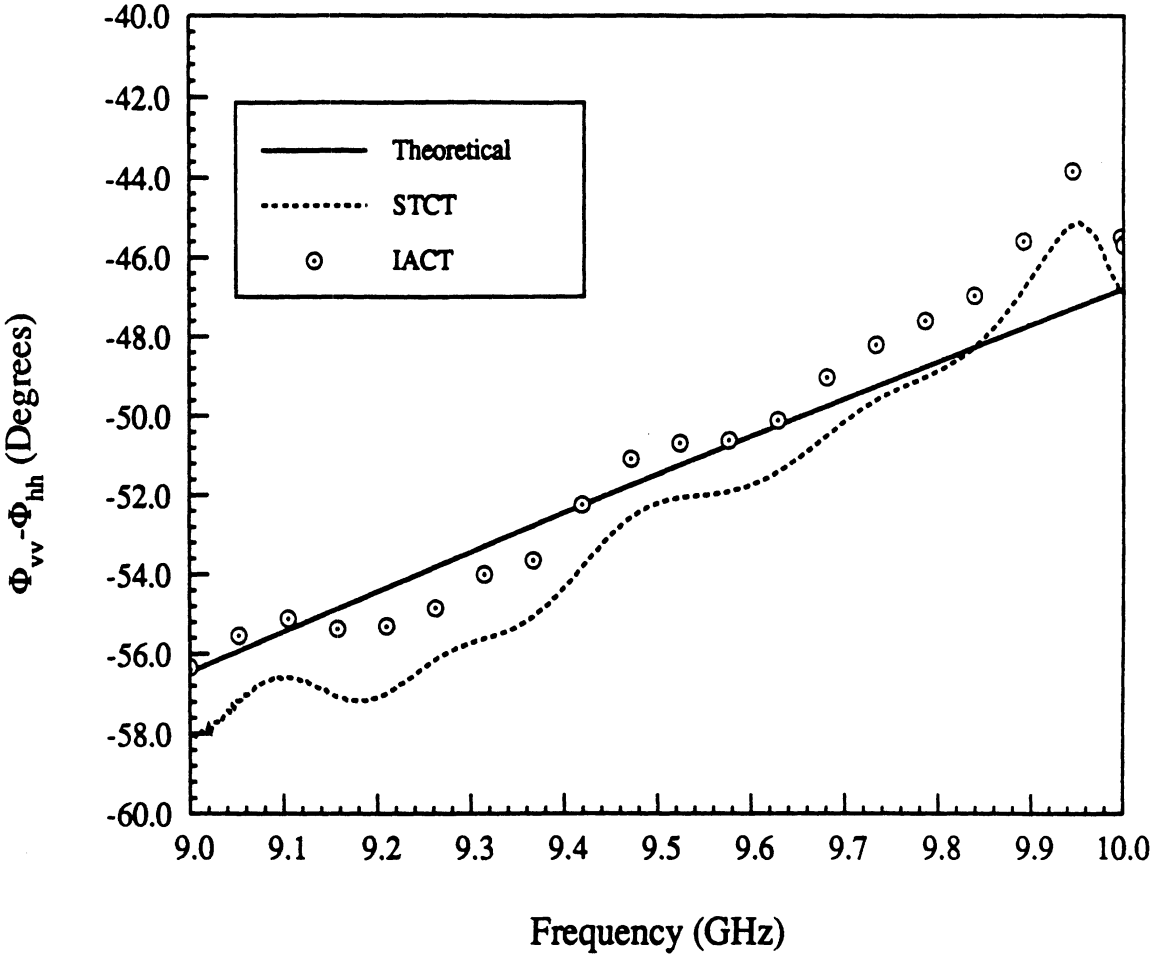

Figure A-10: Phase difference between the diagonal elements of the scattering matrix of the vertical cylinder.

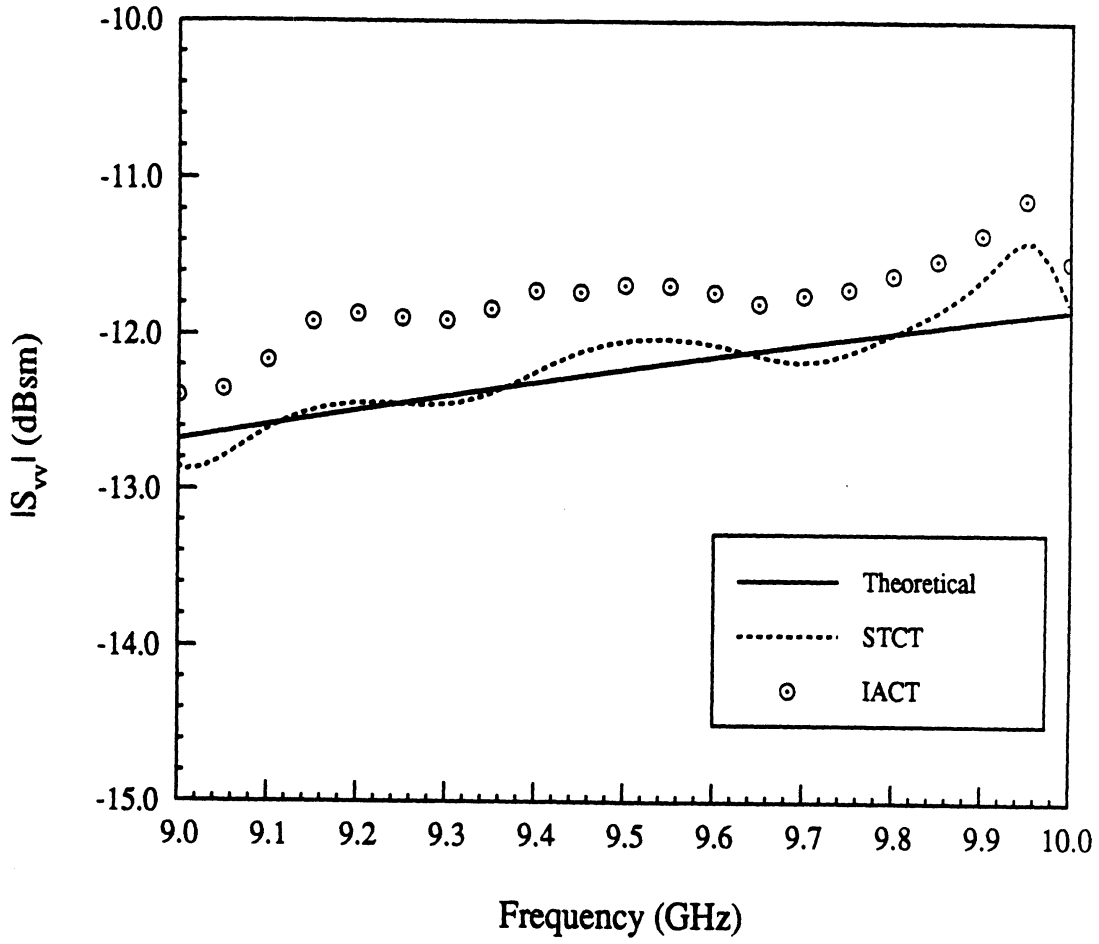

Figure A-11: Magnitude of the diagonal element (s_{vv}) of the scattering matrix of the 45° tilted cylinder.

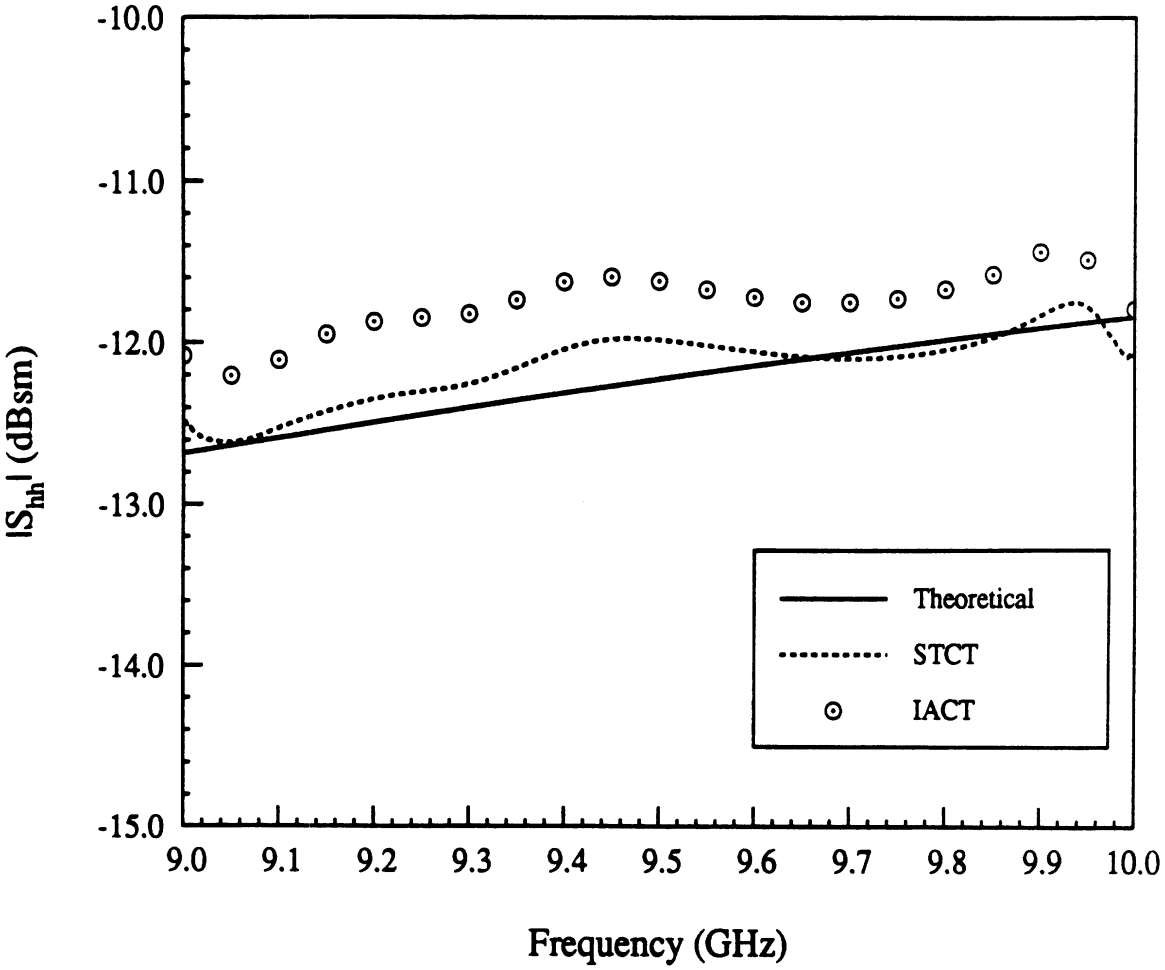

Figure A-12: Magnitude of the diagonal element (s_{hh}) of the scattering matrix of the 45° tilted cylinder.

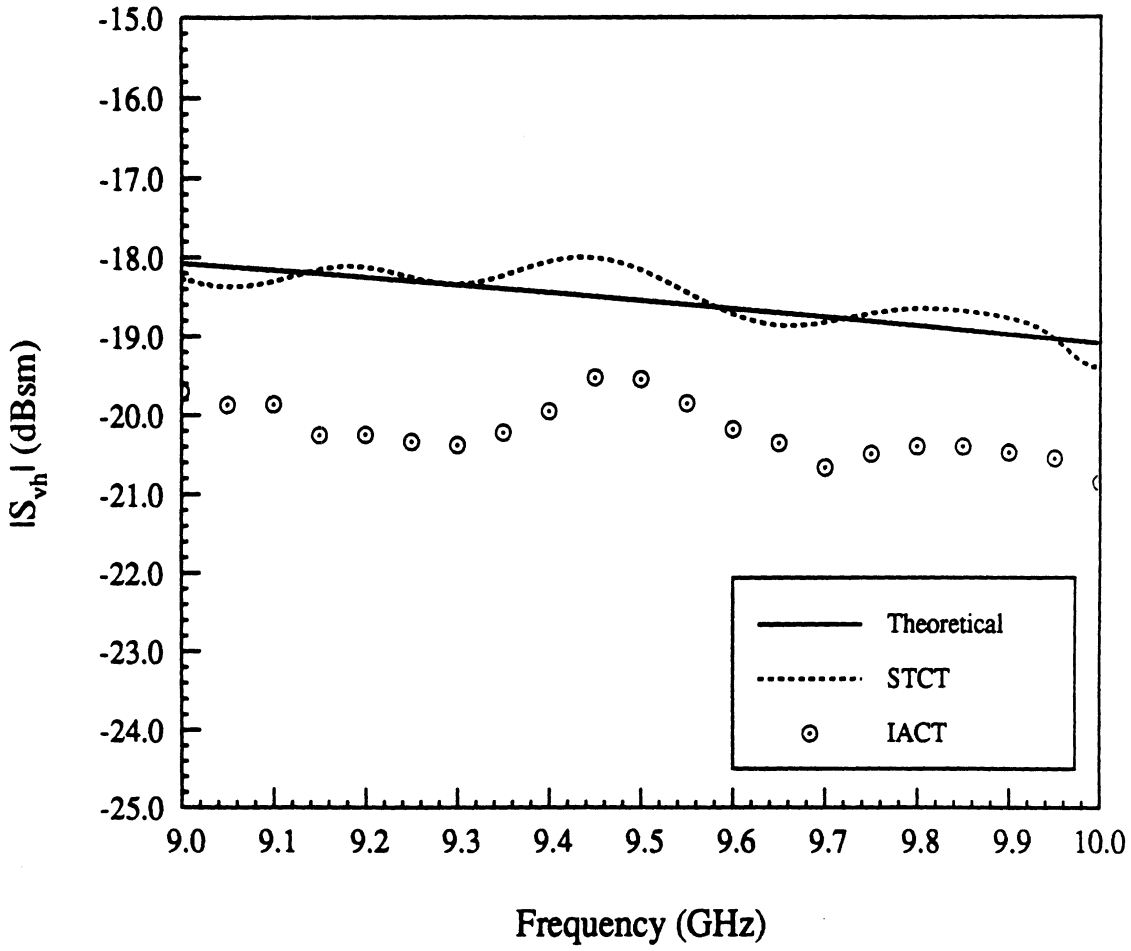

Figure A-13: Magnitude of the off-diagonal element (s_{vh}) of the scattering matrix of the 45° tilted cylinder.

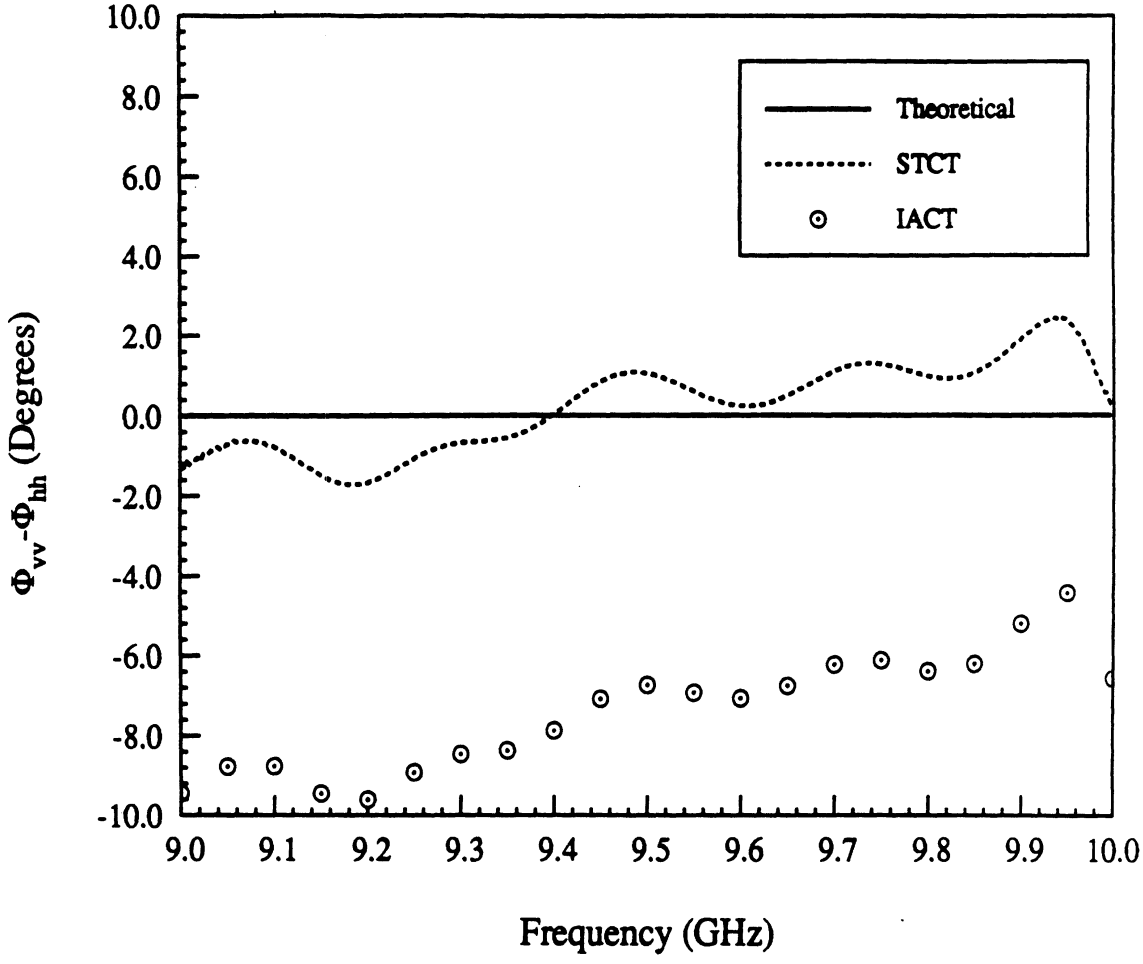

Figure A-14: Phase difference between the diagonal elements of the scattering matrix of the 45° tilted cylinder.

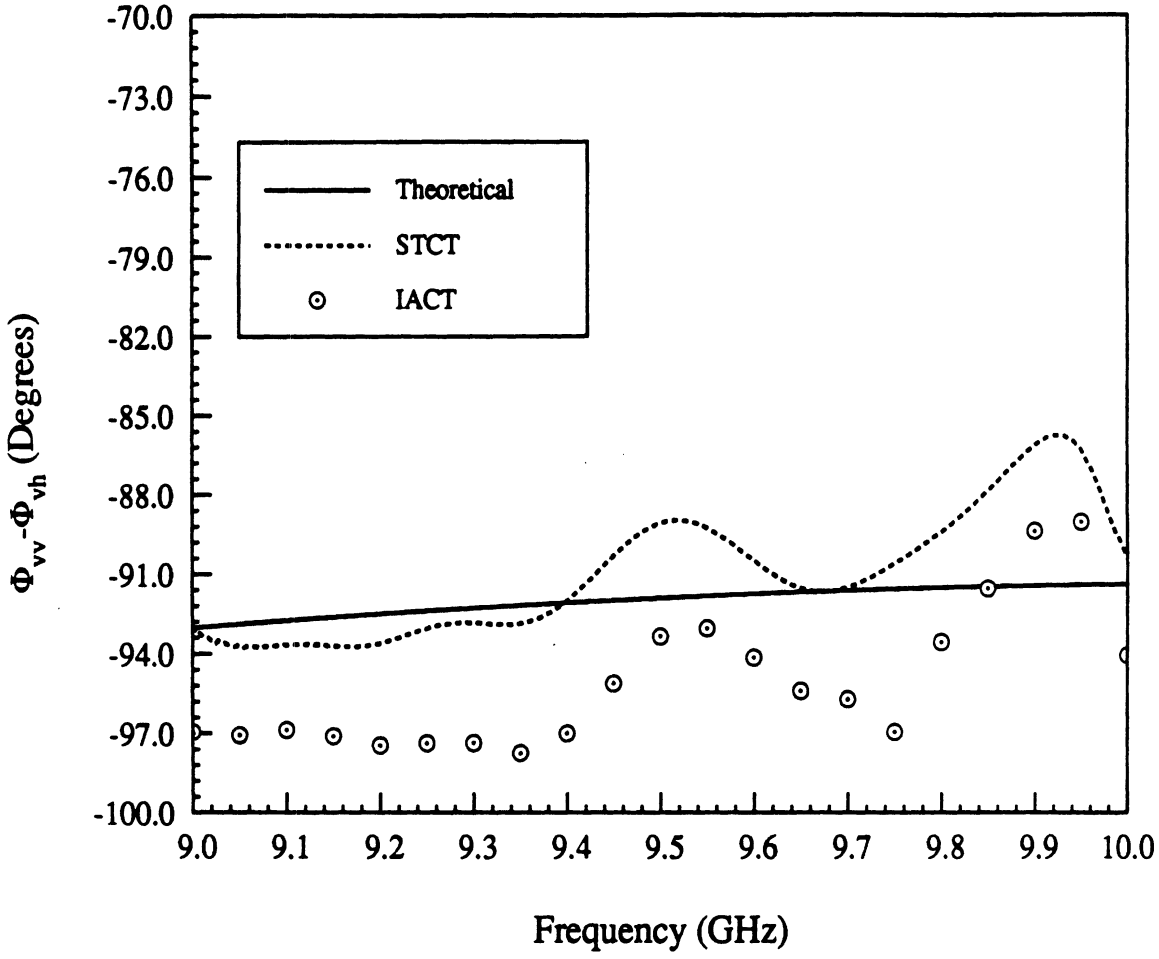

Figure A-15: Phase difference between the diagonal and the off-diagonal elements of the scattering matrix of the 45° tilted cylinder.